



Politecnico di Torino

FACOLTÀ DI INGEGNERIA
Corso di Laurea Magistrale in Ingegneria Meccanica

TESI DI LAUREA MAGISTRALE

**Geometrical Irregularities Effect
on Lead Sheathing
for Submarine Power Cable Applications**

Candidato:
Edgardo Moreno
Matricola s256830

Relatori:
Aurelio Somà
Filippo Berto
Correlatore:
Lorenzo Peroni

Anno Accademico 2019-2020

*Al mio nonno Angelo,
il mio piú grande sostenitore.*

Abstract

In countries which have to deal with the electrical energy supply to several and small islands, wind farms, oil wells and other users by the sea, a local power production is often not possible, not convenient or with a low efficiency. For these reasons in the last century, and above all in the last decades with a growing interest from the research field, the employment of submarine power cables to provide electrical power to the less accessible users is increasing. After the installation, the main problem for these systems is their life expectation, thus the study of their creep-fatigue behaviour. The life of these cables, which is determined by the most critical layer (the water-blocking Pb sheath) was incremented in several ways: from the alloys' composition choice to the realization of other supporting layers. In a previous work was demonstrated the beneficial effect of the application of a galvanized steel tape, which limits the radial expansion, thus deformations, owing to the warming up for Joule effect. Despite of that, during its winding, several irregularities arise on the underlying lead sheath and their effect on the fatigue life expectation is the main topic of this work. In particular, an irrelevant damaging impact was shown.

Contents

1	Introduction	9
1.1	Cable Construction Elements	10
1.2	Lead Alloys	13
2	Theory Review	17
2.1	Fatigue Phenomenology	17
2.1.1	Fatigue Test	18
2.1.2	Main Fatigue Laws	21
2.1.3	Notch Effect	24
2.2	Creep Phenomenology	29
2.2.1	Creep's Stages	30
2.2.2	Traditional Creep Laws	32
2.2.3	Practical Creep Laws	34
3	Model Calibration	36
3.1	Experimental Data	36
3.2	Best Fitting Curves	38
3.3	Creation of the Abaqus Model	41
3.3.1	Plastic Curve Definition	43
3.3.2	Mesh Creation, Loading Step and Outputs	45
3.4	Isight Optimization and Creep Parameters	48
3.5	Data and Results Resume	49
4	Specimens with Irregularity	53
4.1	Geometrical Properties	54
4.2	Models creation	55
4.2.1	Geometrical Modelling	55
4.2.2	Model Properties	57
4.3	Fatigue Intensity Factor	60
4.3.1	Time Frames Identification	61
4.3.2	Global Strains	64
4.3.3	Coffin-Manson-Basquin Interpolation	66
4.3.4	k_f Computation	71
4.4	Strain Intensity Factor	73
4.4.1	Most Solicited Point	74
4.5	Notch Sensitivity	78
4.6	Data and Results Resume	79

5	Irregularity Influence on the Real Configuration	82
5.1	Cable Section Geometry	83
5.2	Material properties	85
5.3	Mesh Creation	90
5.4	Boundary Conditions	91
5.5	Load Steps Definition	93
	5.5.1 Thermal Step Duration	95
5.6	Output Selection	96
5.7	Results and Intensity Factor	97
5.8	Data and Results Resume	102
6	Conclusions	104
A	Research Material	106
A.1	Example of Wrong Calibration	106
A.2	Irregularity Geometry	106
A.3	In-depth Analysis about k_f	109
A.4	Digital Image Correlation	113

List of Figures

1.1	Application of submarine power cable	10
1.2	Cable construction elements	10
1.3	Conductor design examples	11
1.4	Mass impregnated paper tapes	12
1.6	Pb-Sb phase diagram	15
1.7	Pb-Sn phase diagram	15
1.8	Pb-Sb-Sn phase diagram	16
2.3	Hysteresis cycle	20
2.4	Fatigue life phases for constant strain amplitude	20
2.6	Ramberg-Osgood law	22
2.8	Notch effect on stress-strain distribution	25
2.10	Notch effect on global stress-strain curve	26
2.11	Notch effect on the fatigue curve	27
2.13	Strain rate effect on the creep behaviour	31
3.1	Dimensioned specimen drawing	36
3.3	Fracture on a smooth specimen	39
3.5	Best fitting curves of experimental data	41
3.9	Symmetry conditions	43
3.10	Plastic curve compared with best fittings	44
3.11	Iterations on plastic curve choice	45
3.12	Result of mesh creation	45
3.13	Boundary conditions	47
3.14	Stress distribution on smooth specimen	48
3.15	Isight program	50
3.16	Comparison between simulations and scattered data	50
4.1	Specimens with irregularities	53
4.2	Irregular specimens geometries	54
4.3	Dimensioned irregular specimen drawing	56
4.4	DIC on irregular specimen	57
4.5	Selected points for displacement comparison	59
4.6	Time frames identification	62
4.7	$\varepsilon_g - N$ plot	65
4.9	Nominal stress range - N	66
4.11	Example of wrong Coffin-Manson interpolation	67
4.12	CMB interpolation	69
4.14	CMB fatigue curve	69

4.15	Global strain - N smooth and irregular specimen interpolation . .	71
4.17	Fatigue intensity factor	73
4.18	Most solicited points	74
4.19	Stress intensification on the back side	75
4.20	$\varepsilon_{max,eq}$ - Global strain	76
4.22	Strain intensity factors	77
4.24	Notch sensitivity	79
4.25	k_f , q and k_t plot	80
5.1	Irregularities example on the lead sheath	84
5.2	Axisymmetric model of the cable	85
5.4	Mesh on the cable section.	91
5.6	Period boundary conditions	92
5.7	Boundary conditions resume	93
5.8	Assembly detail	96
5.9	Preload stress on the steel tape	96
5.10	Detail of stress field on the Pb layer	97
5.11	Steel tape preload $\sigma_{PL} - \Delta T$	98
5.13	Equivalent strain in the most solicited point	100
5.15	Strain intensity factor	100
A.5	$\sigma - \varepsilon_g$ for smooth and irregular specimens	110
A.8	DIC system example	113

List of Tables

1.1	E-alloy composition	14
3.1	Experimental data for the smooth specimen	37
3.4	Best fitting parameters	41
3.6	Lead plastic curve	46
3.7	Average strain rate and duration for each simulation	47
3.8	Ramberg-Osgood parameters describing the simulation curves	49
4.1	Irregular specimens' geometries	55
4.2	Experimental data of irregular specimen	58
4.4	Average strain rate and duration for each simulation for the irregular specimens	59
4.5	Time frame identification for the smooth specimens	61
4.7	Time frame identification for the irregular specimens	63
4.9	Data for $\varepsilon_g - N$ plots	64
4.11	CMB parameters for the smooth specimens	68
4.12	CMB interpolation parameters for the irregular specimens	70
4.13	Fatigue notch factors	72
4.14	Average notch sensitivity	79
5.1	Cable section geometries	83
5.2	2D model section geometries	84
5.3	Layer A material properties	86
5.4	Layer B material properties	87
5.5	Layer D elastic material properties	88
5.6	Layer D plastic material properties	88
5.7	Layer E orthotropic elastic material properties	89
5.8	Layers F and G orthotropic elastic material properties	90
5.9	Layer H elastic material properties	90
5.10	Layer H plastic material properties	90
5.11	Thermal expansion step duration	95
5.12	Fatigue intensity factor in the real cable configuration	101
5.13	Percentage life loss estimation	101

Chapter 1

Introduction

The main target of this work is the life loss estimation of a submarine power cable, owing to the presence of geometrical irregularities on the lead sheath. This consists in the usage of a constant geometrical factor q (*notch sensitivity*), which for practical reasons was computed from simplified fatigue tests performed on hourglass-shaped lead specimens. For this reason, the first part of the work is focused on the study of the fatigue results of lead specimens. This allows to estimate q , which was then used in order to evaluate the percentage life loss in a real power cable configuration.

The submarine power cables have been used since the last century in different applications. Their design elements and the materials choice had been mainly done on the experience foundations and only in the last decades a research literature is growing upon this topic. In this chapter, a brief introduction about the main applications and construction elements of these systems is faced, with a more in deep discussion about the water-blocking Pb sheath and on the lead alloys' properties. The submarine power cables can be used in several situations and few examples are introduced [24]:

- Power supply to islands, where if the distance is closer than 30 *km* this cables are generally of *medium voltage* (≤ 52 *kV*);
- Offshore wind farms (OWP), where the distance between each wind turbine generators is near to 300 – 800 *m* (see Figure 1.1);
- Supply of marine platforms, where the power is usually produced from a local gas turbine at rather low efficiency.

In this work, the cables of interest are called HVDC (High Voltage Direct Current). These are in general characterised by a power transmission up to 600 *MW* with a voltage of about 500 *kV*. For this reason, these cables are subjected to remarkable warming owing to Joule effect, since a current of ≈ 1 *MA* flows on the conductor. Thus, starting from the power cable configuration studied in this thesis, the main construction elements are discussed and few other technological alternatives are introduced.

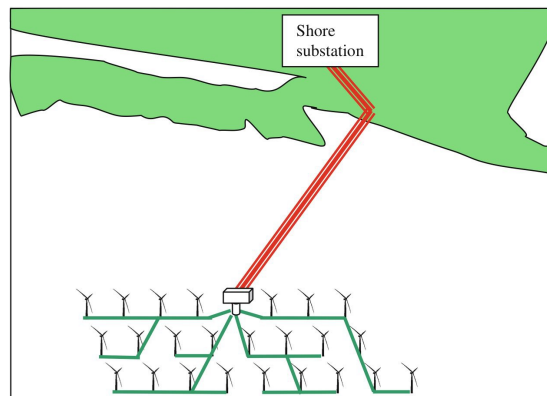


Figure 1.1: Layout of an offshore wind farm [24]

1.1 Cable Construction Elements

In the last decades a lot of different submarine power cable types have been used and tested in several context. Despite some differences between each configuration in terms of number of layers, geometries and materials, each of them has the same primary elements indicated in Figure 1.2 (which is the studied one in this thesis work). Here, only the most relevant layers are labelled, even if in between of each of them secondary layers and tapes are winded. In particular, the studied cable is made by 15 elements, which are listed in the following, starting from the most internal one [16]:

1. Conductor;
2. Carbon black paper tapes;
3. Insulation, which is the thicker layer after the conductor;
4. Carbon black paper and metallized paper tapes;
5. Copper woven fabric tape;
6. Lead sheath E-alloy;

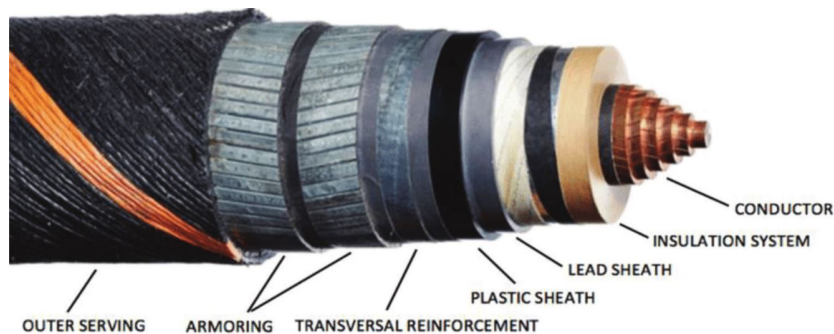


Figure 1.2: Nexans Norway cable section

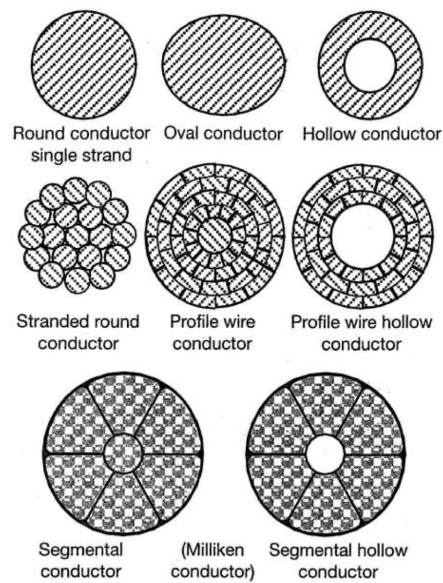


Figure 1.3: Conductor design [24]

7. Polyethylene (PE) layer;
8. Semi conductive nylon tape;
9. Galvanized Steel tape;
10. Semi conductive nylon tape;
11. Armour, galvanized Steel GR34;
12. Semi conductive nylon tape;
13. Armour, galvanized Steel GR34;
14. Plastic coated polyester tape;
15. High Density Polyethylene (HDPE).

Thus, a brief description of the main important of them is provided:

Conductor The conductor can be made of copper or aluminium. The last one has an higher electrical resistivity, a limited corrosion resistance and a lower density with respect to copper. On the sea floor, an heavier cable can be more stable and less excited by waves and currents, for which an *high purity copper* core is generally preferred.

The conductor is always placed at the cable centre and protected by the external layers, but depending on the specific application it can be made by wires of different shapes and profiles, as plotted in Figure 1.3.

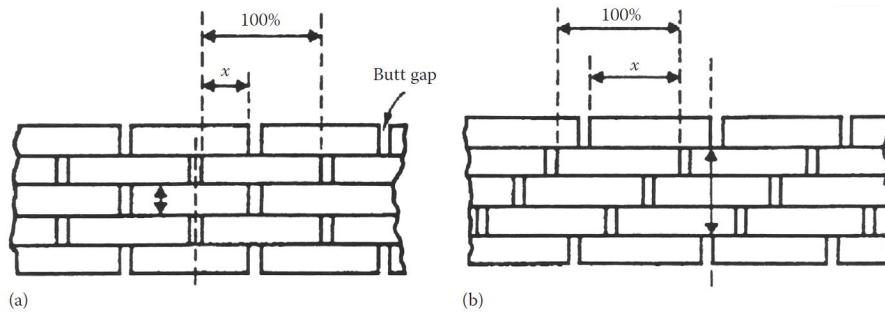


Figure 1.4: Mass impregnated paper tapes [8]

Insulation The conductor is always protected by an electrical insulation system, which avoids short circuits occurrence, that must be mechanically robust and resistant to the temperature, humidity and ageing. In the Nexans Norway's power cable this layer consists in *impregnated paper tapes*, also called *mass impregnated paper tapes* (MI), thus a mixture of Kraft paper and high viscosity impregnant (mineral oil T2015, which has a non-Newtonian rheological behaviour) [11]. This is the most common choice when HVDC cables are manufactured and a graphical representation of this layer is reported in Figure 1.4, where the paper tapes are wound in two different configurations. This is a delicate layer, "since strong thermal expansion could lead to high stress levels, while the pressure drops occurring during cable cooling might reduce the dielectric strength by introducing voids" [11]. Furthermore, in the operating conditions the dielectric strength is much higher than for the cold cable [24].

Another usual choice for the insulation layer consists in the *cross-linked polyethylene* (XLPE) layer. In any case, in order to obtain a smooth interface between the copper conductor and the insulation layer, the external *Carbon black paper tapes* are used. This, such as the other tapes, allows to reduce stress enhancement owing to local irregularities, which would reduce the dielectric strength. Other solutions can be more suitable for other specific applications [24].

Lead layer Externally to the insulation layer, the Water-Blocking Sheath is placed. As well as for the other layers, also in this case there are few different material choices, which are mainly:

- Lead (Pb);
- Aluminium (Al);
- Copper (Cu).

In particular, this thesis is focused on the study of this water-blocking layer, which is made by a lead alloy called *E-alloy*. Its composition and mechanical properties are a discussion topic of the next subsection.

Steel tape The galvanized steel tape is used in order to provide radial sustainment, which is necessary during the thermal expansion of the inner layers.



Figure 1.5: Three-phase submarine cable with double-layer round wire rock armoring [24]

In particular, the MI-paper has an high thermal expansion coefficient, which would lead to unbearable deformations especially for the lead layer. Among this and the other steel components the *semi conductive nylon tape* allows to reduce the stresses from a direct contact, further than reducing the frictional coefficient.

Armoury Finally, the tension stability (mainly during installation, where tensional forces owing to the cable weight could exceed lead resistance) and mechanical protection are provided by the *armoury*. This consists in a series of steel wires with helical disposition placed externally to the steel tape, and an example of a cable with a combination of layers called *rock armoring* is reported in Figure 1.5. Several solutions in terms lay length and consequences can be found [24]. In particular, in the Nexans Norway cable, a *rock armoury* is used, where the first set of galvanized wire steels (thus the most internal one) has an angle of 12.7° with respect to the axial direction, while the second layer has an angle of -10.5° [16].

Finally, a brief description of the main lead alloys and of the used one for the water-blocking layer is faced.

1.2 Lead Alloys

In order to improve the fatigue performances of the submarine power cables, the usage of the steel tape was demonstrated to be useful [16]. Despite of that, the tape winding origins some irregularities on the lead sheath, which is a very soft and ductile material. This thesis faces the influence of these irregularities upon the fatigue life of the power cable, thus is focused on the lead layer. For

Table 1.1: E-alloy composition [12]

Pb	Sn	Sb
99.3	0.45	0.25

this reason, a brief section is dedicated to the description of the main lead alloys properties, further then a more in deep discussion about PbSnSb alloy (also called *E alloy*), which is the adopted one. In particular, its composition is reported in Table 1.1.

Pure lead is never used and it's commonly alloyed with other elements in order to improve its mechanical and electrochemical properties. Usually binary phase diagram are introduced, thus tertiary alloys are discussed. All the following figures, data and discussions were resumed from Reference [10].

Pb Binary Alloys

Pb binary phase diagrams are classified into four main groups, in function of the compatibility between lead and the alloying elements in terms of atomic size, electronegativity and valence. In particular, the group of interest (called *Group 2*) involves alloys mainly made by Sn, Sb, As and Ag.

Since the used lead alloy contains tin (Sn) and antimony (Sb), their binary phase diagrams and main properties are discussed:

- Antimony is used in order to create Pb-Sb alloys with *high tensile strength*, *resistance to fatigue* and *high hardness* with respect to the pure lead. Usually, the adopted Sb percentage is in between 1 ÷ 13%. Owing to their properties, these alloys are usually used for pipe and cable sheathing.

The phase diagram is plotted in Figure 1.6, while more in-deep discussions about the mechanical (such as *age hardening* for alloys with greater than 3.5% Sb) and material properties can be found in Reference [10];

- Pb-Sn alloys containing up to 3% Sn are used in cable sheathing and its phase diagram is reported in Figure 1.7 [10]. Furthermore, lead alloys low in tin are used for their *higher corrosion resistance*. Further informations can be found in Reference [10].

Antimony and tin effect can be combined in order to create ternary alloys.

Pb Tertiary Alloys

Pb-Sb-Sn alloys are the mostly used in cable sheathing (owing to their fatigue and corrosion resistance) and its phase diagram is plotted in Figure 1.8. In particular, *alloys E* are the most common and their chemical composition is around 0.4% Sn and 0.2% Sb, together with a negligible percentage (usually < 0.01%) of other elements like Cu, Bi, and Ag [10]. The mechanical behaviour of this alloy is characterised by a significant thermal activated plastic flow (creep). Indeed, even when its working at room temperature conditions, it has an *homologous temperature* around 0.5 [10]. Furthermore, recovery and recrystallization (which is sensitive to the amount of prior deformation and

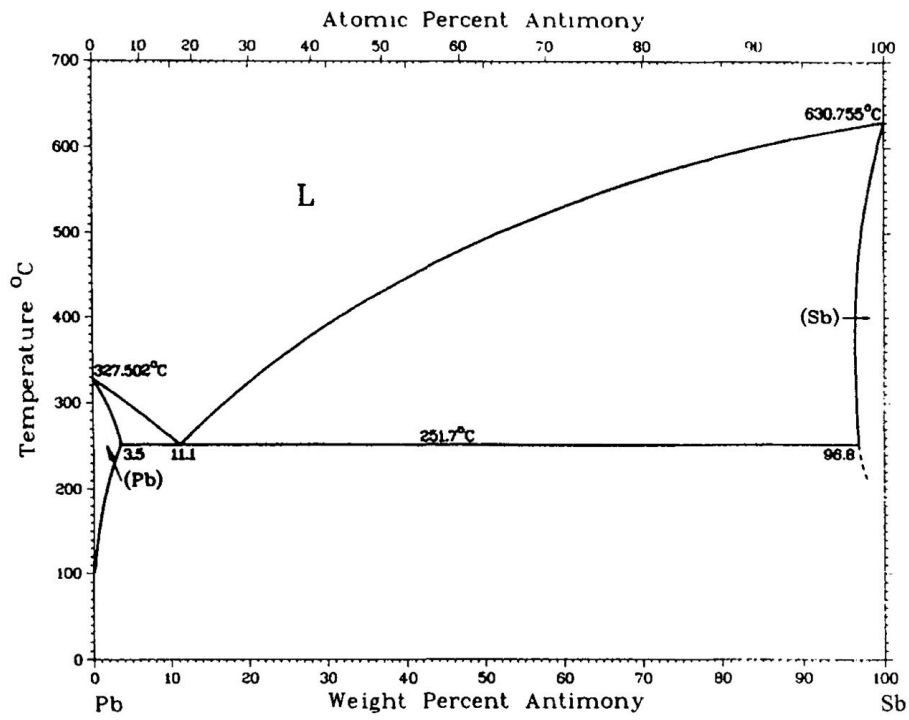


Figure 1.6: Pb-Sb phase diagram [10]

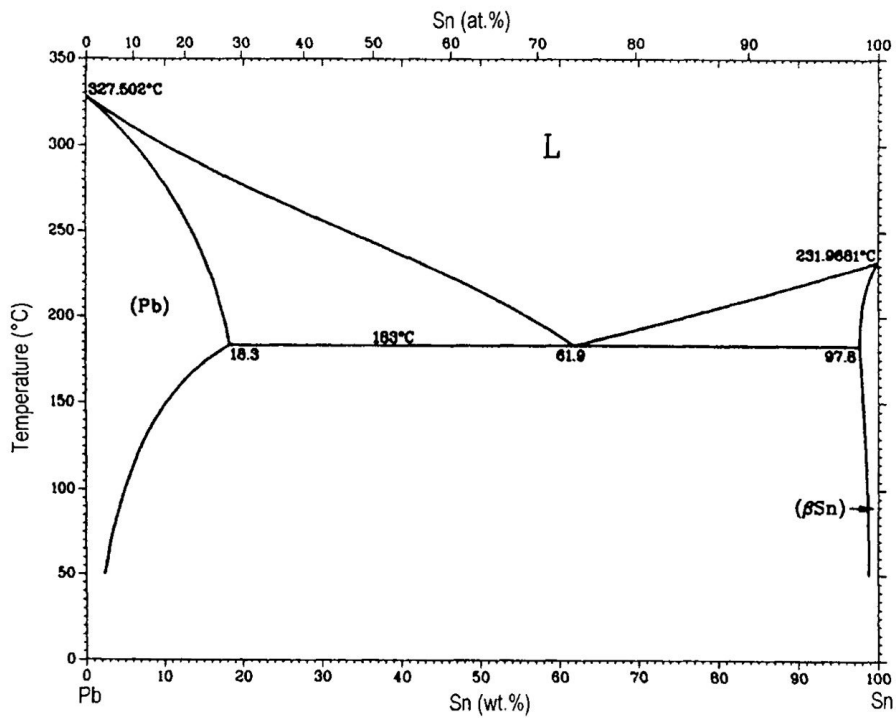


Figure 1.7: Pb-Sn phase diagram [10]

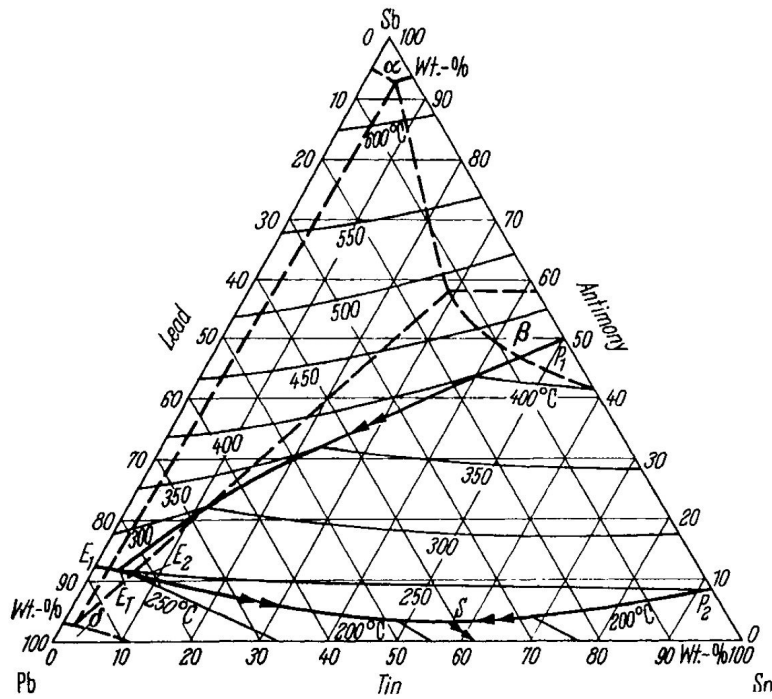


Figure 1.8: Pb-Sb-Sn phase diagram [10]

operating temperature, and it can be slowed by the presence of Sn) are the other main peculiarities of lead alloys. Since the lead behaviour is strongly time dependent, tensile and fatigue tests are usually performed at different strain rates. Again, further informations can be found in Reference [10].

After this brief introduction to the topic of the thesis, a review of the main important theoretical aspects is introduced. In the next section, all the arguments which were useful during the thesis development are contained.

Chapter 2

Theory Review

The aim of this brief section is not to explain and resume every aspect of fatigue theory, but to review elements and topics which were faced during the thesis development. In particular, the following sections are introduced:

- Fatigue phenomenon:
 - Tests peculiarities;
 - Local behaviour;
 - Main fatigue laws;
 - Notch effect.
- Creep phenomenon:
 - Creep stages;
 - Main traditional creep laws;
 - Time-hardening and strain-hardening problems.

2.1 Fatigue Phenomenology

Seeing as in the real-world service components are always subjected to cyclic loads (which can vary in amplitude and frequency), thermal stress and other conditions, a *statical design* is almost never enough. Thus, in order to describe the materials behaviour and their response in the most recurrent set of variables a new theory must be studied and fitted for each occasion. Creep is an example, which theory tries to describe how materials are behaving when they are working in high temperature conditions. Fatigue is another main theory which describes how materials are behaving when they are not solicited by monotonic loads. Indeed, their response is always time dependent and, if this peculiarity has enough time to show up, new breakdown phenomenon are arising. Furthermore, the fatigue failure is apparently brittle as it is not preceded by large plastic deformations. Since few signs of failure are evident in this phenomenon, several studies during the last centuries were conducted, in order to understand which is the failure cause and how to predict fatigue failure in several working conditions.

Starting from a brief explanation of the fatigue testing conditions, few main aspects of theory were described, like S-N curve and Coffin-Manson-Basquin

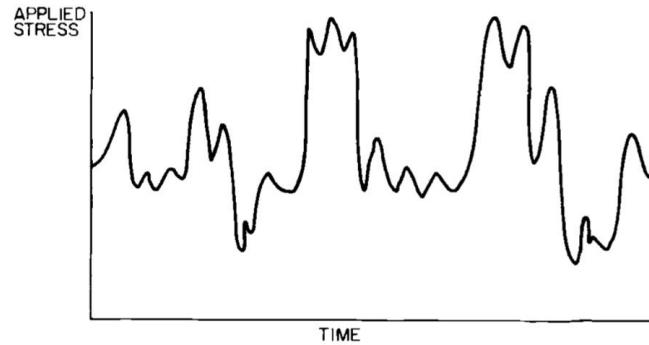


Figure 2.1: Random load example [3]

equation, crack propagation stages, hysteresis loop and notch effects in fatigue life.

2.1.1 Fatigue Test

During production, installation and service, the submarine power cable is excited by axial forces, bending, torsion and contact loads with a random sequence and amplitude. Since each kind of load has a different effect in fatigue life, it would be useless to test a cable's section by means of a random excitation. Thus, in order to understand fatigue physics, tests are usually conducted in more simplified situations, in which a single load type is considered. In this case *axial fatigue test* is used. This is useful to describe locally both axial and bending loadings, since also in bending the lead fibres are solicited by traction and compression.

Depending on the stress and strain amplitude, *fatigue* can be distinguished in two main fields:

- HCF & VHCF are *high cycle fatigue* and *very high cycle fatigue*. These conditions occur when the stress is small and minor than yield stress, thus when the plastic deformation is negligible and the elastic one predominant. In this case the reference entity for studying the fatigue life is usually the *stress*;
- LCF is, in the opposite, the *low cycle fatigue*. In this case, the *strain* becomes the reference variable since a non linear relation between stress and strain arises and, in plastic field, the strain allows to clearly distinguish different stress conditions.

A generic cyclic load in the HCF domain (represented in Figure 2.2) is generally characterised by the *minimum stress* σ_{min} , the *maximum stress* σ_{max} , the *mean stress* σ_m , the *stress amplitude* σ_a :

$$\sigma_a = \frac{\sigma_{max} - \sigma_{min}}{2} \quad (2.1)$$

(or s_a in the case of engineering stress), the *stress range* $\Delta\sigma$ and the *period* T . Furthermore, the *stress ratio* $R = -\frac{\sigma_{min}}{\sigma_{max}}$ is usually used to distinguish different

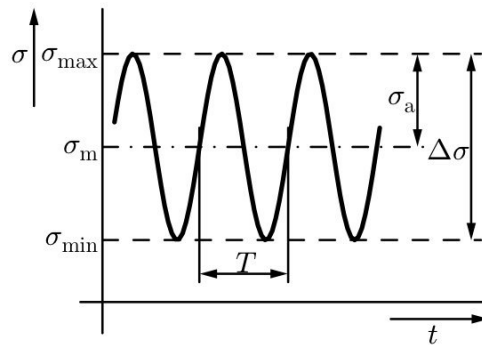


Figure 2.2: Cyclic load [22]

fatigue tests. In the case of lead alloys, which behaviour is better described by LCF domain (being lead characterised by a wide plastic field and a low yield point), the *strain ratio* is more used and the case of $R_\epsilon = -1$ is the most frequently adopted. In LCF cases, where the predominant strain consists in the *plastic strain*, the fatigue tests are performed in *deformation control*. For this reason ϵ becomes the reference entity in the fatigue behaviour at LCF conditions.

If, like for lead (Pb), the material response is also time-dependent (for instance owing to creep phenomenon influence), several tests are usually carried on at different applied global strain range and strain rates. In this way also time dependency can be highlighted. During a single test, several entities are generally collected:

- s is the *engineering stress*, which can be computed by the load cell on the narrowest specimen's section A_0 ;
- ϵ is the *real strain*. Depending on the testing conditions and on the specimen geometry it can be computed locally, as it was done in the following for the smooth specimen, or on a longer segment (like for the specimen with irregularity). In these experiments the Digital Image Correlation (DIC) was used (see Appendix A.4). Indeed, owing to the wide plastic field which characterises the lead, the measurements performed by the testing machine could be not accurate;
- $\dot{\epsilon}$ is the *strain rate* and it can be measured by DIC technique on the same region where ϵ is considered. For the same reason discussed for ϵ , this could be different from the strain rate imposed by the testing machine;
- N is the number of cycles in which the failure has occurred. Conventionally, *failure* means a stress which is usually in between 20% and 40% of the nominal stress measured at half life (thus for the stabilised conditions) [20, 23];
- R , which is the last collected parameter and must be distinguished by the stress or strain ratio, means *run-out*. This is 0 if specimen has failed during the test, 1 if it has survived and the test was stopped at a certain number of cycles.

Thus, the stabilised hysteresis loop is introduced.

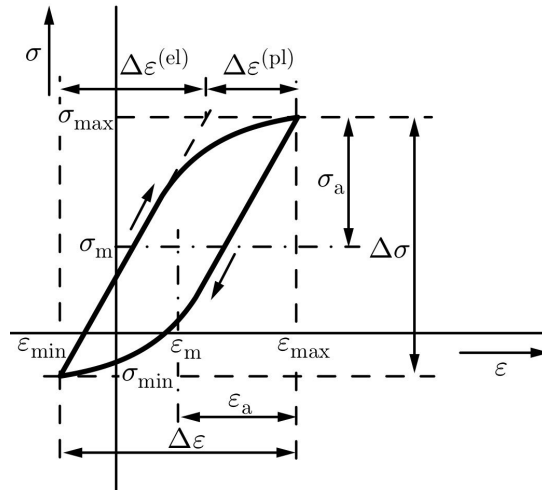


Figure 2.3: Hysteresis cycle [22]

Stabilised Hysteresis Loop

Usually, the engineering stress and the real strain of a single test are plotted in a $\sigma - \epsilon$ plot (see Figure 2.3). The hysteresis loop described by this plot is covered from the specimen at each stabilised cycle and from it the engineering stress range Δs and the real local strain range $\Delta\epsilon$ can be computed. Thus, owing to the strain ratio $R_\epsilon = -1$, the *stress amplitude* $s_a = \frac{\Delta s}{2}$ and the *strain amplitude* $\epsilon_a = \frac{\Delta\epsilon}{2}$ are known for each fatigue test.

Even if generally a single hysteresis cycle is plotted (which is called *stabilised hysteresis cycle*), owing to the crack nucleation and propagation the specimen or any other component changes its response during its life, as it can be seen in Figure 2.4. In particular, if the fatigue test is performed at constant strain

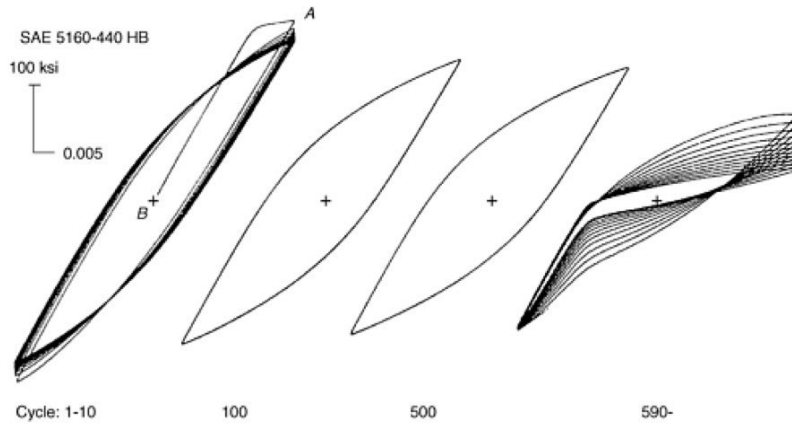


Figure 2.4: Fatigue life phases for constant strain amplitude [2]

amplitude ϵ_a and the stress is computed on the initial resistant section A_0 , three different phases can be observed:

1. During the first few cycles, the material generally faces cyclic *hardening* or *softening*. These phenomenon are due to the dislocation movement during the cyclic loads. The first one occurs in metals with an initial low dislocation density and it's caused by the multiplication of dislocations. In the opposite side, an high strength material typically faces softening, which consists in the dislocation rearrangement and annihilation;
2. After the first phase, the hysteresis cycle generally remains almost the same for large part of its life (with a light and continuous resistance decreasing). In these cycles, the crack nucleation is occurring, but the infinitesimal discontinuities are not affecting the cross section, and so the material resistance. Further informations about the crack nucleation, which main stages are summarised in Figure 2.5, can be found [22];

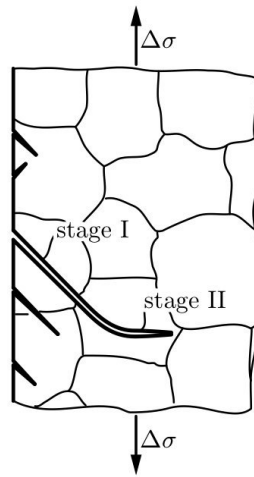


Figure 2.5: Fatigue life stages [22]

3. During the last phase, material's response is changing rapidly. The crack at stage II in Figure 2.5 starts propagating as in fracture mechanics (following *Paris' law*) and it causes progressive resistance decreasing owing to the cross section reduction. For this reason, the material life is mostly characterised by the crack nucleation, while the crack propagation occurs in a small percentage of the total number of cycles.

The main interest in the specimen behaviour is covered by the second phase, where the material properties have an engineering interest and more or less constant at each cycle. Finally, the specimen life is generally described by the Coffin-Manson equation, which allows to predict the number of cycles prior to rupture. These and other aspects are faced in the next subsection.

2.1.2 Main Fatigue Laws

Since the material response is different in all the stress-strain operative conditions, several tests at different global strain ranges must be performed. Thus, since time has an influence on the results, for each set of data a constant

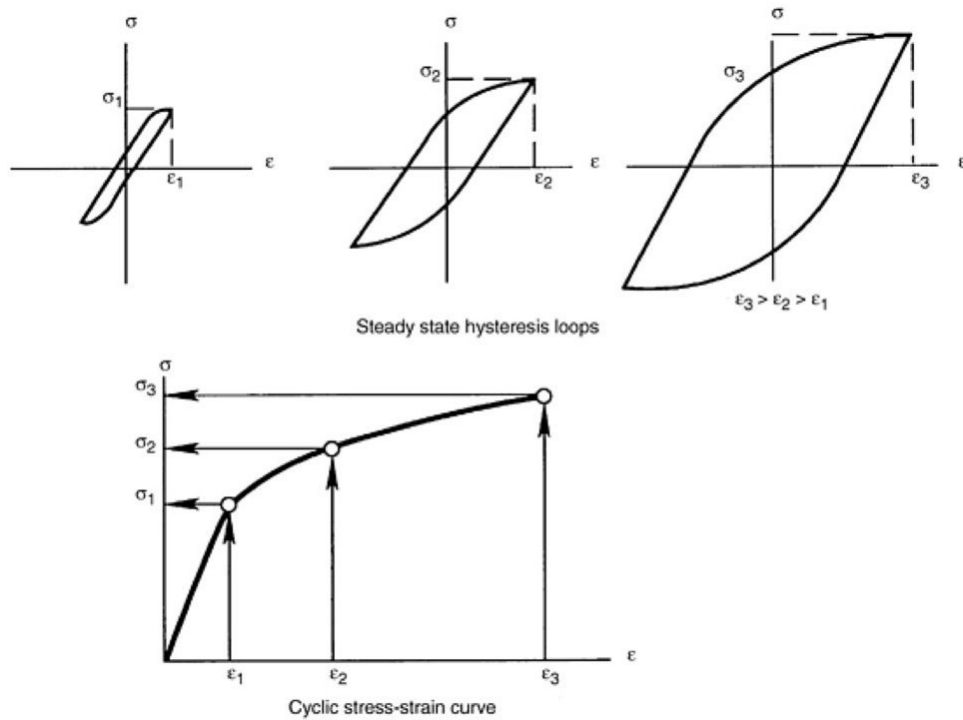


Figure 2.6: Cyclic curve construction by means of different test [2]

strain rate is used. By this way, a different hysteresis cycle for each test is obtained and all of them are usually plotted on the same chart (one for each strain rate condition) in order to highlight their relationship, as plotted in Figure 2.6.

Ramberg-Osgood

In particular, every steady state hysteresis loop can be summarised in a single curve, called *cyclic stress-strain curve*. Each point of this curve, which is generally described by the *Ramberg-Osgood* Equation 2.2, coincides with the vertices of a single hysteresis loop, thus it represents one experimental test [22]:

$$\varepsilon_a = \frac{\sigma_a}{E} + \left(\frac{\sigma_a}{k'}\right)^{1/n'}. \quad (2.2)$$

Where E is the Young modulus, while k' and n' are material constants.

This equation is written in the same format of the monotonic traction curve, made by Hook's elastic and Holomon's plastic components. It was chosen because it's able to properly fit the experimental fatigue data, considering that the material constants k' and n' are different from k and n , valid for the monotonic curve. The reason of that is in the hardening or softening that the material could face during the first few cycles of its life, which could cause an arising or decreasing of the cyclic curve with respect to the monotonic one.

Ramberg-Osgood equation is used to perform FEM simulations of cyclic loadings, since performing the simulation of each hysteresis cycle would request a

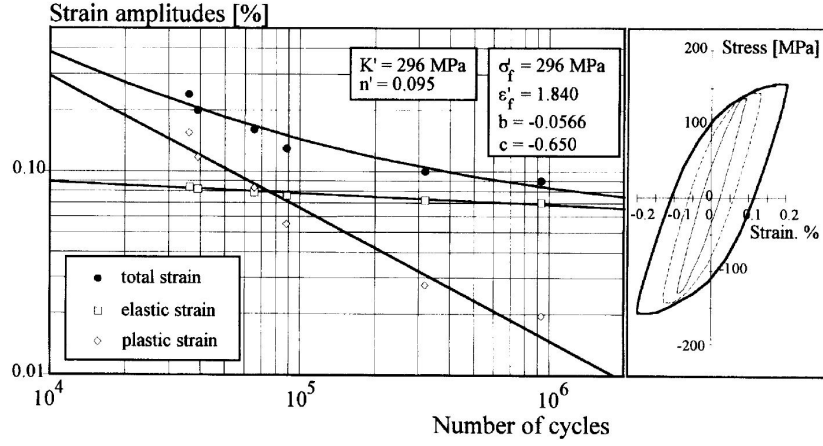


Figure 2.7: Coffin-Manson-Basquin plot (S-N) with elastic and plastic term [20]

huge computational capability. It's known that this kind of simulations allows to represent the stress-strain field in the component in a suitable and representative way. Thus from the cyclic curve it can be extracted the results for all the possible fatigue testing conditions in terms of applied strain amplitude.

Coffin-Manson-Basquin

When the stress-strain field is known and well represented, it's usually linked to the number of cycles to failure of the specimen. In this way, the life estimations can be performed. This is done thanks to Coffin-Manson-Basquin Equation 2.3, which links the *number of cycles* N (or *reversal to failure* $2N_f$) to the *global strain amplitude* ε_a [22]:

$$\varepsilon_a = \frac{\sigma'_f}{E} \cdot (2N_f)^{-a} + \varepsilon'_f \cdot (2N_f)^{-b}. \quad (2.3)$$

This equation considers that the global strain amplitude consists of two terms, the elastic and the plastic one. The first term (which is defined by the material constants σ'_f and a) is predominant for large numbers of cycles (HCF) and it corresponds to the Basquin equation. The second is the Coffin-Manson term, which gives a good approximation of the life duration for a small number of cycles (thus in the LCF domain). Here:

- ε'_f is the *fatigue ductility coefficient*;
- b is the *fatigue ductility exponent*, which depends on the material hardening.

An example of CMB interpolation is given in Figure 2.7, where the plastic and elastic strain components are separately considered. This means that the global strain amplitude is separated in its two components $\varepsilon_g = \varepsilon_{el} + \varepsilon_{pl}$. These are plotted with N and separately interpolated. The sum of the two curves obtained represents the effective *fatigue curve*. In particular, the plastic contribution is smaller than the elastic one at high number of cycles, while is predominant in LCF, where it influences the curve slope.

The Coffin-Manson-Basquin equation (CMB) as written in Equation 2.3 is valid in the case of mean stress $\sigma_m = 0$. If this isn't true, several corrections to this law were proposed. One of the most used is called *Morrow hypothesis*. This consists in considering the effect of the mean stress only in the elastic component of the CMB equation $\varepsilon_a^{(el)} = \frac{\sigma_f - \sigma_m}{E} (2N_f)^{-a}$. In this way, if the mean stress is positive (traction) the component's life is reduced, as the crack nucleation and propagation are facilitated.

Furthermore, all these considerations are valid just in the case of smooth specimens. If notches are present, the notch effect in terms of *notch factors* and *notch sensitivity* must be considered.

2.1.3 Notch Effect

When a specimen with an irregularity or a generic notch is considered, the experimental evidence is that its life is reduced with respect to the smooth specimen in the same testing conditions. For this reason, the notch effect must be considered in predicting the fatigue life, since it facilitates the crack nucleation and propagation. This section is organised in the following steps:

- Stress concentration factor k_t in statical conditions;
- Fatigue concentration factor k_f ;
- Notch sensitivity q .

Stress Concentration Factor

Every notch or irregularity always causes stress and strain redistribution and intensification at the notch root. This *local effect* is usually explained and debated by means of a *concentration factor*. If the specimen is working in the elastic field, this is called k_t and it's defined at constant net section stress (or nominal stress) in the following way:

$$k_t = \frac{\sigma_{max}}{\sigma_{nss}}, \quad (2.4)$$

where σ_{max} is the maximum stress value in the notch root, while σ_{nss} is the *net-section stress*, thus the stress computed in the restricted section. If σ_{max} overcomes the yield point, the stress concentration factor in Equation 2.4 is not any more valid and the deviation from the linearity of the monotonic curve must be considered. When the local plastic deformations are involved, but the other sections are still working in the elastic field, the elastic stress intensity factor is divided into two different intensity factors:

$$k_\sigma = \frac{\sigma_{max}}{\sigma_{nss}}, \quad k_\varepsilon = \frac{\varepsilon_{max}}{\varepsilon_{nss}}.$$

Where k_σ is the *stress intensity factor* and k_ε is the *strain intensity factor*. These values are always valid in correspondence to the notch root and their difference is explained in Figure 2.8, where is evident that the deviation from the linear-elastic behaviour blocks out the linear proportionality between the stress and strain. Since in the case study all the specimen is working in the plastic fields, the stress and strain intensification factors were used in the following with

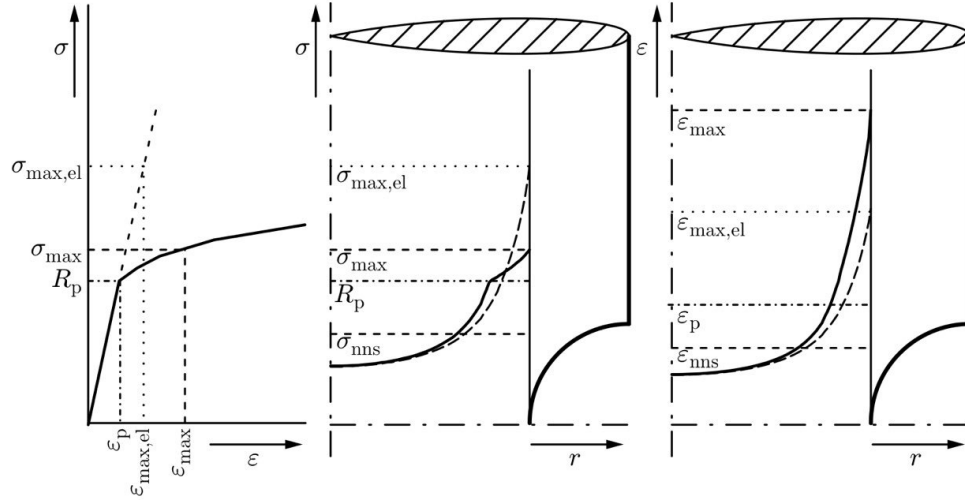


Figure 2.8: Notch effect on stress-strain distribution [22]

a different definition. Even if in general the stress concentration factor is the mostly used, when the material has a wide plastic field it could be more relevant the *strain intensity factor* in all the stress-strain conditions.

Furthermore, k_σ and k_ϵ are linked each other by means of the *Neuber's law*:

$$k_t^2 = k_\sigma \cdot k_\epsilon. \quad (2.5)$$

This rule allows, in a first approximation, to compute the maximum stress and strain values at the notch root, but it's not an accurate design tool, since it could overestimate the notch effect. A correction to this law was proposed in the case of creep loading $k_t^{0.9 \div 1.5} = k_\sigma \cdot k_\epsilon$ [23]. Another reason for which Neuber's rule is not an optimal design tool in the fatigue domain resides in the crack nucleation and propagation mechanics. Indeed, the stress and strain concentration factors are valid at the notch root. Thus the stress and strain values computed in this way are perceived by the crack just during its nucleation, while during the propagation, the crack enters in a less solicited region. This problem can be considered and studied in a more accurate way by measuring the crack length during the fatigue tests [20].

Further than the *local* effect of notches, which is studied by means of the concentration factors, these irregularities have also a *global* effect. Material properties are the same of the smooth specimen and each infinitesimal element of it is covering the same plastic curve, but (being the volume near the notch more solicited) each element along the specimen is on a different point of the plastic curve. For this reason, as shown in Figure 2.10, measuring the global strain rather than the local one could lead to observe another traction curve, which is characterised by different RO parameters and by an *apparent* Young's modulus. These are not *real* parameters, but they are just a consequence of the localised stress and strain intensification. This curve is obtained when the measurement segment L_0 in Figure 2.9 is enough far away from the notch, so that the obtained curve becomes a global property of the notched specimen. This situation is the only one that can be compared with the smooth specimen

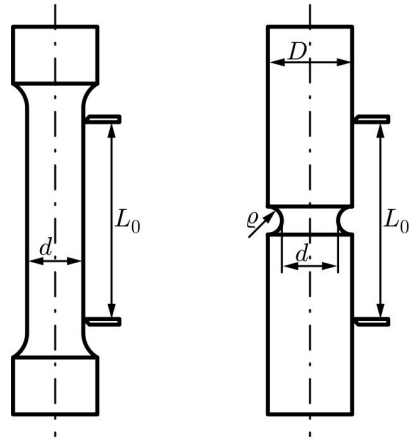


Figure 2.9: Different measurement locations for Figure 2.10 [22]

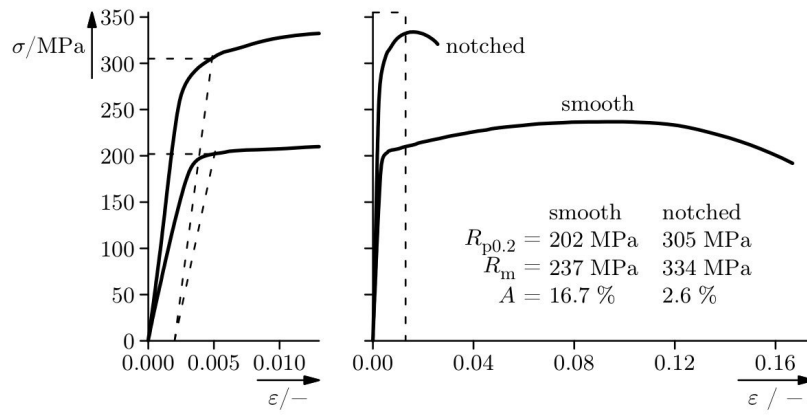


Figure 2.10: Notch effect on global stress-strain curve [22]

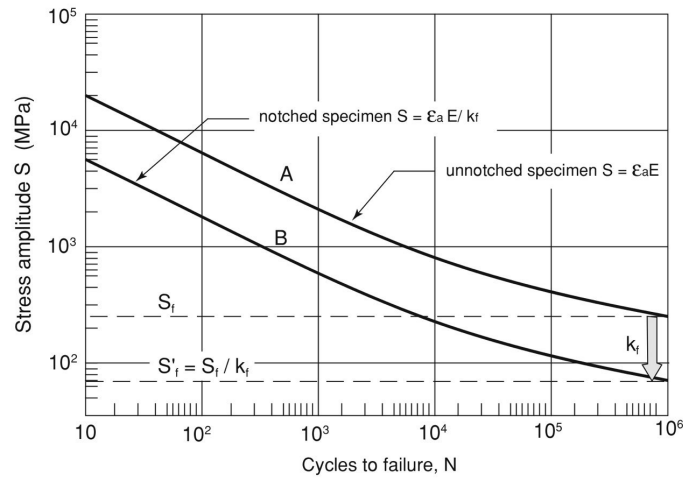


Figure 2.11: Notch effect on the fatigue curve [20]

curve, since both are obtained for the same *global strain*.

If the notched curve doesn't change significantly when the strain is measured on a longer length than L_0 , the same thing is not true for the shorter ones. Indeed, being the plastic curve the same of the smooth specimen, if L_0 gradually focus on the notch, the measured curve moves step by step upon the smooth one. For this reason, when dealing with a notched specimen, it's important to measure the strain along an appropriate length (so that the obtained curve is independent from the measurement point). Otherwise, the notched $\sigma - \varepsilon$ curve wouldn't be reliable and comparable with the smooth specimen results, since the measured strain wouldn't be equal to the global one.

If when a static design is needed k_σ and k_ε concentration factors are the only required, when the target is the notch influence in the fatigue domain new entities must be introduced.

Fatigue Notch Factor

In the fatigue domain notches generally reduce the number of cycles to failure N if a comparison between smooth and notched specimens is performed on a $\sigma_{nss} - N$ plot (see Figure 2.11). Thus, the *fatigue notch factor* is introduced at constant number of cycles N :

$$k_f = \frac{\sigma_{c,smooth}}{\sigma_{c,notch}}, \quad (2.6)$$

where $\sigma_{c,smooth}$ is the *fatigue limit* for the smooth specimen, while $\sigma_{c,notch}$ is the fatigue limit of notched bodies [22]. This definition is the most used one and it's valid in the HCF domain, where a constant k_f is introduced and it's defined for $N = 10^6$ cycles. The fatigue notch factor allows to perform a fatigue design by means of the *real fatigue curve*, thus the one of the smooth specimen. Indeed, the fatigue curve of the notched specimen generally is not provided, since its existence is hidden behind the k_f .

Its meaning is different from the previous stress and strain intensification factor

k_t . Indeed k_t describes a local condition (thus it allows to compute the local maximum stress and strain values), while k_f describes the notch perceived effect, but it doesn't allow to compute the exact stress and strain values on the notch root in the fatigue domain.

Even if the two definitions are different, the stress intensification factor k_t applied to the fatigue domain with the same definition of k_f has the effect to overestimate the damage introduced by the irregularities or notches. Thus, the relation between these notch factors is $1 < k_f < k_t$. Being $k_f > 1$, the life of notched specimens is anyway always shorter than the life of the analogous smooth specimen. Using a constant fatigue notch factor for all the number of cycles means that the fatigue curve of the notched specimen is considered to be translated by a constant multiplying factor with respect to the smooth specimen fatigue results. This simplification is not always valid, since the material response to notch could be different in function of the applied stress and strain. For this reason, if the specimen or component is working and failing in the Low Cycle Fatigue domain, the fatigue notch factor can be defined in a different way [4, 18]:

$$k_{f,N} = \frac{\sigma_{n,smooth}}{\sigma_{n,notch}}. \quad (2.7)$$

In this case k_f is defined on the fatigue curve by means of the *net section stress amplitude* at a certain number of cycles to failure N , which is different from $N = 10^6$ used in the HCF domain, as shown in Figure 2.11. Generally the value of $N = 10^3$ is a choice for the reference fatigue notch factor in the LCF domain $k_{f,10^3}$ [18]. This choice is arbitrary and it depends also in the material properties. Indeed, the LCF domain is defined for the occurrence of plastic behaviour in the fatigue life and this could happen even at an high number of cycles for the most ductile materials. The lead, for instance, has plastic deformation also at $N = 10^6$, which means that its behaviour is always interested by the so-called LCF domain.

Even if the notch fatigue factor is defined taking into account the *stress* values, in the forward discussions the same definition was used with the *strain* values:

$$k_{f,N} = \frac{\varepsilon_{g,smooth}}{\varepsilon_{g,notch}},$$

being the lead response affected by a wide plastic field, which wouldn't allow to clearly see the notch effect from the stress point of view [4]. For this reason, $\varepsilon_g - N$ plots (where ε_g is the global strain) are considered instead of $\sigma_{nss} - N$.

In such plots the *fatigue curves* are usually described by the Coffin-Manson-Basquin equation and for this reason the *global strain* on the notched specimen must be correctly computed, as discussed in the previous section. Furthermore, also in this case the *fatigue notch factor* is defined at constant number of cycles and it could be different for each N value [18]. Thus, the fatigue curve of notched specimens in Figure 2.11 in the reality is almost never translated from the un-notched curve by the same notch factor in every point. Despite of that, the value at $N = 10^6$ is usually chosen as constant since it allows to simplify the damage computations in all the stress and strain domain. Further discussions about its computation were faced during the thesis development and they are gathered in Section 4.3.4 and in Appendix A.3.

In the same way done for the *static intensity factor*, Neuber's law can be

extended to the *fatigue notch factor*:

$$k_f^2 = k_\sigma \cdot k_\varepsilon,$$

where, being in LCF domain, k_f is applied to the global strain amplitude [4]. As already said, Neuber's law is not an accurate design tool. Indeed, depending on the phenomenon involved in the study, it could overestimate or underestimate the notch effect. Few corrections, considering the underestimation ($\zeta > 1$), were proposed $k_f^2 = \zeta \cdot k_\sigma k_\varepsilon$ [4]. Finally, the linkage between k_t and k_f is usually studied by means of the *notch sensitivity factor* q .

Notch Sensitivity Computation

The *notch sensitivity factor* q is the geometrical parameter which usually allows to compute k_f from k_t and it's defined in the elastic field as:

$$q = \frac{k_f - 1}{k_t - 1}, \quad (2.8)$$

where $q = 0$ when $k_f = 1$, thus if the specimen is indifferent to the notch presence, and $q = 1$ when $k_f = k_t$.

As well as k_t , also the notch sensitivity factor is usually considered as dependent only on the notch geometry and material properties. Despite of that, if the material is working under plastic conditions and the fatigue curve is described in a wide range of N , q could be dependent both on the global strain (which takes the place of σ_{nss} , through k_t and k_ε) and on the number of cycles to failure (through k_f). For this reason, the Equation 2.8 was extended to more general conditions as:

$$q = \frac{k_{f,N} - 1}{k_\varepsilon - 1},$$

where k_f could be considered anyway constant (see Appendix A.3) and k_ε can be computed in all the plastic field by means of FEM analysis. In this conditions q is depending only on the global strain through k_ε , even if the computation of a constant value (which can be easier used) is the target of this work.

Concluded the section regarding to the fatigue phenomenon, a brief section about *creep* is introduced.

2.2 Creep Phenomenology

Creep is a phenomenon which explains time-dependent plasticity. This behaviour occurs if a metal or a ceramic component is loaded at high temperatures, usually between $0.3 T_m < T < T_m$, where the melting temperature is expressed as *absolute temperature*, in K . Thus, it's evident that a large amount of materials, as lead ($T_m \approx 600 K$ [6]), are working in creep field also at room temperature [12]. Since a creep response was highlighted in the following work, a brief review about the main theoretical aspects of this phenomenon is discussed. In particular, this section is organised in the following points:

- Creep stages;
- Main traditional creep laws;
- Time-hardening and strain-hardening problems.

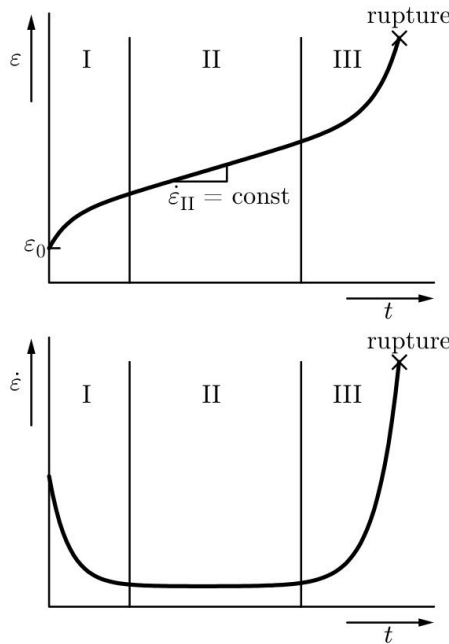


Figure 2.12: Plot of the strain and strain rate versus time [22]

2.2.1 Creep's Stages

Materials' behaviour in these conditions is usually introduced with a $\varepsilon_p - t$ plot, evaluated at constant stress and fixed temperature, as reported in figure 2.12. These results are the output of the usual *constant tensile load creep test*, which is the mostly used in order to provide creep data and it's the most simple situation which allows to understand the basic behaviour of different metals, alloys and ceramics in creep conditions.

If a specimen or a generic component is solicited by an external constant load at high temperature, its response can be generally distinguished in three different regions. In the first one, called as stage-1 or *primary creep*, the plastic deformation starts from the statical value ε_0 , owing to the monotonic plastic response and it increases in time by a decreasing strain rate, also called *creep rate*, $\dot{\varepsilon} = d\varepsilon/dt$. The creep behaviour arises even if the applied stress is lower than the yield point measured during the tensile test and, in this case, the plastic time dependent deformation would start from $\varepsilon_0 = 0$. Indeed, also the yield point measured during the creep tests is strain rate dependent and its value is decreasing for lower strain rates (as shown in Figure 2.13).

Yield Stress The variation of the yield stress with respect to the strain rate and the temperature is usually studied by means of the *stress sensitivity* exponent N [14]:

$$N = \left[\frac{\partial \ln \dot{\varepsilon}}{\partial \ln \sigma} \right]_{T,s}.$$

At high temperatures the value of N decreases, which means that a variation of the strain rate affect more the flow stress (see Figure 2.14).

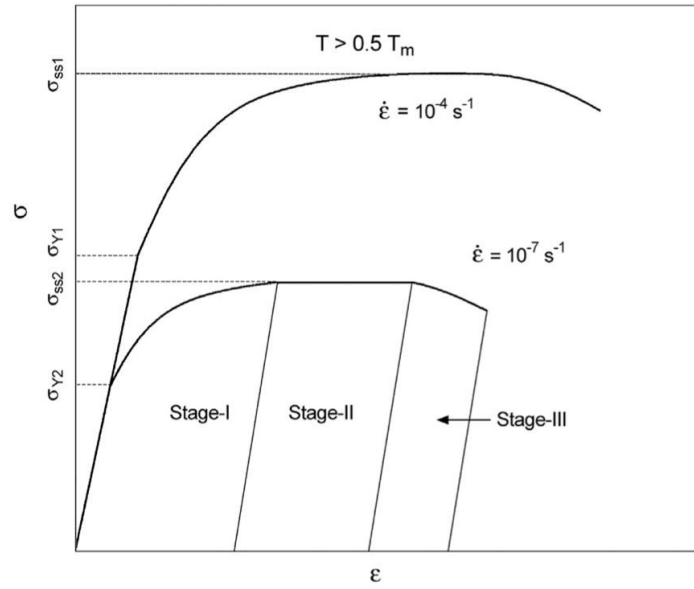


Figure 2.13: Strain rate effect on the creep behaviour [14]

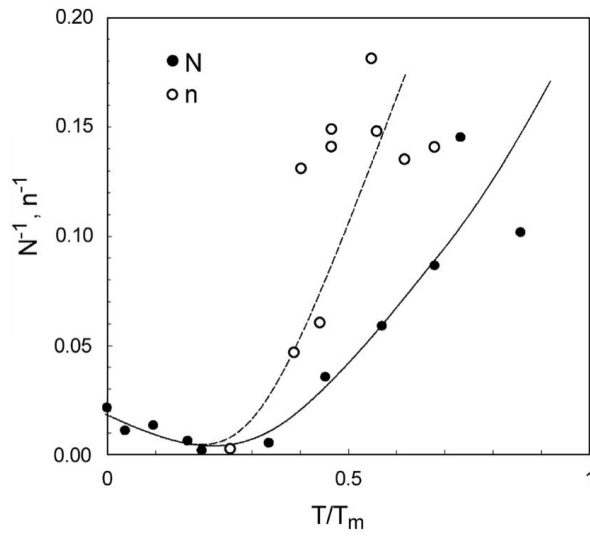


Figure 2.14: Stress sensitivity exponent [14]

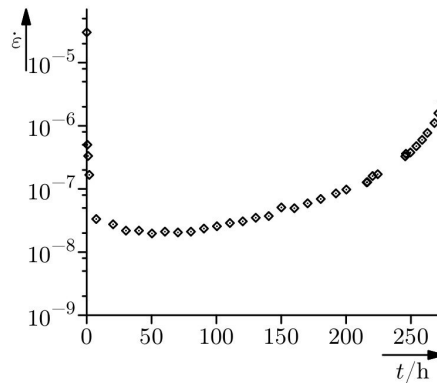


Figure 2.15: Experimental results for the creep rate versus time [22]

The strain rate decreasing experienced in the first creep stage (see Figure 2.12) occurs because changing in the dislocation substructure bring to harden the material.

After the first stage, for most of the materials in which the microstructure doesn't change during the creep process, thus for instance if no recrystallization is experienced, the *stage-2* is encountered. Here, if the test is performed at constant stress, the material's plastic deformation is increasing usually at constant strain rate. This is also called *steady-state creep* and in this part of the response, the strain rate is constant since the hardening and dynamic recovery are balanced [14].

Recovery This phenomenon consists in a thermal activated dislocation rearrangement. At high temperature self diffusion is facilitated and edge dislocations' climb brings to higher annihilation probability. Furthermore, the distribution rearrangement in a lower energy content configuration occurs.

The secondary creep doesn't exist for all the materials since for some of them, like nickel super-alloys, after the primary creep, the strain rate directly starts to increase (see Figure 2.15). Finally, the stage-3 or *tertiary creep* is the stage in which massive inner damage occurs in the material and failure of the component is encountered. Here, the strain rate starts to increase again and intercrystalline *creep fracture* grows at high speed.

2.2.2 Traditional Creep Laws

The creep phenomenon is explained by several *creep mechanisms*, which weight on the creep deformation depends on the stress and temperature. The main ones are listed below:

- Dislocation creep. Owing to the major vacancy density at the highest temperature, the dislocation *climb* is facilitated and the creep strain rate is described by [22]:

$$\dot{\epsilon} = \frac{A\sigma^3}{kT} D_V(T).$$

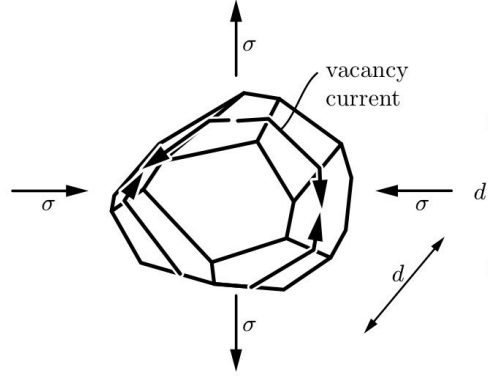


Figure 2.16: Vacancy diffusion on the grain boundaries [22]

Here, A is a material parameter, k is the Boltzmann constant and D_V is called *diffusion coefficient for volume diffusion*. Since this equation doesn't take into account the possible dislocation density variation (which is more frequent in the first and tertiary creep stages), it's more suitable for describing the material behaviour in the *second stage* [22].

- Diffusion creep. Mechanism which is dominant at the lower stresses and it consists in the vacancy diffusion to the grain boundaries less subjected to tensile stresses, without involving the dislocation sliding or climbing. This process is generally called *Coble creep* if the vacancies are moving on the grain boundaries (see Figure 2.16), and *Nabarro creep* if the vacancies are moving inside the grains.
- Grain boundary sliding. Phenomenon in which the grain boundaries can move against each other. For further discussions and informations see Reference [22].

From the practical point of view, the material behaviour in the secondary creep stage (also called *steady state creep*, SS) is usually studied and a relation between the creep strain rate and the other variables was found for different metals and alloys. In particular, this relation is called *power law creep* and it's described by the equation 2.9, where holds a power relation with the stress σ and an exponential one with respect to the temperature T [14]:

$$\dot{\epsilon}_{ss} = A_0 \exp[-Q_c/kT] (\sigma_{ss}/E)^n. \quad (2.9)$$

Here A_0 is a material constant, while k is the Boltzmann's constant and Q_c is the activation energy for creep. This relation is consistent with Norton's one and it's valid only when a constant steady-state stress σ_{ss} is applied [22]. Furthermore, this law is called *five power-law creep* being usually $n \approx 5$ and the mechanism which holds in this field is mainly the *dislocation climb* [14].

When the temperature decreases below roughly $0.5 \div 0.6 T_m$ the five power-law creep doesn't hold any more and the *power-law breakdown* (PLB) occurs. In such situation a different relation could be more suitable in the description of creep phenomenon, which is called *hyperbolic sine equation* [14]:

$$\dot{\epsilon}_{ss} = A_1 \exp[-Q_c/kT] [\sinh \alpha_1 (\sigma_{ss}/E)]^5. \quad (2.10)$$

Despite these relations were obtained in the most used tests for creep parameters definition, in the real situations the stress is almost never constant. For this reason, different creep laws were introduced.

2.2.3 Practical Creep Laws

In this subsection a brief description of the main laws of practical interest is introduced. Then, a more in-deep discussion about the equation implemented in Abaqus is faced. When the stress is varying during the test, the development of a creep theory is more difficult. In particular, two equations represent the most common situations:

- Time hardening. Hypothesis which holds when the creep strain rate is a function of the stress, *time* and temperature:

$$\dot{\varepsilon}_c = f(\sigma, t, T) \quad , \quad \dot{\varepsilon}_c = f_1(\sigma) \frac{df_2(t)}{dt} f_3(T).$$

Where each function can be found elsewhere and depends on the material and working conditions [21];

- Strain hardening. Law used when the creep strain rate depends also on the strain, owing to the material hardening:

$$\dot{\varepsilon}_c = g_1(\sigma)g_2(\varepsilon_c)g_3(T).$$

In particular, an example of the strain history prediction from this equation (where the functions have their own expressions) is plotted in Figure 2.17.

If these are the general theoretical expressions, the equation implemented in Abaqus for the *strain hardening* format is:

$$\dot{\varepsilon}_{eq,cr} = (A\sigma_{eq,d}^n [(m+1)\varepsilon_{eq,cr}]^m)^{1/(m+1)}. \quad (2.11)$$

This standard creep law provides a good fit of the experimental data when used for modelling the *secondary creep* [1]:

- $\dot{\varepsilon}_{eq,cr}$ is the uniaxial equivalent creep strain rate;
- $\varepsilon_{eq,cr}$ is the equivalent creep strain;
- $\sigma_{eq,d}$ is the Von Mises equivalent stress or *deviatoric* stress;
- A , m and n are materials constants. For physically reasonable behaviour A and n must be positive and $-1 < m \leq 0$.

Finally, in general the fatigue and creep phenomenon can occur together and in this more complex case a new theory called *creep-fatigue* is studied. The theory of practical use for this thesis is contained in this chapter, thus the work development is discussed in the following.

Chapter 3

Model Calibration

The specimen reported in Figure 3.1, which is an angular section of the water-blocking lead sheath of the submarine power cable, was tested in several axial fatigue tests. In this chapter, the model creation and material calibration on the base of the experimental data obtained with different strain rates is discussed, considering that the *lead alloy E* was used (see Table 1.1 for its chemical composition). The purpose of this work is the *material calibration*, useful for the next analysis which consists in the evaluation of the effect of macroscopic defects on the lead sheath fatigue life. Indeed, during production, transport and installation, the power cable is always subjected to fatigue cycles, which can lead to crack nucleation and breakdown.

Starting from a brief explanation of the acquired data, a deep discussion on the model construction and the parameters' assignment is debated. Thus, for instance, the interpolation of the experimental data, the plastic law and the creep model choice are faced. The entire modelling work was done on Abaqus, and Isight was used to optimize the creep parameters choice.

3.1 Experimental Data

Since in the real application, the power cable is subjected to fatigue cycles occurring with different amplitudes or strain rates, several tests at three different strain rates were performed. In Tables 3.1, 3.2 and 3.3, the experimental fatigue results coming from tests at different strain rates order of magnitude are reported, considering that the specimen is smooth, thus it has not pre-existing defects. In

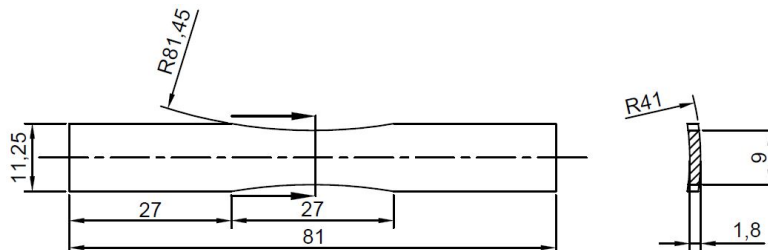


Figure 3.1: Dimensioned specimen drawing

particular, in each set of data the *nominal* strain rate imposed by the testing machine is constant and equal to $1e-2$, $1e-3$ and $1e-4$ ($1/s$). The collected data are called, respectively, Set 1, Set 2 and Set 3. In these tables, each row represents a different fatigue test and the acquired data are referring to the stabilised hysteresis loop of each of them, thus to the experimental data measured at half life.

Starting from the first column, the *engineering stress* of the stabilised hysteresis loop, expressed in *MPa*, is reported. After that, is the *real strain*, computed by means of DIC technique (see Appendix A.4) in the middle of the specimen from the convex side, having it a curvature commensurate with the real sheath's one.

Table 3.1: Experimental data for the smooth specimen, Set 1

s (MPa)	ε	$\dot{\varepsilon}$ (1/s)	N	R
4.8	4.30E-04	4.53E-03	1100000	0
6.45	4.65E-04	4.90E-03	486000	0
6.9	5.50E-04	4.32E-03	227838	0
7.45	8.75E-04	5.65E-03	104000	0
8.65	7.10E-04	4.58E-03	101000	0
7.9	7.80E-04	4.21E-03	110000	0
9.7	7.50E-04	4.05E-03	48500	0
8.7	1.10E-03	5.00E-03	62500	0
4.672	2.85E-04	8.14E-03	3570000	1
4.166	2.30E-04	6.57E-03	4200000	1
5.411	3.75E-04	6.75E-03	2207600	1
4.584	2.75E-04	4.24E-03	6297000	1
6.140	4.75E-04	5.00E-03	839000	1

Table 3.2: Experimental data for the smooth specimen, Set 2

s (MPa)	ε	$\dot{\varepsilon}$ (1/s)	N	R
5.15	3.90E-04	4.10E-04	231500	0
6.5	5.50E-04	5.79E-04	120000	0
7	7.50E-04	5.88E-04	63373	0
7.55	7.50E-04	4.83E-04	105000	0
7.1	1.20E-03	7.73E-04	55875	0
8.4	1.25E-03	6.75E-04	29000	0
8.1	9.25E-04	4.48E-04	29630	0
10.5	2.10E-03	9.58E-04	18500	0

Table 3.3: Experimental data for the smooth specimen, Set 3

s (MPa)	ε	$\dot{\varepsilon}$ (1/s)	N	R
1.1	1.80E-04	5.00E-05	43600	1
1.9	1.70E-04	5.00E-05	52460	1
2.5	2.1E-04	5.00E-05	46260	1
6	6.00E-04	5.00E-05	40000	0

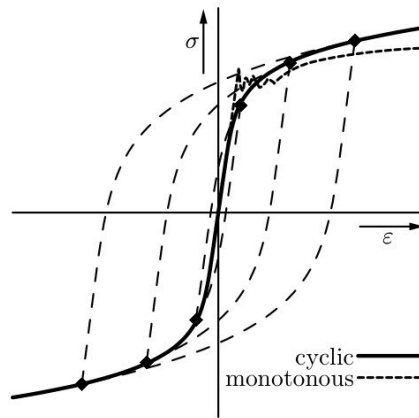


Figure 3.2: Example of cyclic stress-strain curve [22]

Being the strain measured on the specimen surface, this corresponds to the E22 component. In Figure 3.2, taken as an example, each dot through which the cyclic stress-strain curve is passing represents an experimental test. Differently from the stress, which is given as engineering quantity (being it computed by the load cell on the centre section), the *real* strain is provided. Indeed, since the lead has a wide plastic field, the displacement imposed from the testing machine wouldn't be representative of the deformation occurring on each point of the specimen. So, the strain was directly computed on the point of interest (the central one from the convex side, as discussed in the following), using DIC technique. Thus, the strain rate, the number of cycles in which the failure has occurred and the Run-out ($R = 1$ if the specimen has survived the test) are the last experimental data. Data in which $R = 1$ are usually the ones at lower applied stress. Indeed, the target of this work was to figure out the strain rate influence, which is not the main character at the lowest stress conditions (corresponding to the elastic field). For this reason, tests were interrupted being the duration in terms of number of cycles to failure N not relevant in those conditions. Again, the strain rate is different from the one imposed by the tensile testing machine, as it was computed in the point of interest by means of DIC. The *strain ratio* $R_\varepsilon = -1$ was adopted.

Finally, the Young modulus $E = 12000 \text{ MPa}$ and the Poisson's ratio $\nu = 0.431$ are known [12]. This values are valid for the static test and in the following section the Young modulus' will be changed in order to obtain a better description of the material behaviour in fatigue conditions.

An example of crack propagation in the smooth specimen is plotted in Figure 3.3, where is evident that the fracture nucleation and propagation took place in the middle section of the specimen.

3.2 Best Fitting Curves

The experimental data cannot be directly used on the software, being them generally too scattered. Thus, the average behaviour had to be found for each fatigue set of data. The best interpolation of experimental results was computed

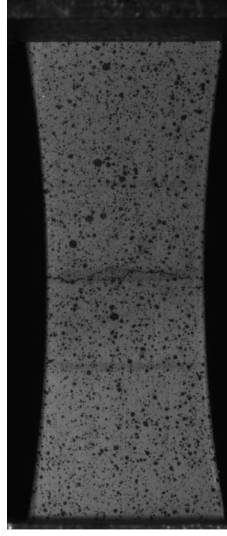


Figure 3.3: Fracture on a smooth specimen

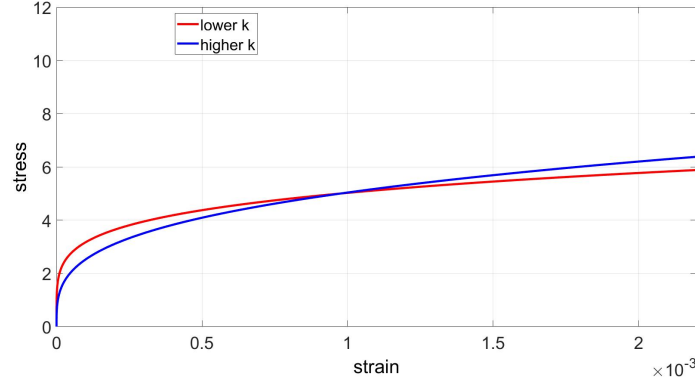
by means of the *Ramberg-Osgood* equation, as discussed in Section 2.1.2 and that curve was used as target in the Isight simulations, in order to find the creep parameters:

$$\varepsilon_{ro} = \frac{\sigma}{E} + \left(\frac{\sigma}{k'}\right)^{1/n'}. \quad (3.1)$$

Even if the real stress is requested both in Ramberg-Osgood law and in Abaqus, the engineering one was used: the difference between them, owing to the low strain amplitude applied during the fatigue tests, is negligible.

What is needed at this point is just a target, thus a mathematical expression which fits the experimental data. So, despite recurring values of k' and n' can usually be found in the literature for smooth specimens and for several metals [22], in this case no boundary conditions were imposed and the best fitting values (which have no physical meaning) were considered. Indeed, for each strain rate was found the best interpolation considering the Equation 2.2, where just the elastic and plastic strain are present, despite the creep component ε_{cr} has a wide influence on the specimen behaviour ($T_f \approx 327^\circ C$, thus lead is working in creep conditions even at room temperature). Thus, ε_{el} and ε_{pl} computed in Ramberg-Osgood equation have just a mathematical meaning and don't correspond to the real plastic and elastic strain components of the global deformation.

As first step for the identification of the best curve, two *first-attempt values* of k' and n' of the Equation 2.2 were chosen. Knowing also the Young modulus' and the engineering stress of each fatigue test (see Tables 3.1, 3.2 and 3.3), both elastic ($\varepsilon_{el} = \sigma/E$) and plastic strain component ($\varepsilon_{pl} = (\sigma/k')^{1/n'}$) were computed for every test and set of data. Then, the measured strain ε and the interpolated one ($\varepsilon_{ro} = \varepsilon_{el} + \varepsilon_{pl}$) were directly compared each other. Between them, the percentage and absolute error were computed in order to have two parameters by means of which understand how far the interpolation was from

Figure 3.4: k influence on best fitting curves, example

experimental data and so how well the data were described by the average curve:

$$err_{\%} = \left| \frac{\varepsilon - \varepsilon_{ro}}{\varepsilon} \right|, \quad err_{abs} = |\varepsilon - \varepsilon_{ro}|. \quad (3.2)$$

Thus, by an iterative procedure k' was manually adjusted while n' was computed by means of Excel Solver, trying to minimise the errors. The effect of the parameter k' (without considering the elastic contribution), after having optimised the value of n' , can be seen in Figure 3.4. In detail, lower values of k' allow to obtain a curve with an high slope at small strain values and more flat at higher ones.

In order to obtain a better interpolation, it was introduced a weight on the errors, which allowed to partially consider the influence of the most scattered test data. For instance, the point with $\sigma_{Set1} = 9.7 \text{ MPa}$ was rejected (owing to probable buckling effect) and the weigh of $\sigma_{Set1} = 8.65 \text{ MPa}$ considered in part, since they had a too big influence on the curve's shape, moving it far away from the most concentrated data. Even for lowest values of k' , the interpolation was far away from the experimental data, in particular for tests at smaller stress and strains. This consideration led to change the Young modulus' computed by other authors [12] for smooth specimen and the value $E = 15000 \text{ MPa}$ was adopted. This value was chosen as a mean value of the optimal ones for each set of data, in order to avoid the introduction of the Young modulus' dependence on the strain rate. Indeed, as it is possible to see in Figure 3.5 a lower value of E would have been more appropriate on the *Set 3* data, but less for the others.

Finally, the optimal values of k' and n' for each Set of data (thus the values for tests at different strain rates) are reported in Table 3.4, while the interpolation curve on the experimental data are plotted in Figure 3.5. These will be used as a target in the Isight simulations and they have been plotted singularly on Figures 3.6, 3.7 and 3.8.

As already said, data at lower stress (thus in the elastic part) are not important since in that region the three curves are overlaid. Finally, even if few data were collected at the nominal strain rate k' and n' were chosen in order to respect the slopes of the other curves. This curve was just used in the material calibration, but not in the irregularity effect evaluation where the simulations'

Table 3.4: Best fitting parameters and errors between curves and experimental data

Set	k'	n'	$err_{med,\%}$	$err_{med,abs}$	E (MPa)	ν
1	30	0.162	11.2%	6.00E-05	15000	0.431
2	20	0.122	21.8%	2.90E-04	15000	0.431
3	15	0.112	17.8%	4.00E-05	15000	0.431

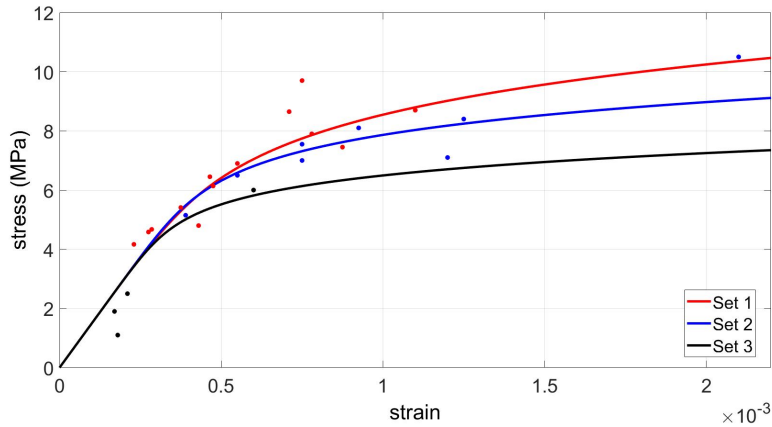


Figure 3.5: Best fitting curves of experimental data

curve were adopted. An improvement could be to perform more tests obtaining a more reliable interpolation.

3.3 Creation of the Abaqus Model

In this section, the model construction and properties assignment are discussed, while the creep parameters computation will be faced in the next section. The model imported by SolidWorks consists in a fourth of a specimen, which dimensions are reported in Figure 3.1, without the grabbing parts. This choice allowed to reduce the computational time, since the symmetry conditions are used to consider the global size as highlighted in Figure 3.9. Thus, three different models were created (one for each Set of data, being the strain rates different) and the lead alloy material properties were assigned to every model:

- Young modulus' $E = 15000$ MPa;
- Density $\rho = 11340E - 12$ ton/mm³, not necessary in this analysis;
- Power law creep parameters, in stress-hardening form as stress is time dependent, which computation is discussed in Section 3.4;
- Plastic curve with *isotropic hardening* (stress and material-property plastic strain ε_{mp}), reported in Table 3.6, which computation is discussed in the following. The choice of the isotropic hardening (instead of the kinematic one, that would have allowed to simulate the Bauschinger effect) was done

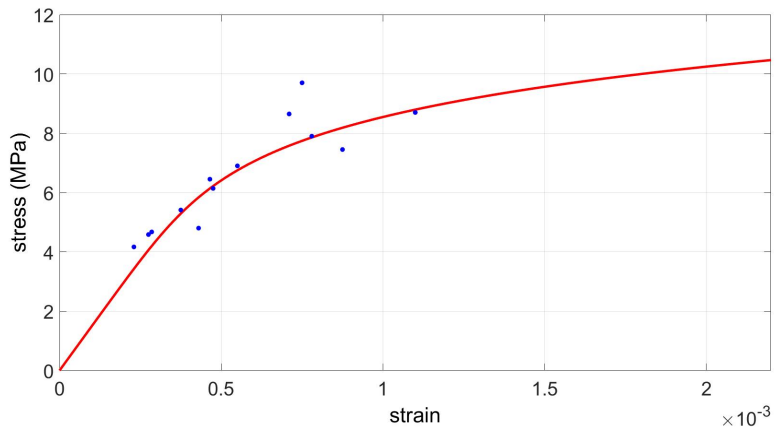


Figure 3.6: Best fitting curve of Set 1 data

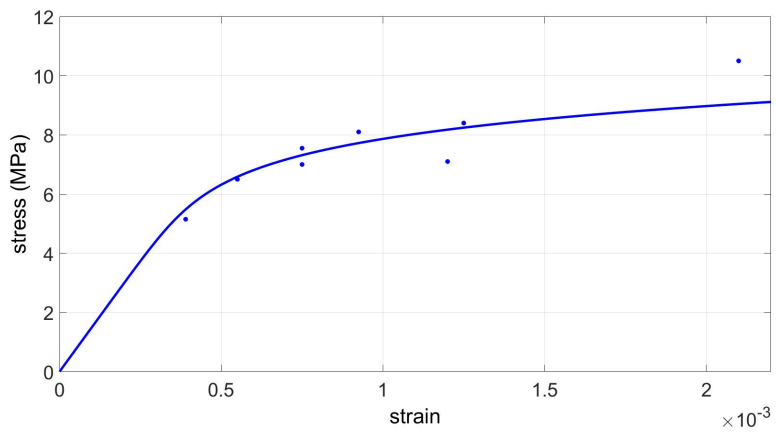


Figure 3.7: Best fitting curve of Set 2 data

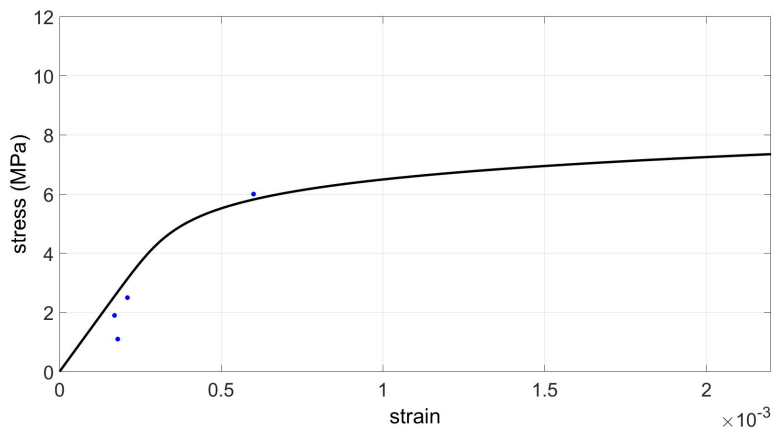


Figure 3.8: Best fitting curve of Set 3 data

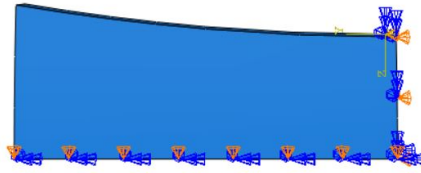


Figure 3.9: Symmetry conditions

in order to simplify the analysis, which doesn't plan to simulate an entire hysteresis cycle.

3.3.1 Plastic Curve Definition

The plastic curve must have the same shape of the best-fitting curves, but it must be shifted at higher stress levels in order to assume that it could have been achieved at a higher strain rate, so without the creep deformation influence (*true plastic curve*). Thus, few passages were followed:

1. Definition of the field in which the plastic curve is valid, which should contain all the experimental test deformations in order to avoid any mistake during the simulations. So, a limit strain value of $\varepsilon_{limit} = 0.01$ was arbitrary chosen, as enough higher than the strains involved in the fatigue tests (order of $\varepsilon = 0.002$, as shown in Tables 3.1, 3.2 and 3.3).
2. Computation of stress values at a deformation as near as possible to $\varepsilon_{limit} = 0.01$ for each set by means of the best-fitting curves, which results are reported in Table 3.5. This allowed to understand how high the plastic

Table 3.5: Best fitting, limit points

Set	ε	σ_{limit} (MPa)
1	0.0099	14
2	0.011	11.5
3	0.011	9

curve should have been, and so to choose the *target stress* σ_p for the plastic curve at the same deformation ε_{limit} . In order to assume that this can be considered as a *true plastic curve*, the chosen stress σ_p must be higher than the highest σ_{limit} . In this way, the additional deformation between the plastic curve and experimental ones can be associated to the creep phenomenon. In Figure 3.10, best fittings compared to plastic curve are plotted.

Few Isight iterations were done in σ_p choice. Finally, the optimal value was defined as $\sigma_p = 14.5$ MPa, which means that the plastic curve passes from the point $P=(0.01,14.5)$, as shown in Figure 3.10. Indeed, despite the plastic curve is close to Set 1 best-fitting, higher values of σ_p would have led to need more creep contribution and in those conditions Isight *Data Matching* wasn't able to find creep parameters allowing to fit the target (best fitting curves) with an error less than the 10%.

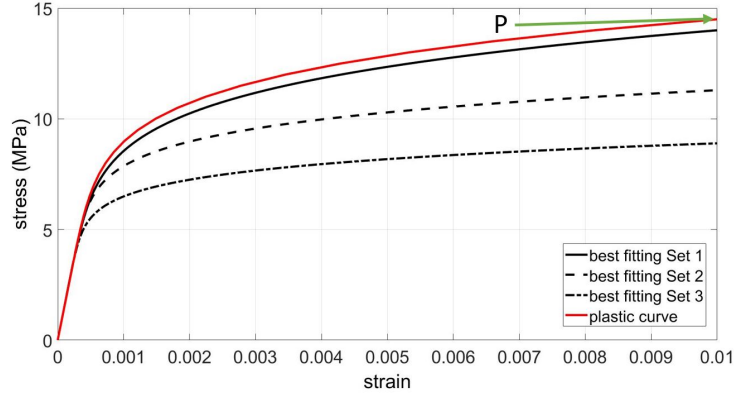


Figure 3.10: Plastic curve compared with best fittings

- Once the target point P was defined, the proper plastic curve's shape had to be found. As well as for the best-fitting curves, also the plastic one is described by the Ramberg-Osgood law, for which k' and n' are unknown. k' was defined first, while n' was the free parameter that, using Excel Solver, allowed the plastic curve to pass from the point $P=(0.01,14.5)$. In particular, the choice of k' was made in order to obtain an enough *low yield point*, so that also Set 3 curve could feel the plastic deformation influence. Indeed, after few Isight iterations it was highlighted that the only creep contribution was not enough to reach the total deformation without a certain plastic contribution. Abaqus material property must be the only plastic component, thus the definition of the yield point allows to divide the global strain and to reject the elastic component.

Yield Point Definition

Since the strain amplitude is small and even less than the deformation for which $R_{p0.2}$ is defined, a deviation from the elastic behaviour was defined in a different way. The yield stress σ_y was computed on the plastic curve as the point in which the plastic deformation was equal to 1% of the elastic contribution, so that this plastic term could be negligible. Thus, by choosing the value for k' , by means of Excel Solver σ_y was computed from the following equation.

$$0.01\sigma_y/E = (\sigma_y/k')^{1/n'} \quad (3.3)$$

Finally, the values $k' = 30$, $n' = 0.154$ and $\sigma_y = 4.2 \text{ MPa}$ were found. In Figure 3.11, few iterations in the choice of σ_p and k' are plotted, where the red one was implemented in Abaqus.

So, considering the Yield Point as the threshold between the elastic and the plastic field, to that a *null plastic strain* was assigned. This means that the plastic properties assigned to the model were found by subtracting the term $(\sigma_y/k')^{1/n'}$ to the true strain for $\sigma > \sigma_y$ in the following way:

$$\varepsilon = \varepsilon_{pl} - (\sigma_y/k')^{1/n'} = (\sigma/k')^{1/n'} - (\sigma_y/k')^{1/n'}$$

This consists in placing a new x-axis with its origin in the so defined yield point, and from that point to higher stresses, the plastic deformation was measured.

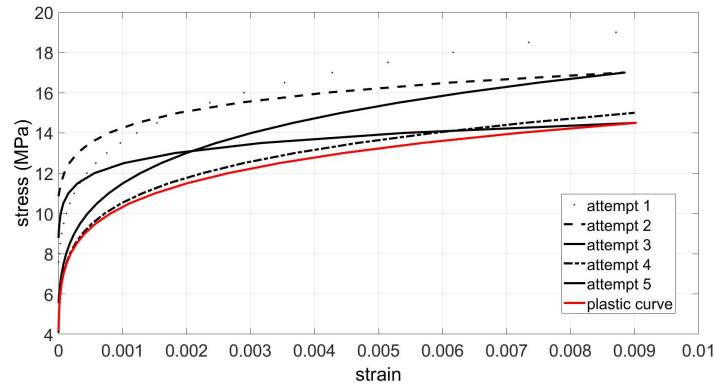


Figure 3.11: Iterations on plastic curve choice

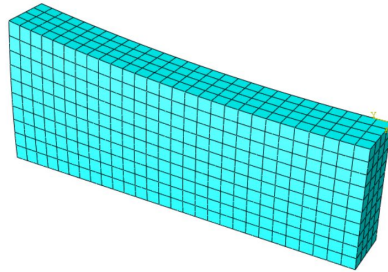


Figure 3.12: Result of mesh creation

The plastic curve is reported in Table 3.6, where to the last deformation a value of 1 is given, in order to avoid errors during the simulations.

3.3.2 Mesh Creation, Loading Step and Outputs

Once the material properties were defined, the mesh on the model with *quadratic brick elements* (in order to avoid the description of constant deformation field on each) was created.

After few iterations, the maximum size of 0.5 mm was defined. This mesh, shown in Figure 3.12, is considered enough detailed being the stress field uniform, since there are not important notch effects, and the centre point (where measurements were done) is well described by a single element. Also an higher size could have been chosen in order to obtain the same results, but this was selected in order to have a more detailed solution and a reasonable computational time.

Finally, the correct implementation of the loading step and reading of the outputs on the element of interest were faced.

Loading Step

After having defined the boundary conditions on symmetrical faces (Figure 3.9), a displacement field was applied to the upper face along y positive direction. Since the creep phenomenon is involved in the analysis (time dependent stress distribution), *visco* load type was selected [1]. Furthermore, to the

Table 3.6: Lead plastic curve

σ	ε_{mp}
4.2	0.00
4.5	1.87E-06
5	6.40E-06
5.5	1.42E-05
6	2.71E-05
6.5	4.73E-05
7	7.82E-05
7.5	1.24E-04
8	1.89E-04
8.5	2.82E-04
9	4.09E-04
9.5	5.82E-04
10	8.12E-04
10.5	1.11E-03
11	1.51E-03
11.5	2.01E-03
12	2.65E-03
12.5	3.45E-03
13	4.45E-03
13.5	5.68E-03
14	7.19E-03
14.5	9.03E-03
15	1.12E-02
15.5	1

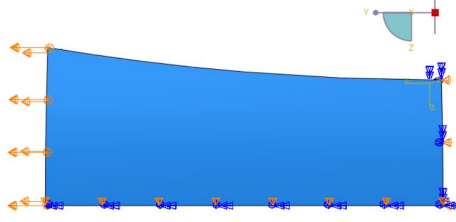


Figure 3.13: Boundary conditions

same surface was applied a constraint on displacements along x direction which emulates the grabbing machine element, as reported in Figure 3.13.

In order to guarantee that the correct strain rate is respected during the simulations, *ramp* load shape was defined. This condition doesn't really respect the testing situation, since at each peak the material faces a strain rate inversion. Thus, the load shape should have been modelled with a null derivative at the end. However, the *ramp shape* is simpler and it allows to obtain reliable results. Then, the *increment size* was chosen in order to have between 50 and 100 iterations, while the *creep strain error tolerance* was set equal to $1E-05$. The displacement is then applied with a constant speed from the time $t = 0$ until the end. Thus, the cycle duration and the applied displacement value had to be computed:

$$t = \varepsilon / \dot{\varepsilon}_m. \quad (3.4)$$

Where:

- t is the duration of a quarter of the fatigue cycle, thus a simulation which covers the best fitting curves;
- $\varepsilon = 0.002$, is considered as the limit value for each cyclic stress-strain curve, since the available experimental data are within this interval;
- $\dot{\varepsilon}_m$ is, for each set of data, the *average strain rate* of the measured ones in Tables 3.1, 3.2 and 3.3.

In Table 3.7 the average strain rate for each set of data and the consequent duration of a quarter cycle, computed by Equation 3.4, are collected. After few

Table 3.7: Average strain rate and duration for each simulation

Set	$\dot{\varepsilon}_m$ (1/s)	t (s)
1	5.23E-03	0.38
2	6.14E-04	3.26
3	5.00E-05	40

iterations modifying the applied displacement, the value causing the deformation $\varepsilon = 0.002$ on specimen centre, which is the point where strain and strain rate were measured, was found equal to $displ = 0.023$ mm.

Outputs

Since the stress and strain for each test were measured by DIC technique on the specimen centre, the desired outputs are stress S_{22} and deformation E_{22} components on the element 1120, indicated by an arrow in Figure 3.14. 22 corresponds to y direction, thus the vertical one.

Since the mesh is made by quadratic elements, 8 integration points from which extract the output on each element are available. Despite of that, being the stress field uniform, the results on each integration node on the element of interest have a negligible difference and *point 1* was chosen. Finally, $E_{22} - S_{22}$ history during the analysis was compared with the best-fitting curves.

In order to verify that the solution of the simulations was independent from the *increment size* chosen in order to have a number of iterations between 50 and 100, few attempts were done forcing Abaqus to perform simulations with a constant increment size. In all the three models, four simulations were submitted considering a number of iterations between 32 (avoiding instabilities for a lower number, which would have led to the simulation abortion) and 400. Considering the same outputs on the element were measurements are performed, the results were compared each other and the solution was found to be *independent* from the increment size, at least until the third decimal digit for the stress values.

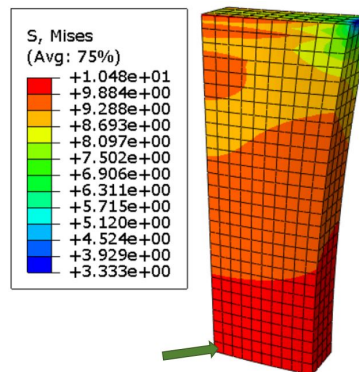


Figure 3.14: Von Mises distribution and element from which output are extracted

3.4 Isight Optimization and Creep Parameters

The *calibration optimization* was performed by the minimization of few objectives. In particular, the controlled entities allowed to reduce the difference between the areas of the simulation and the target curves, together with the reduction of the squared difference between values at constant strain. Even if two targets should have been enough for each simulation, a third one was added owing to the simulation's error. Indeed the control in terms of difference between areas was done considering the initial position of the simulation curve (thus computed with the attempt values A , m and n) with respect to the best-fitting, but during few attempts a combination of creep parameters could have led to change the position of the simulation with respect to the target. Thus, both area's objectives *under target* and *above target* were chosen in order to consider that during few

loops the position of the simulation curve could have changed with respect to the best-fitting. This choice consists in the research of a convergence to the target both from the top and the bottom with respect to the best fitting curves.

After several iterations, the optimal power law creep parameters were found:

- $A = 3.94e - 08$
- $n = 4.218$
- $m = -0.6103$

With these parameters, the simulation run in Abaqus for each model (thus for the three models) was compared with best-fitting curves until the deformation $\varepsilon = 0.002$ in order to guarantee the correct strain rate, and the results plotted in Figures 3.17, 3.18 and 3.19 were obtained. These creep parameters were considered valid since the maximum error between the simulation and target curve (computed at constant strain amplitude) is around 8% for the terminal strains of Set 3 and for the middle ones of Set 2, while the other simulation shows a better correspondence with respect to Set 1 data. Furthermore, in Figure 3.16 the simulations compared to scattered data for each set were plotted and an example of wrong interpolation is reported in Appendix A.1.

Even if the best-fitting cyclic stress-strain curves are a little different from the curves covered by each simulation, all the following studies were performed by means of the simulations and so supposing that the material have had a behaviour described by the optimized curves. This means that the role played by the best fitting curves is hidden behind the optimization and each experimental data is read through the simulated curves. For this reason, *corrected* Ramberg-Osgood parameters were found. These have no physical meaning, but they are just describing the simulation curves. Indeed, performing interpolations of simulations' results by means of best fitting curves instead of optimized curves would have led to errors, in particular in the next chapter for the interpolation of fatigue curves.

$$\varepsilon_{ro} = \frac{\sigma}{E} + \left(\frac{\sigma}{k'_{new}}\right)^{1/n'_{new}}$$

Table 3.8: Ramberg-Osgood parameters describing the simulation curves

	Set 1	Set 2	Set 3
k'_{new}	30	25	20
n'_{new}	0.166	0.156	0.15

3.5 Data and Results Resume

In this section a brief resume of the procedure and results for the model calibration is discussed:

- Model geometries are plotted in Figure 3.1;
- The curves used as *target* in Isight simulations in order to compute the optimal creep parameters are described by the average behaviour of the

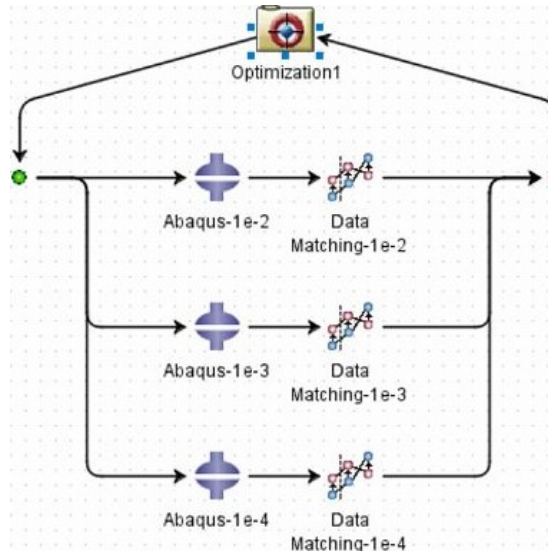


Figure 3.15: Isight program

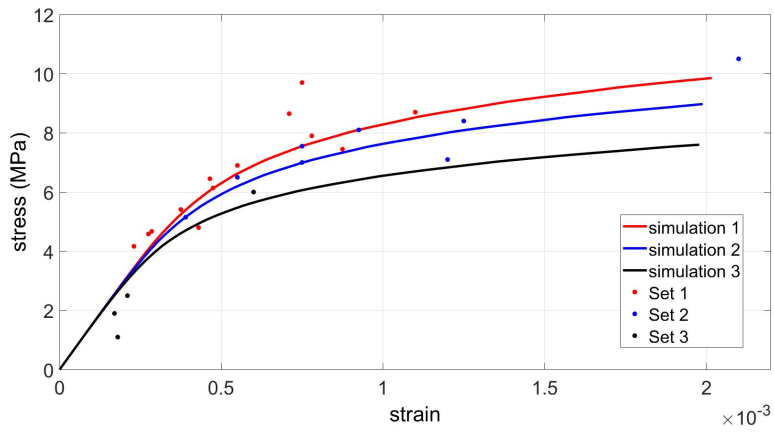


Figure 3.16: Comparison between simulations and scattered data

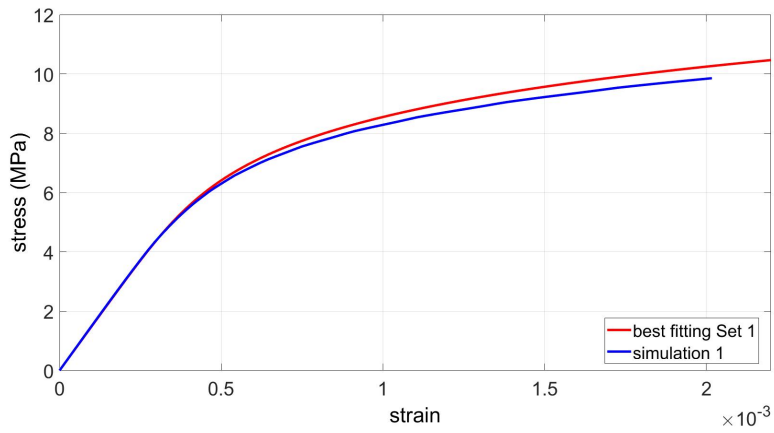


Figure 3.17: Comparison between Best fitting 1 and Simulation 1

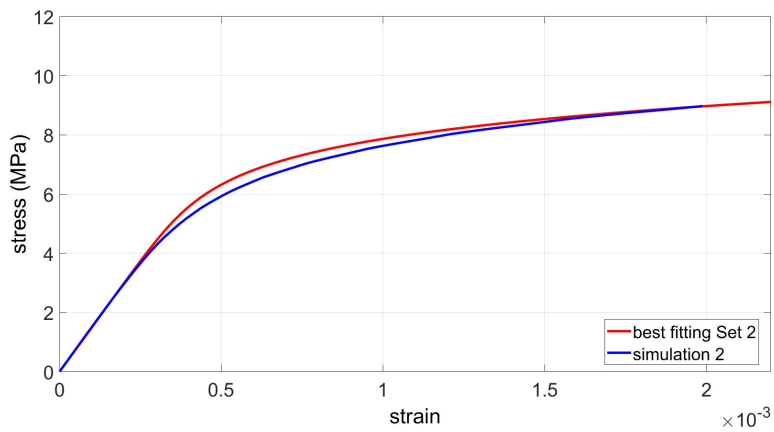


Figure 3.18: Comparison between Best fitting 2 and Simulation 2

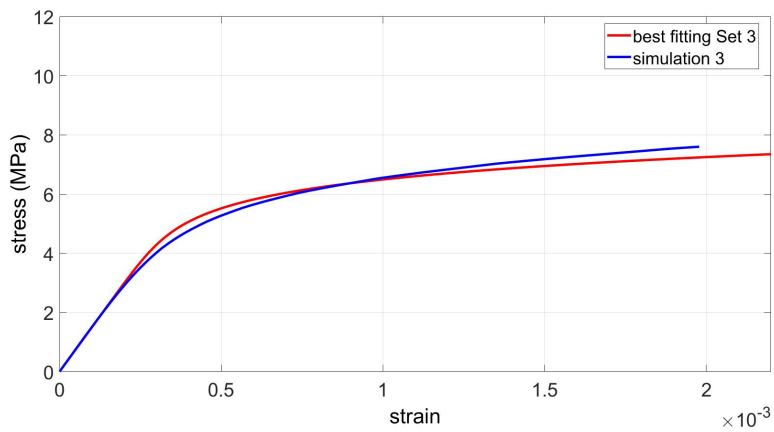


Figure 3.19: Comparison between Best fitting 3 and Simulation 3

experimental tests (collected in Tables 3.1, 3.2 and 3.3). In particular, in Table 3.4 the best fitting parameters describing these curves (plotted in Figure 3.5) are collected;

- From the three time-dependent curves plotted in Figure 3.5, a *time-independent* one was found. This, plotted in Figure 3.10, corresponds to an ideal *pure plastic response*, which Ramberg-Osgood parameters are $k' = 30$, $n' = 0.154$ and with yield stress $\sigma_y = 4.2 \text{ MPa}$. Thus, the plastic strain component was extracted and the consequent plastic curve reported in Table 3.6 was assigned to the model as a plastic property;
- The average strain rate was computed from the experimental data for each strain rate condition and the duration of each simulation was then computed (see Table 3.7);
- Finally the creep parameters were computed: $A = 3.94e-08$, $n = 4.218$ and $m = -0.6103$. The simulation curves (which outputs are concerning the integration point 1 of the central element from the convex side, as plotted in Figure 3.14) are described by *modified Ramberg-Osgood parameters*, collected in Table 3.8.

Once the model was calibrated, the same material properties were used in order to simulate the response of the specimens with irregularity, which is the topic of the next chapter.

Chapter 4

Specimens with Irregularity

The main purpose of this and Chapter 3 was to understand and study the influence of irregularities on the lead sheath fatigue life. These irregularities, as shown in Figure 4.1, are a consequence on the above polymer tape winding (see Figure 1.2) which, owing to the high pressure used in his collocation, brings to wrinkle the underlying lead sheath. Thus, after the studies on smooth specimens



Figure 4.1: Specimens with irregularities

useful for the material calibration (see Section 3.5), its properties were used to develop further models and to study the irregularities effect on the lead layer. In particular, the experimental evidence is that these are reducing the lead sheath life and the main objective of this work was to compute the *fatigue intensity factor*, further than the *notch sensitivity*. These are the two entities which allow to figure out the relationship between the stress-strain concentrations and the number of cycles to failure N , at different strain rates, further than allowing the life loss estimation in the real power cable configuration.

Thus, the procedure followed is resumed in the following sections:

1. Geometrical properties. Discussion on the geometrical data collected;
2. Models creation. Irregularity geometrical modelling, model and material properties, further than correct strain rate assignment;

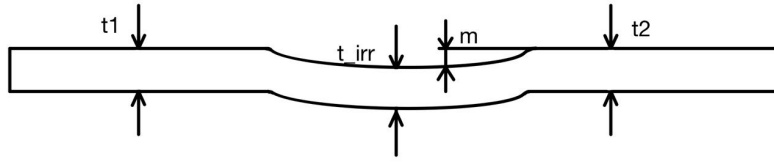


Figure 4.2: Irregular specimens geometries

3. Fatigue intensity factor k_f . Global strain amplitude ε_g computation from the time frames identification and fatigue curves $\varepsilon_g - N$ interpolation by means of Coffin-Manson-Basquin (CMB) equation;
4. Strain intensity factor k_t and k_ε . Identification of the most solicited point for smooth and irregular specimen and computation of the intensity factor in the elastic and plastic field;
5. Notch sensitivity q computation for all the strain rate conditions and results discussion.

4.1 Geometrical Properties

For each fatigue test, a specimen was directly obtained by the real lead sheath in correspondence with the irregularity caused by the above polymer tape, where the *nominal thickness* of the sheath studied in this chapter is 1.8 mm . In each specimen (which geometry is sketched in Figure 4.2), irregularities' geometry is different and, even if the fatigue results should be compared between data coming from the same irregularity (in order to avoid the influence of the geometrical parameter), the high dispersion of geometrical data led to consider each result as coming from a *mean geometry*. These specimens had been left for two days at room temperature, before testing. For this reason it could be said that all the residual stresses on the irregularity were relaxed, while the local hardening could had been mitigated by recovery and recrystallization. Therefore, the same material properties (and in particular the same plastic curve) were used in all the model, irregularity included.

In order to compare the experimental results between the smooth and irregular specimens (thus, to compute k_f and q), several fatigue experimental tests were performed at two nominal strain rates: $1e - 2$ and the slowest $1e - 3$ (1/s). These, as discussed in Section 3.1 don't correspond to the *real* strain rate locally perceived by the material. As well as it was done for the smooth specimen, *Set 1* is used to indicate the acquired data at the nominal strain rate $1e - 2$, while *Set 2* is used for the other results, collected from a nominal input strain rate of $1e - 3$. No experimental tests were performed at the nominal strain rate of $1e - 4$.

In Table 4.1 are collected the geometrical dimensions of all the specimens, referring to Figure 4.2. Each one is identified by the *ID code*; thus the maximum grabs thickness was measured, together with the irregularity thickness and the parameter m , which is the offset between the sheath convex part and the irregularity lower surface. Finally, the difference between left and right grabs

Table 4.1: Irregular specimens' geometries (mm)

ID	$t_{1,max}$	$t_{2,max}$	t_{irreg}	m	$t_{max} - t_{min}$
1a	2.00	1.97	2.05	0.15	0.03
1b	1.93	1.93	1.93	0.16	0
1c	2.03	2.01	2.01	0.24	0.02
2a	1.87	1.85	1.88	0.19	0.02
2b	1.95	1.96	1.92	0.24	-0.01
2c	1.88	1.89	1.89	0.21	-0.01
3a	1.81	1.88	1.80	0.20	-0.07
3b	1.86	1.84	1.81	0.19	0.02
3c	2.01	2.05	2.03	0.13	-0.04
3d	2.05	2.03	2.01	0.16	0.02
4a	1.83	1.85	1.90	0.20	-0.02
4b	1.84	1.81	1.86	0.15	0.03
4c	1.85	1.91	1.91	0.13	-0.06
5a	2.05	2.08	2.05	0.23	-0.03
5b	2.02	2.01	2.01	0.12	0.01
5c	2.14	2.15	2.21	0.09	-0.01
mean values	1.95	1.95	1.95	0.17	

thickness was computed, while the test conditions in terms of strain rate and global strain amplitude - stress amplitude will be specified forward.

On the base of these geometrical properties, a new model was created for each nominal strain rate.

4.2 Models creation

In this section the geometrical modelling, the model properties assignment and the calibration verification are faced, further than a discussion on the fatigue experimental data. This was useful in order to obtain a model from which reliable results could be computed.

4.2.1 Geometrical Modelling

Once the geometrical properties were known, a new model was created for each nominal strain rate, in order to have the irregularity in its restricted section. Thus, referring to Figure 4.2, the following geometrical properties were defined:

- Thickness value t , constant along all the model;
- Offset m value.

Firstly, owing to the high dispersion of t and m data, the mean value for each significant entity was computed. Thus, from Table 4.1, the three average thickness, further then the average of $m = 0.17 mm$, are known.

The mean thickness of $1.95 mm$ is different from the nominal one of $t = 1.8 mm$. Since no geometrical data were available, the nominal value was used for the material calibration in the smooth specimen models. Thus, in order to

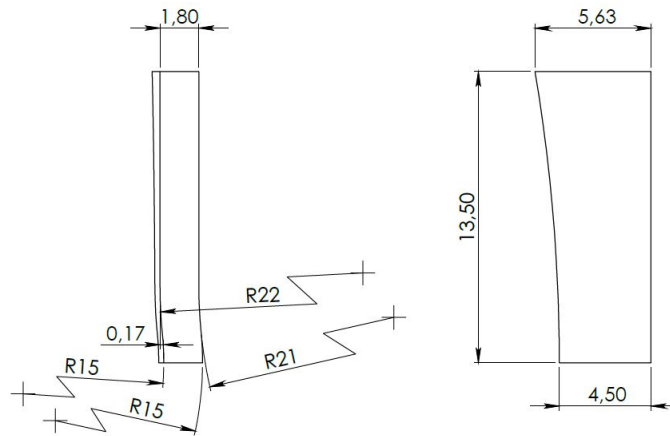


Figure 4.3: Dimensioned irregular specimen drawing, modelled on SolidWorks

compare the results between the irregular models simulations and the smooth ones (analysed in Chapter 3) the same thickness had to be used and the constant nominal value of 1.8 mm was assigned also in this case.

The model used in order to study the irregularity influence is plotted in Figure 4.3, which represents a fourth of the specimen. Further than $t = 1.8 \text{ mm}$ and $m = 0.17 \text{ mm}$, also the four radius defining the irregularity severity (2 for the convex side and 2 for the concave one) were chosen as representative of a mean-high irregularity severity. This means that the irregularity was modelled considering that it was more concentrated near the mean section, thus the four radius had to be small enough to allow a rapid changing of the section direction.

Radius of Irregularity

The value for each of the four radius was obtained by means of a Matlab file, reported and discussed in Appendix A.2. Its purpose was to define the four radius values in order to obtain a shape with *tangent curvatures*, avoiding arising edges which could have led to unreal local intensification factors during the simulations. This choice (which represents an approximation) was critically discussed in the Chapter 6.

The irregularities longitudinal dimensions were extracted form Figure 4.1, owing to the impossibility of accessing to the laboratory for coronavirus pandemic. For values of $start = 10 \text{ mm}$ and $irr = 3 \text{ mm}$ (explained in Appendix A.2), the following radius were computed, while approximations had been implemented:

- $R_{1,int} = 13.7 \approx 15 \text{ mm}$;
- $R_{1,ext} = 15.5 \approx 15 \text{ mm}$;
- $R_{2,int} = 22.4 \approx 22 \text{ mm}$;
- $R_{2,ext} = 20.6 \approx 21 \text{ mm}$.

Ext refers to the convex side of the specimen, while *int* to the concave one. The model created was exported in IGES format and opened in Abaqus, where the model properties were assigned.

4.2.2 Model Properties

Since the purpose of this analysis is to highlight the irregularity effect on the fatigue life of the lead sheath, experimental tests were performed in order to allow a comparison with smooth specimen fatigue tests. Thus, the *experimental data* are introduced.

In the case of the smooth specimen, the model fitting and calibration was done verifying that the longitudinal deformation on the restricted section from the convex side, in the element pointed in Figure 3.14 was corresponding to the experimental measured values. Regarding to the irregular model, using DIC technique on the same region of the smooth specimen led to data affected by uncertainty (owing to the presence of the irregularity). Thus, Digital Image Correlation was used on a different region, identified with the three longest *green segments* which extremities are highlighted in Figure 4.4. To the average of them, the deformation data in Tables 4.2 and 4.3 are referred. These tables are

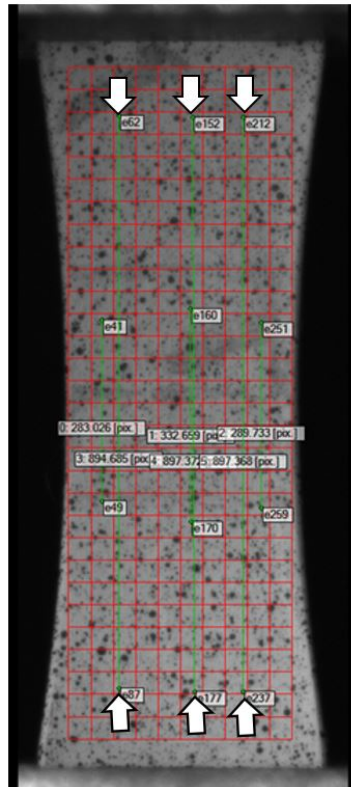


Figure 4.4: DIC on irregular specimen. Computations on three short segments were affected by uncertainty, thus the longest had been used.

distinguished in relation to the strain rate and, as it was done for the smooth specimen for Tables 3.1, 3.2 and 3.3, the main data are discussed.

The *ID* code allows to link the available fatigue results with the previous geometries measurements (the fatigue data are not available for each specimen). Then, being the simulation performed on a fourth of the entire hysteresis loop, the stress-strain data are indicated in terms of *amplitude*, even if they were collected

Table 4.2: Experimental data of irregular specimen, Set 1

ID	$Global\varepsilon$	$\varepsilon_{DIC,in}$	$\varepsilon_{DIC,rel}$	N	σ_{in}	σ_{rel}
1a	0.06	0.064	0.0675	97181	8.125	8.07
1b	0.065	0.0665	0.069	98359	8.45	8.25
2a	0.05	0.048	0.0515	130051	7.925	7.925
3c	0.10	0.105	0.1025	37129	10.1	10.05
4b	0.09	0.0975	0.0875	23829	10.45	10.15
4c	0.09	0.095	0.110	48421	10.6	10.35

Table 4.3: Experimental data of irregular specimen, Set 2

ID	$Global\varepsilon$	$\varepsilon_{DIC,in}$	$\varepsilon_{DIC,rel}$	N	σ_{in}	σ_{rel}
2b	0.065	0.06	0.062	50114	8.35	8.075
2c	0.05	0.04	0.0425	265882	6.175	6.15
3a	0.09	0.0925	0.096	26595	9.1	8.99
3b	0.08	0.081	0.07	33516	9.05	8.85
3d	0.06	0.055	0.0565	63854	7.925	7.75
5b	0.075	0.072	0.0785	32885	8.75	8.075

expressed in *range*. The global strain amplitude $Global\varepsilon$ imposed by the testing machine at each cycle (expressed in %) is indicated. This is different from the DIC measured strains, reported in the following columns and expressed in %, and is different from the following global strain ε_g . In particular, $\varepsilon_{DIC,in}$ refers to the strain amplitude measured during the first few cycles of the fatigue test, while $\varepsilon_{DIC,rel}$ is the *relaxed* strain amplitude, which was used in the following as representative of each stabilised hysteresis loop. Finally, the number of cycles N to failure, the *initial* stress amplitude and the *relaxed* stress amplitude, both expressed in MPa , are reported. These stresses were computed by the load cell on the reduced section, thus they are *nominal* engineering values.

Since the simulations are reliable if they fit the calibration state, few conditions had to be respected in the properties assignment to the model:

- *Material properties* are the same obtained after the material calibration in Chapter 3, and resumed in Section 3.5;
- The *duration* of both the simulations was maintained constant (see Table 3.7). $t = 0.38 s$ was assigned to the model concerning to data Set 1, while $t = 3.26 s$ to data Set 2 (see Tables 4.2 and 4.3);
- Finally, since the exact value of the strain rate for each test was not experimentally computed, the same average values obtained for the smooth specimens were used. In order to respect the average strain rate $\dot{\varepsilon}_m$, reported in Table 3.7, the suitable displacement on the grabbing part had to be verified. Indeed, owing to the presence of the irregularity, the displacement which allows to simulate the same strain rate could have been changed.

In Table 4.4 these conditions are resumed.

Table 4.4: Average strain rate and duration for each simulation for the irregular specimens

Set	$\dot{\epsilon}_m$ (1/s)	t (s)
1	5.23E-03	0.38
2	6.14E-04	3.26

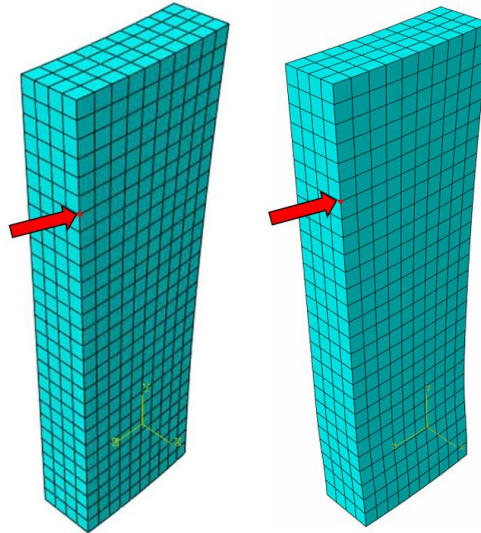


Figure 4.5: Selected points for displacement comparison. On the left smooth specimen, on the right irregular specimen

Displacement Verification

The results of the irregular specimen simulations can be compared with the smooth ones just if the models respect the applied strain rate (nominal value $1e-2$ and $1e-3$ (1/s)), thus if the global displacement and the simulation duration are identical.

The *global size* of the mesh elements was left equal to the smooth specimen one (0.5 mm). This choice was done in order to have the same number of elements and the same spatial point from which outputs were extracted. Thus, being the deformation in the specimen with irregularity measured at a point near to the grabbing part, as explained in Figure 4.4, from simulations of both irregular and smooth specimen, the displacement of the same point (see Figure 4.5) was extracted as output. This, as the one where measurements on the irregular specimens come from, has a longitudinal coordinate of $\frac{l_0}{2} \approx 10.5\text{ mm}$ with respect to the restricted section. Also this dimension was directly computed from the Figure 4.4, where the length of the longest green segments was found $l_0 \approx 21.0\text{ mm}$. The identified point will be considered as the point to which the *global entities* are assigned, since it is close to the grabbing part, but still on the specimen. For this reason it is exempt from data that would have been measured by the testing machine.

Having as target the displacement of the pointed node of the smooth specimen

(which results are reliable as the model was calibrated) the proper displacement was applied to the irregular model, with a boundary condition already shown in Figure 3.13. Applying a load amplitude with the *ramp* shape, which allows to obtain a constant strain rate along all the simulation, the displacement boundary condition to the irregular specimen was found equal to 0.023 mm both for *Set 1* and *Set 2* models. This is the same value applied in the smooth specimen model and it was chosen in order that all the experimental data, and so all the test conditions, were included in the simulation with an acceptable deformation margin.

Thus, after having assigned all the necessary properties to the model, the computation of the *fatigue intensity factor* could be performed.

4.3 Fatigue Intensity Factor

From the definition given in Section 2.1.3, in order to compute the fatigue intensity factor, $\varepsilon_g - N$ *fatigue plots* are necessary. Indeed, the experimental stress values, owing to the distinct plastic behaviour which characterises lead, are not suitable for the most common $\sigma_n - N$ fatigue plots. In these, the smooth and irregular experimental results wouldn't be sufficiently different each other.

Since the purpose of this work was to study the irregularity influence in all the global strain ε_g domain, the following steps were faced:

- Identification of ε_g values concerning to the experimental conditions for both the smooth and irregular models:
 - Recognition of the simulation time frames corresponding to the experimental tests;
 - Output selection and ε_g computation;
 - Scattered plots $\varepsilon_g - N$ with experimental results.
- $\varepsilon_g - N$ scattered plots interpolation with CMB equation:
 - Interpolation parameters.
- k_f computation from the $\varepsilon_g - N$ interpolation curves.

First of all, the point shown in Figure 4.5, which is close to the grabbing part, was selected as reference point for the *global strain* computation. This was chosen since it well represents *global* conditions, avoiding the influence of the inaccurate measurements performed by the testing machine. Then, its displacement was selected as output in the Abaqus simulations for every time frame and in this way the *global strain* along all the simulation could be computed:

$$\varepsilon_g = \ln\left(1 + \frac{2d}{l_0}\right).$$

Where $l_0 = 21.0 \text{ mm}$ is the average length of the longest segments in Figure 4.4, at the tip of which the output displacement was selected.

Since the number of cycles to failure N (useful for $\varepsilon_g - N$ plots) is known only for the experimental conditions, from the simulation the time frames which are able to represent the experimental tests must be selected. These are the

Table 4.5: Time frame identification for the smooth specimens, Set 1

time (s)	time frame	$E22_{DIC}$	$E22_{sim}$
0.094	22	4.30E-04	4.38E-04
0.099	23	4.65E-04	4.63E-04
0.114	26	5.50E-04	5.39E-04
0.179	39	8.75E-04	8.83E-04
0.149	33	7.10E-04	7.22E-04
0.159	35	7.80E-04	7.77E-04
0.154	34	7.50E-04	
0.219	47	1.10E-03	1.10E-03
0.064	16	2.85E-04	2.94E-04
0.049	13	2.30E-04	
0.079	19	3.75E-04	3.65E-04
0.059	15	2.75E-04	2.70E-04
0.104	24	4.75E-04	4.88E-04

time frames which are describing the experimental conditions and from which the ε_g can be associated with the experimental N . For this reason, the proper time frames had to be identified.

4.3.1 Time Frames Identification

As already discussed for the smooth specimen in Chapter 3, the simulation is generally solved in a number of time frames between 50 and 100. Step by step, a new point on the *cyclic stress-strain curve* is covered and for each of them all the requested outputs are computed. For this reason, comparing the results with every experimental data, each of them can be described by a point on the simulation curve, so by a certain time frame. Their correct identification is determinant to be representative of that experimental data.

The proper time frames on the *stabilised cyclic curve* for the smooth and irregular specimen were found in two different ways.

Smooth Specimen

In the case of the smooth specimen, the experimental data collected by DIC technique were referred to the strain measured in the central part of the specimen from the convex side (see Figure 3.14). Thus, this is the same point from which the simulation results were considered. Being DIC measurements performed on the specimen surface, the experimental results are referring to $E22$ strain component, which was extracted as output in the simulation from one arbitrary node of the same element at every time frame. The integration node 1 was used and this choice is arbitrary since in these simulations the stress and strain field is uniform. Then, $E22$ value was compared to the experimental strain amplitude values, collected in Tables 3.1 and 3.2. Choosing the closest results from the simulation, time frames in Tables 4.5 and 4.6 were found.

In these, $E22_{DIC}$ are the same experimental strain amplitudes collected in Tables 3.1 and 3.2, while $E22_{sim}$ are the deformation values extracted from the proper time frames of the simulation. It was chosen the closest value to the

Table 4.6: Time frame identification for the smooth specimens, Set 2

time (s)	time frame	$E22_{DIC}$	$E22_{sim}$
0.73	22	3.90E-04	3.94E-04
1.01	29	5.50E-04	5.58E-04
1.33	37	7.50E-04	7.52E-04
1.33	37	7.50E-04	7.52E-04
2.05	55	1.20E-03	1.20E-03
2.13	57	1.25E-03	1.26E-03
1.61	44	9.25E-04	9.26E-04

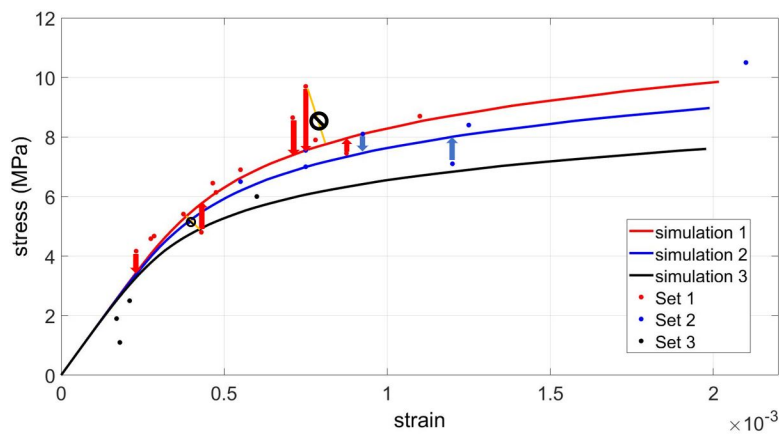


Figure 4.6: Time frames identification. Example for the smooth specimens (see Figure 3.16)

experimental data, so that the selected time frame could be suitable for the description of the experimental hysteresis loop. The same values rejected during the model calibration were not considered in this case, as time frame 34 for Set 1. Furthermore, for problems explained in the next section, the time frame 13 for Set 1 data wasn't considered.

As shown in Figure 4.6, the approximation point, owing to the choice of entities for the comparison, was found by the intersection of the simulation curve and a vertical line passing through the experimental data. In this way, if the simulation results are considered, the experimental stress loses its meaning because it is usually far away from the value computed by the simulation at the same strain amplitude. Since each experimental point is interpolated by the simulation curve, a more accurate work should have been to identify each time frame considering both the stress and strain values, thus projecting the experimental point on the closest point of the cyclic curves, with an oblique line (see Figure 4.6). Being the cyclic stress-strain curve quite flat and the experimental data not too much scattered, no big errors are committed by using a vertical line for the time frames identification.

Table 4.7: Time frame identification for the irregular specimens, Set 1

time (s)	time frame	d_{DIC}	$d_{simulation}$
0.157	32	7.29E-03	7.29E-03
0.162	33	7.45E-03	7.52E-03
0.122	25	5.56E-03	5.65E-03
0.237	48	1.11E-02	1.11E-02
0.202	41	9.45E-03	9.42E-03

Table 4.8: Time frame identification for irregular specimens, Set 2

time (s)	time frame	$d_{measured}$	$d_{simulation}$
1.000	35	6.70E-03	6.73E-03
0.885	26	4.59E-03	
1.925	52	1.04E-02	1.05E-02
1.405	39	7.56E-03	7.60E-03
1.125	32	6.10E-03	6.07E-03
1.565	43	8.48E-03	8.48E-03

Irregular Specimen

Regarding to the irregular specimen, the DIC technique was used in order to measure the specimen deformation along the average of the longest segments in Figure 4.4 (as already discussed in Section 4.2.2). Thus, the experimental deformations collected in Tables 4.2 and 4.3 and called *relaxed strain amplitudes* are already the needed global strains. However, the time frames identification was performed, since the point highlighted in Figure 4.5 can't be exactly correspondent to that coordinate (even if a negligible error would be done).

Since in this case the measured deformation couldn't be directly used as comparison parameter between the experimental data and the simulations, it was converted in the displacement of the extreme point of the same segments (highlighted in Figure 4.5). Then, this entity was used in order to find the correspondent time frames, computing the output displacement in the same point.

The output displacement d is computed on an half of the total measurement segments:

$$\varepsilon_{DIC,rel} = \ln\left(\frac{l_0 + 2 \cdot d}{l_0}\right) \quad , \quad d = (e^{\varepsilon_{DIC,rel}} - 1) \frac{l_0}{2}. \quad (4.1)$$

From the Equation 4.1, the entities d_{DIC} (mm) were computed and collected in Tables 4.7 and 4.8, where the closes simulation time frames were chosen and the proper time frames were identified. In this case, for Set 1 the last data (not included in the table) was rejected since it has a deformation which exceed the field covered by the simulation. For Set 2, the time frame 25 was rejected. Indeed, it would have worsened $\varepsilon_g - N$ curves and elaborations in the following sections.

Once each experimental data was identified in a certain time frame, stress-strain conditions in all the specimen for each experimental test were known, thus

Table 4.9: Data for $\varepsilon_g - N$ plots, Set 1

Smooth			Irregular		
time frame	ε_g	N	time frame	ε_g	N
22	4.14E-04	1100000	32	6.94E-04	97181
23	4.37E-04	486000	33	7.16E-04	98359
26	5.04E-04	227838	25	5.38E-04	130051
39	7.97E-04	104000	48	1.06E-03	37129
33	6.61E-04	101000	41	8.97E-04	23829
35	7.06E-04	110000			
47	9.78E-04	62500			
16	2.82E-04	3570000			
19	3.48E-04	2207600			
15	2.60E-04	6297000			
24	4.59E-04	839000			

Table 4.10: Data for $\varepsilon_g - N$ plots, Set 2

Smooth			Irregular		
time frame	ε_g	N	time frame	ε_g	N
22	3.73E-04	23150	35	6.40E-04	50114
29	5.18E-04	120000	52	9.97E-04	26595
37	6.86E-04	63373	39	7.24E-04	33516
37	6.86E-04	105000	32	5.78E-03	63854
55	1.07E-03	55875	43	8.08E-04	32885
57	1.11E-03	29000			
44	8.33E-04	29630			

the *global strain* ε_g could be computed.

4.3.2 Global Strains

Regarding to the smooth specimen, from the identified time frames the displacement of the point highlighted in Figure 4.5 was extracted. Then, the global strain was computed:

$$\varepsilon_g = \ln\left(\frac{l_0 + 2 \cdot d}{l_0}\right).$$

Finally, from the definition of the global strain, the values concerning to the irregular specimen were computed in the same way from the output displacements.

The global strains for both the specimens, together with the number of cycles to failure N (taken from Tables 3.1 and 3.2 for the smooth specimen, from Tables 4.2 and 4.3 for the irregular one) are resumed in Tables 4.9 and 4.10. These data were used in order to plot the scattered Figures 4.7 and 4.8. From these figures is evident that all the data concerning to the *irregular specimen* are under the scattered data coming from the smooth one. This behaviour can be

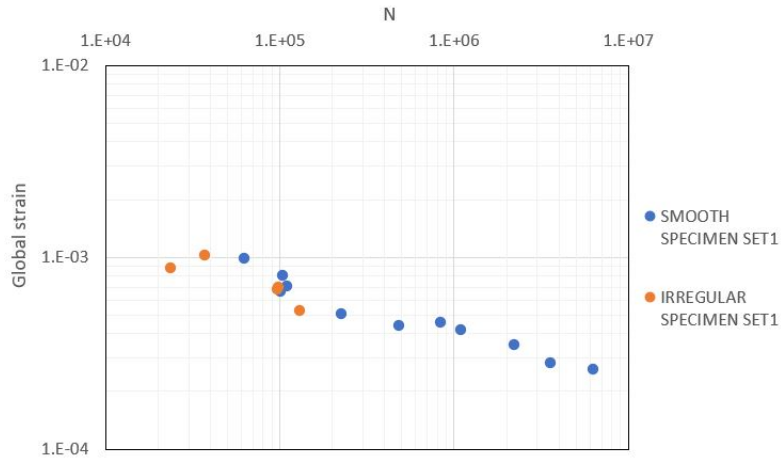


Figure 4.7: $\varepsilon_g - N$ plot, Set1 data

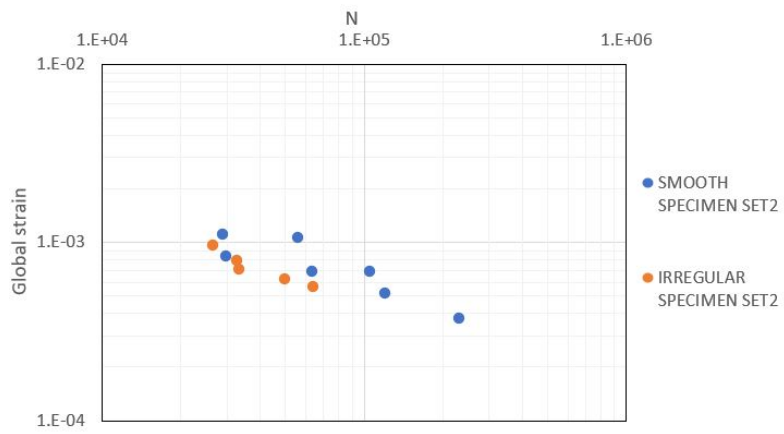


Figure 4.8: $\varepsilon_g - N$ plot, Set2 data

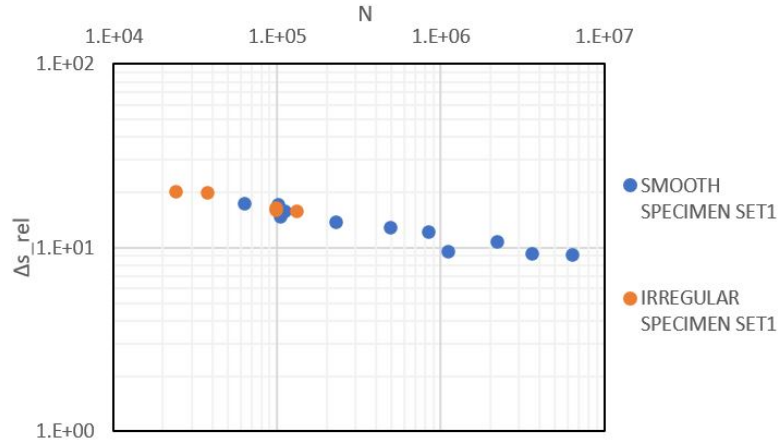


Figure 4.9: Nominal stress range - N, Set1 data

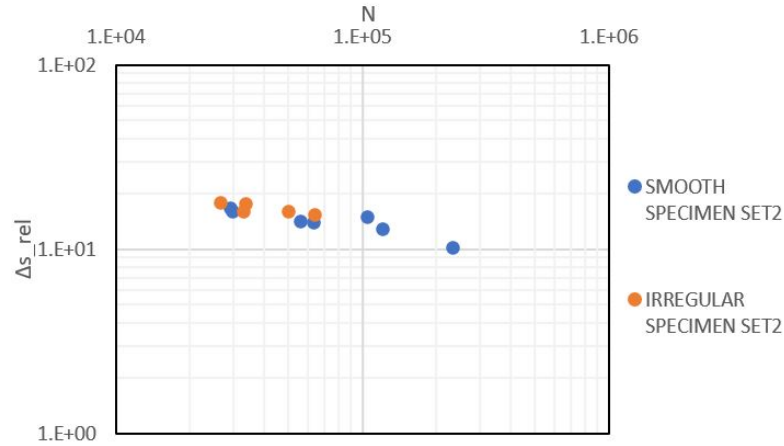


Figure 4.10: Nominal stress range - N, Set2 data

associated to the notch effect on the specimen, thus in the following the CMB interpolation of the experimental data was performed.

Finally, in order to confirm the choice made in the study of $\varepsilon_g - N$ plots, rather than $\sigma_g - N$, the Figures 4.9 and 4.10 have been plotted. A clear distinction between the smooth and irregular specimen's experimental data couldn't be done and for this reason the global strain was chosen as reference entity. Thus, the $\varepsilon_g - N$ plots were interpolated, in order to obtain an average behaviour of the experimental data.

4.3.3 Coffin-Manson-Basquin Interpolation

The more suitable interpolation equation for plots like $\varepsilon_g - N$ is the *Coffin-Manson-Basquin* (CMB) equation. This, as explained in Section 2.1.2, is given by a summation of two exponential terms:

$$\varepsilon_{Ba} = A_{el} \cdot N^{-b_{el}} \quad ; \quad \varepsilon_{Co-Ma} = A_{pl} \cdot N^{-b_{pl}}.$$

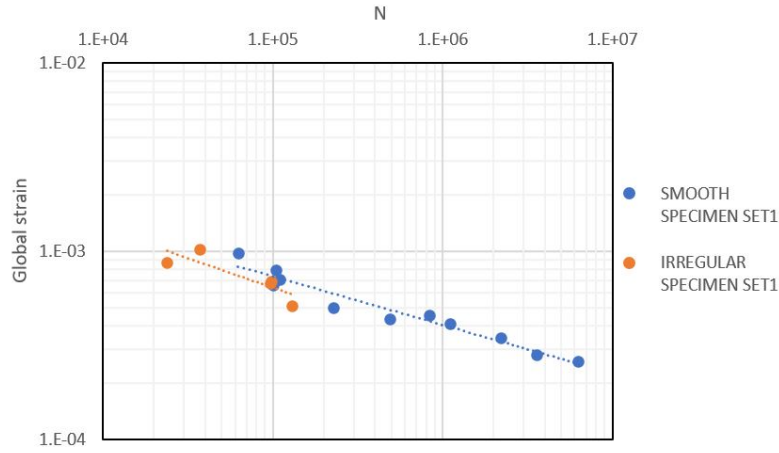


Figure 4.11: Example of wrong Coffin-Manson interpolation, with a single exponential term

Where ε_{Ba} contains the effect of the elastic strain components ε_{el} , while ε_{Co-Ma} is given by the interpolation of the plastic strain components ε_{pl} with respect to the number of cycles to failure.

Since the lead behaviour is mainly characterised by the plastic field, the elastic term ε_{Ba} could have been considered piecewise constant (on a logarithmic plot) with respect to N . This would have consisted in using a single exponential term for the interpolation of the $\varepsilon_g - N$ fatigue curves. In this way, not negligible errors were obtained, in particular on Set 1 data for the smooth specimen. In detail, an example of this wrong interpolation is plotted in Figure 4.11. Here is evident that, for the smooth specimen (Set 1) data at higher number of cycles have a huge weight on the curve slope and they are leading to obtain a wrong slope on the region of interest, which is the one at lowest number of cycles (where the comparison between the results had to be performed). This problem could have been solved by performing an interpolation just with the experimental data at the lowest number of cycles, but this would have led to a not enough robust fatigue curve. Indeed, rejecting or considering a single different data, interpolation parameters were changing radically. For these reasons, a complete interpolation was performed, with few distinctions between smooth and irregular specimens.

Smooth Specimen

In order to perform the CMB interpolation, the *global strain* in Tables 4.9 and 4.10 must be separated in its elastic and plastic components $\varepsilon_g = \varepsilon_{el} + \varepsilon_{pl}$ considering that, from the Ramberg-Osgood (RO) relationship:

$$\varepsilon_{el} = \frac{\sigma}{E} \quad \wedge \quad \varepsilon_{pl} = \left(\frac{\sigma}{k'}\right)^{1/n'}$$

Even if ε_g is not a local strain (thus the $\sigma - \varepsilon$ curve on which is lying couldn't be the local one found in Figure 3.16, as discussed in Section 2.1.3), the simulation curve was used. Later it was verified that the stress and strain intensification on the smooth specimen (which is due to its hourglass shape) is

not influential and that also the global entities are well described by the local curves. Thus, few conditions must be specified:

- RO parameters k' and n' are describing the simulation curve, rather than best fitting ones. For this reason, the modified parameters k'_{new} and n'_{new} in Table 3.8 were used;
- The stress σ linked to the global strain is unknown. Indeed, the experimental data (collected in Tables 3.1 and 3.2) have the same ε_g as a consequence of the time frames selection (see Figure 4.6), but using the nominal stress in order to compute $\varepsilon_{el} + \varepsilon_{pl}$ would lead to a global strain given by the intersection between the simulation curve and an horizontal line passing through the σ_n .

Thus, an iterative procedure was performed in order to compute the stress value associated to the global strain. This means that, knowing ε_g values, the σ which respects the condition $\varepsilon_g = \varepsilon_{el} + \varepsilon_{pl}$ was computed. In particular, σ was found for each global strain by means of Excel Solver, in order to respect the following equation:

$$\frac{\frac{\sigma}{E} + \left(\frac{\sigma}{k'_{new}}\right)^{1/n'_{new}}}{\varepsilon_g} = 1.$$

These computations were done neglecting the fact that in the reality also the creep deformation is present. Therefore, this means that these are not the *real* elastic and plastic components (as creep is just divided between them), but they are assumed to be that only for the interpolation purpose. Thus, the interpolation of elastic and plastic strain components was separately performed for both Set 1 and Set 2 data. In Figure 4.12 is plotted the example of interpolation for the strain components in Set 1 data for the smooth specimen, while in Figure 4.13 is plotted an example of why few experimental data were rejected. They had a huge weight on the slope of the interpolation curve, which would have led to errors in the computation of k_f .

In conclusion, the interpolation parameters of the equation

$$\varepsilon_{Co-Ma-Ba} = A_{el} \cdot N^{-b_{el}} + A_{pl} \cdot N^{-b_{pl}}$$

are collected in Table 4.11. A detail of the fitting curve overlaid to the experi-

Table 4.11: Global displacement curve interpolation parameters for smooth specimen

	Set 1	Set 2
A_{el}	0.0029	0.0033
b_{el}	-0.153	-0.18
A_{pl}	10.168	85.863
b_{pl}	-0.922	-1.153

mental values is plotted in Figure 4.14, where is evident that the interpolation gives a good approximation of the experimental fatigue results. Thus, even if also in the smooth specimen the strain field is not perfectly uniform (see Figure 3.14), considering the *global* $\sigma - \varepsilon$ curve as if it were overlaid to the local one, led to negligible errors. All the interpolations are plotted at the end of this section.

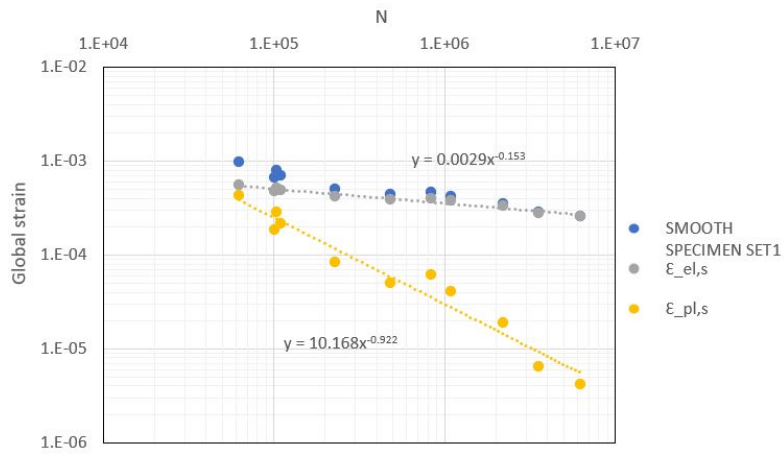


Figure 4.12: Interpolation of strain elastic and plastic components for the smooth specimen

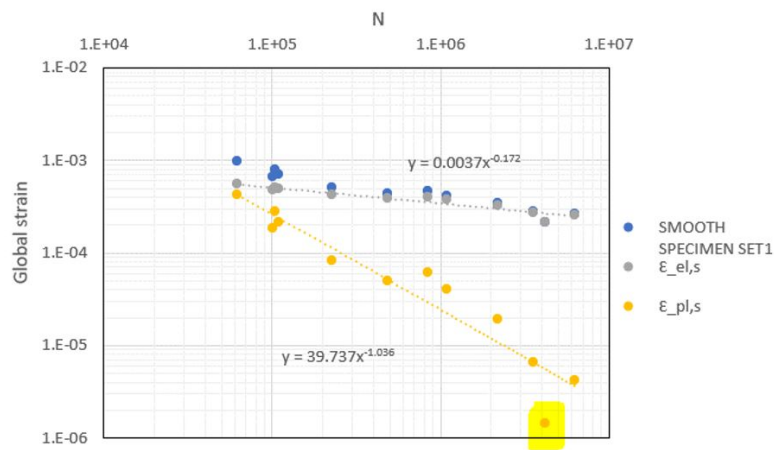


Figure 4.13: Effect of the rejected data on the interpolation curve

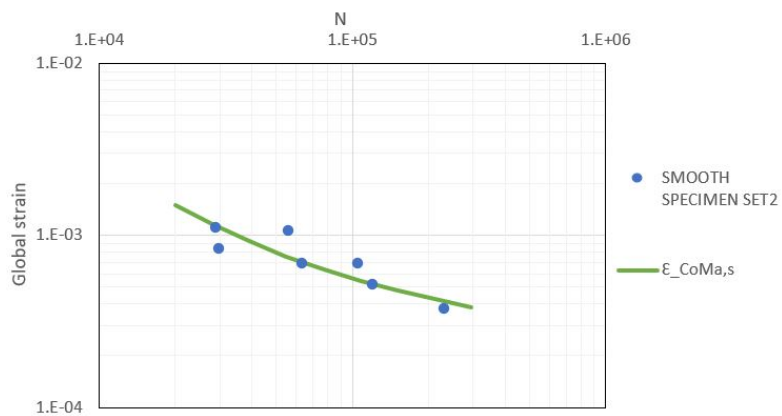


Figure 4.14: Interpolation of scattered data for smooth specimen, Set 2

Table 4.12: Global displacement curve interpolation parameters for irregular specimen

	Set 1	Set 2
A_{el}	0.0021	0.0025
b_{el}	-0.153	-0.18
A_{pl}	7.4	66
b_{pl}	-0.922	-1.153

Irregular Specimen

In the case of the irregular specimen the $\varepsilon_g - N$ interpolation had a complication. Indeed, as explained in section 2.1.3, the strain intensification owing to the notch presence lead to have a *global* $\sigma - \varepsilon$ curve which is not any more correspondent to the simulation curve (see Appendix A.3 for further discussions). For this reason, the ε_g collected in Tables 4.9 and 4.10 were not divided into the elastic and plastic strain components (since the simulation or best fitting RO parameters were not representing the global curve), but the CMB interpolation parameters for the $\varepsilon_g - N$ curve were manually adjusted.

This is the simplest way which allows to obtain an acceptable interpolation when few and scattered data are considered. It consists in using the same elastic and plastic *slope* parameters b of the smooth specimen interpolation (see Table 4.11), changing manually the *intercepts* A . In particular, the ratio of the elastic and plastic parameters A was maintained constant between the smooth and irregular specimens. This means that the degrees of freedom were not any more two (A_{el} and A_{pl}) but just one of them. Indeed, the second allows to maintain a constant proportion between the smooth and irregular fatigue curves:

$$A_{el,irr} = \frac{A_{el,smo}}{A_{pl,smo}} \cdot A_{pl,irr}.$$

Even if this is not an accurate procedure, it can be considered satisfactory since the irregular specimen's data are too less to obtain a good interpolation.

This choice led to compute a constant *fatigue notch factor* k_f and, even if it could have been supposed a variation of it with respect to the number of cycles to failure N , this expectation couldn't be verified with the few available data. The solution of the problem can be optimised in this direction, performing an higher number of tests, which would allow to perform a more correct interpolation of the irregular fatigue curve, thus to analyse an eventual variation of k_f with respect to N . In particular, the scattered data $\sigma - \varepsilon_g$ could be plotted and the interpolation curve (see Figure 2.9) would allow to find its RO parameters, further than the *apparent* Young modulus (generally higher than the real one). By means of these data the stress correspondent to the global strain could be computed, allowing the decomposition of the strain in its *apparent* elastic and plastic components, useful for a more correct CMB interpolation. Finally, the interpolation parameters for the $\varepsilon_g - N$ curve for the irregular specimen ($\varepsilon_{C0-Ma-Ba} = A_{el} \cdot N^{-b_{el}} + A_{pl} \cdot N^{-b_{pl}}$) are collected in Table 4.12. The choice of the free parameter $A_{pl,irr}$ was driven by a *safety* consideration, thus giving a bigger weigh to the experimental data under the final fatigue curve.

At the end, the obtained interpolation for the scattered data in Figures 4.7 and 4.8, were plotted in Figures 4.15 and 4.16. It can be deduced that the fatigue

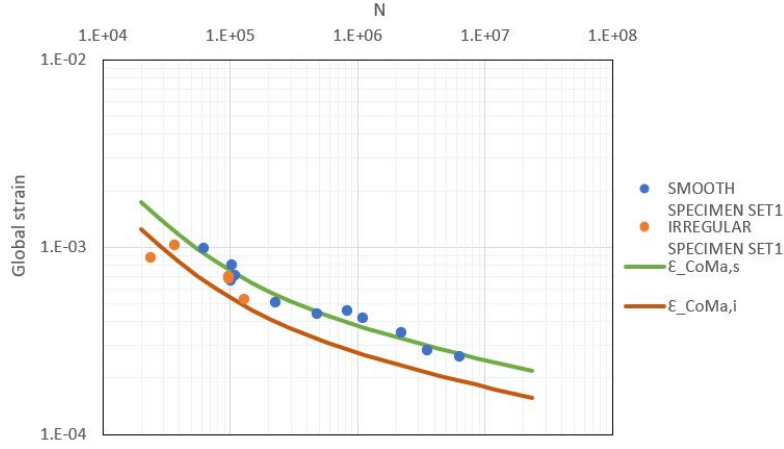


Figure 4.15: Global strain - N smooth and irregular specimen interpolation, Set 1

life is lower for the irregular specimens, being them subjected to a stress and strain intensification. Even if in Figure 4.15 the interpolation of the irregular fatigue curve could fit better the experimental data, they are too less to pretend that this is not the actual interpolation curve. Since a choice in the selection of CMB parameters had to be done, the same was performed for both the set of data.

Concerning to the smooth specimen fatigue curves, the Ramberg-Osgood *new* parameters were then verified, being the interpolations for the smooth specimen adequate. Thus, the global curve for the smooth specimen is effectively corresponding to the local one. These are the plots from which the *fatigue notch factor* was computed. Indeed, even if the crack nucleation and propagation are associated to the most solicited point, the study of $\varepsilon_{max,eq} - N$ plots (where $\varepsilon_{max,eq}$ is the equivalent strain in the most solicited point) wouldn't be representative for two reasons:

- Historically *global plots* are used for studying fatigue problems, since in this way a direct comparison with the smooth specimens results can be performed;
- The *local* stress and strain values coming from the simulations are affected by the $k_t-k_\sigma-k_\varepsilon$, as it will be explained later. Thus, it has no sense to study the fatigue intensity factor k_f on $\varepsilon_{max,eq} - N$ plots, being the N dependence on $\varepsilon_{max,eq}$ not realistic from the fatigue point of view.

4.3.4 k_f Computation

Once the fatigue curves in Figures 4.15 and 4.16 were known, the difference between the smooth and irregular behaviour (with respect to the number of cycles to failure N) was associated to the *fatigue notch factor*. This, from Equation 2.6, is defined at *constant* number of cycles N as:

$$k_f = \frac{\sigma_{n,smooth}}{\sigma_{n,irregular}},$$

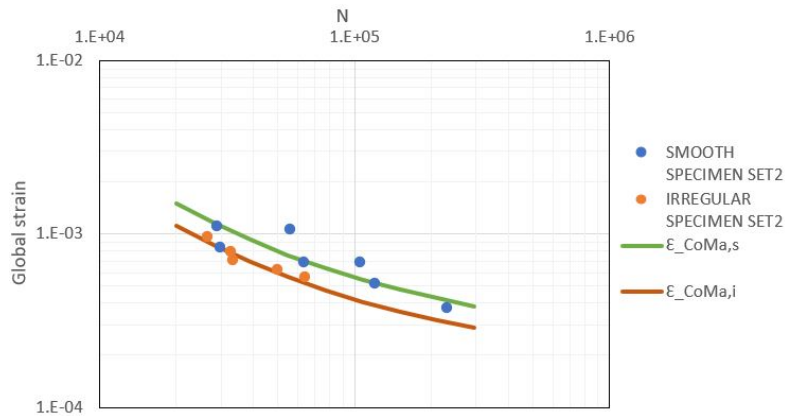


Figure 4.16: Global strain - N smooth and irregular specimen interpolation, Set 2

Table 4.13: Fatigue notch factors for Set 1 and Set 2 data

	Set 1	Set 2
k_f	1.37	1.30

where n represents the *net section stress*. Even if usually the computed value of k_f could depend on the number of cycles N , when a design for unlimited life is performed, the reference number of cycles $N = 10^6$ is usually chosen, while if the planned life is in the LCF domain k_f can be defined for $N = 10^3$. The reason why a constant k_f is usually chosen is discussed in Appendix A.3.

Since in this case the stresses hadn't been taken into account, the same definition of the fatigue notch factor was used for the global strain amplitudes:

$$k_f = \frac{\varepsilon_{n,smooth}}{\varepsilon_{n,irregular}}.$$

Being the fatigue curves described both in the HCF and LCF domains, k_f was computed for each N (rather than for a reference value). However, owing to the choice made for the interpolation of the fatigue curves, the fatigue notch factor has a constant value.

Fixing the number of cycles N and computing ε_g for both the specimens with the CMB interpolation curves in Figures 4.15 and 4.16, k_f was computed. The results for both Set 1 and Set 2 data are plotted in Figure 4.17. Other choices during the interpolation (as same slope parameters b , but independent intercepts A) would have led to a sharply decreasing k_f from a value near to k_t (elastic intensification factor) at the lowest number of cycles and to an asymptotic value at high N between 1 and 1.2. This could be the reason why, in HCF domain (thus when only the elastic field is present) a constant value of k_f is always given.

Again, the values in Table 4.13 are valid just in the case of lead working near the tests conditions, thus where the interpolation of fatigue curves is reliable. From the definition of *notch sensitivity*, which computation is the target of this work, the *Strain intensity factor* must be computed.

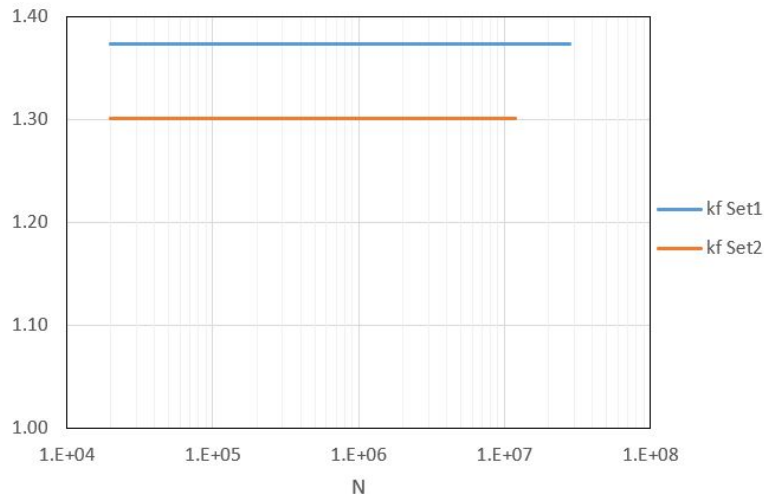


Figure 4.17: Fatigue intensity factor for Set 1 and Set 2 data

4.4 Strain Intensity Factor

To simulate in the computer a complete fatigue test with each cyclic loading, it would request a huge amount of computing time, further than a more complex and complete description of the material behaviour along its life (as hardening or softening properties, number of cycles computation. . .). For these reasons the flow monotonic curve can be substituted with the cyclic stress-strain curve, as it was done until now for all the models. In this way, every point on the covered curve well represents the stress-strain conditions for a fatigue test with that stress and strain amplitudes. Thus, the cyclic curve can be used in the model in order to resume all the possible fatigue stabilised conditions in one simulation.

Being clear the reason why a monotonic simulation can be associated to several fatigue tests, also the conditions in which the results are not any more reliable should be known. Indeed, even if the cyclic stress-strain curve is covered by the simulation, Abaqus still considers it as a monotonic flow curve. Thus, the element which is missing in order to compute the notch sensitivity is the distinction between the *statical notch factor* k_t and *fatigue notch factor* k_f . Since the *fatigue notch factor* was computed from the global strain values, rather than the stresses, also the *stress intensity factor* (which is the commonly used in the High Cycle Fatigue HCF domain) was not considered relevant. For this reason, the *strain intensity factor* was used in the local irregularity effect evaluation.

If the *fatigue notch factor* was computed from the fatigue curves considering the global strain ε_g , the *strain intensity factor* concerns the *local effects* of the irregularity. Thus, it was computed considering the comparison between the *local maximum strain* for the irregular and smooth specimens by means of $\varepsilon_{max,eq} - \varepsilon_g$ plots. Indeed, k_t in the elastic field and k_ε in the plastic one are defined at *constant global strain* as:

$$k_t = \frac{\varepsilon_{max,eq,irr}}{\varepsilon_{max,eq,smo}}$$

Even if the stress and strain intensification factors are usually computed with respect to an ideal linear-elastic behaviour, in this case the reference situation

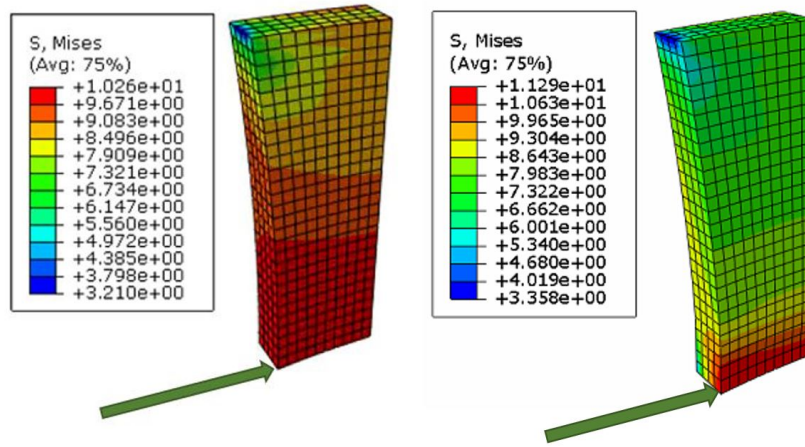


Figure 4.18: Most solicited points. On the left smooth specimen, on the right irregular specimen

was associated to the stress-strain history of the smooth specimen. This choice was done since the k_ε historical definition is valid when the component is globally in its elastic field and a plastic deformation is locally encountered owing to the notch effect, while in this case all the specimen faces a plastic deformation. Thus, in order to compute the strain intensity factor in all the global strain domain, few steps were faced:

- Extrapolation of the global strain ε_g from all the time frames of the irregular and smooth specimens simulations;
- $\varepsilon_{max,eq}$ computation:
 - Identification of the most solicited point.
- k_t computation in all the global strain domain.

In the same way done in Section 4.3.2 for the global strain computation, in this case the *displacement* of the node highlighted in Figure 4.5 was extracted as output from each time frame of the simulations. Then, the most solicited point, useful for the computation of the *maximum equivalent strain amplitude* was found.

4.4.1 Most Solicited Point

The most solicited point was found running a simulation and identifying the highest Von Mises stress values with the *Probe values* command. Several nodes were selected and, as a result, the element containing the nodes with the highest stress values are pinpointed in Figure 4.18. In both the models, this element corresponds to the external one from the concave side. Values plotted in this figure are corresponding to the last time frame covered by the simulation and their only purpose was to determine the most solicited point. This is considered guilty for the fatigue failure in each time frame (thus in each experimental test) as, being the most solicited one, it's probably the point from

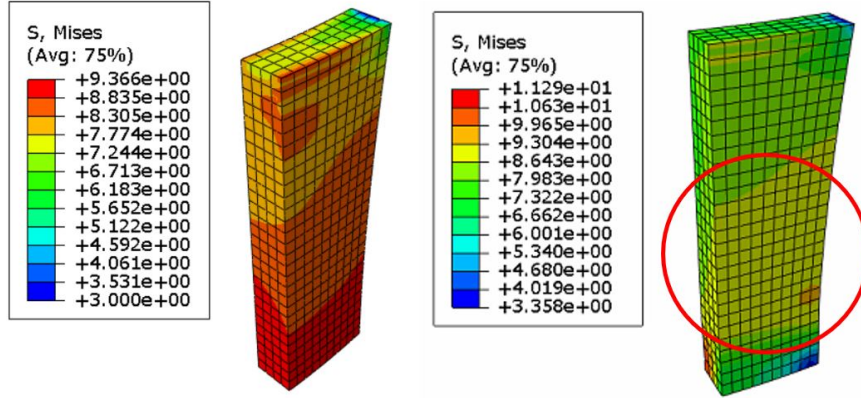


Figure 4.19: Stress intensification on the back side. On the left smooth specimen, on the right irregular specimen

where the crack starts nucleating and propagating. In particular, the integration node 2 of element 1120 was chosen for smooth specimen, while the node 2 of the element 2040 for the irregular one.

For the irregular model simulation it can be seen clearly the intensification effect of the irregularity in the mean section from the concave side. From the convex one, another less damaging intensification effect is present and the comparison between the two geometries was plotted in Figure 4.19. Finally the *equivalent maximum strain range* and the *equivalent stress* were computed.

Equivalent Stress and Strain

The maximum equivalent strain amplitude $\varepsilon_{max,eq}$ in the most solicited point was defined by means of the following equation [7]:

$$\varepsilon_{eq} = \frac{2}{3} \cdot \sqrt{\frac{3(e_{xx}^2 + e_{yy}^2 + e_{zz}^2)}{2} + \frac{3(\gamma_{xy}^2 + \gamma_{yz}^2 + \gamma_{zx}^2)}{4}}. \quad (4.2)$$

Other equations valid for the *equivalent strain rate* computation were found elsewhere [5, 19]. Despite of that, the results were differing by a negligible value (under 5%) and the Equation 4.2 was used.

Extracting all the six entities e_{xx} , e_{yy} , e_{zz} , γ_{xy} , γ_{yz} and γ_{zx} from the most solicited point at each time frame, the *maximum equivalent strain amplitude* was computed. Then, from the same point also $\sigma_{max,eq} = \sigma_{VM}$ was known. When local effects are considered, it has no meaning to compare them with respect to the number of cycles. Indeed, even if the fatigue failure starts from the most solicited point, which (for this reason) could be taken as reference point in the fatigue curves, it must be reminded that simulations results are corresponding to a monotonic curve. Thus, the maximum values have no meaning from the fatigue point of view, but they are just highlighting the presence of an intensity factor k_t and k_ε . Finally, $\varepsilon_{max,eq}$ and ε_g were plotted together in Figures 4.20 and 4.21. Considering the smooth specimen as the *nominal* condition, the ratio

$$k_t = \frac{\varepsilon_{max,eq,irr}}{\varepsilon_{max,eq,smo}}$$

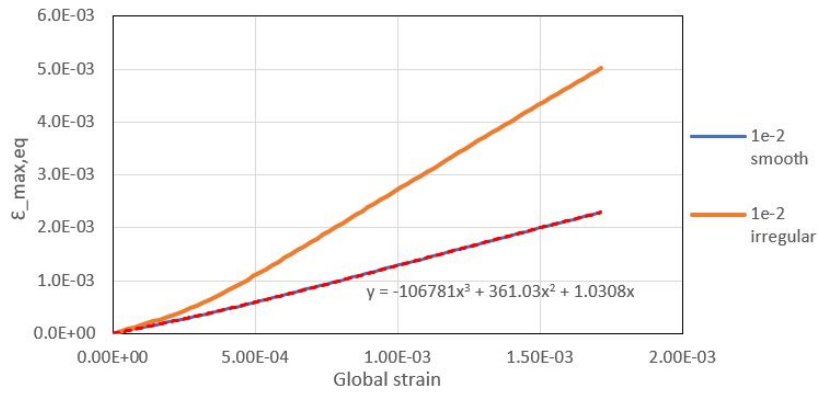


Figure 4.20: $\epsilon_{max,eq}$ - Global strain, Set1

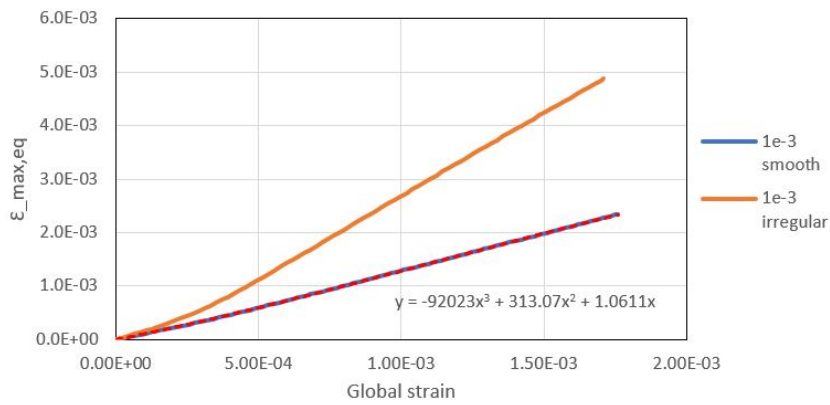


Figure 4.21: $\epsilon_{max,eq}$ - Global strain, Set2

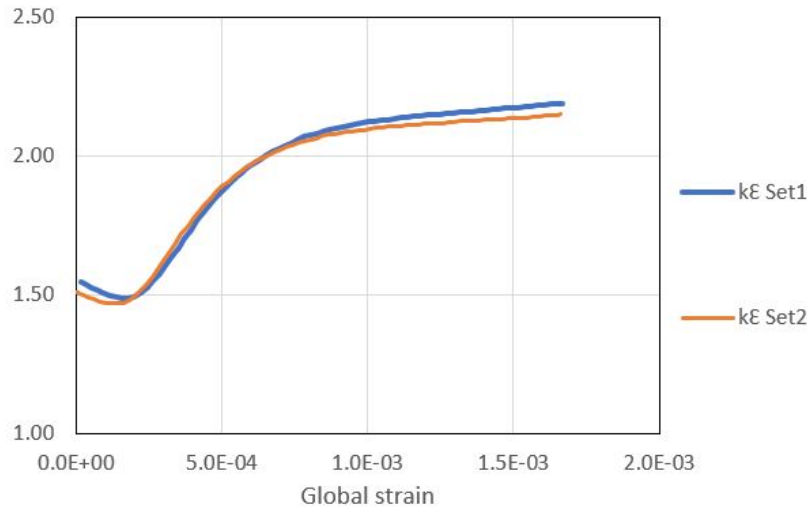


Figure 4.22: Strain intensity factors in all the global strain field, for both nominal strain rates tests

was computed at constant global strain. In this way, the Figure 4.22 was obtained, were:

- k_t is constant in the elastic field and is equal to $k_t \approx 1.5$ for the data Set 1 and Set 2. Indeed, as it can be seen in Figure 3.5, the simulation curves are overlaid in the elastic field, thus there is no reason for which k_t should be different. If this doesn't occur its probable that a mistake was done in pasting the strain components or in the selection of the integration point from which consider the outputs;
- In the plastic field, k_ε is arising owing to the shape of the plastic curve. Its values tend asymptotically to $k_\varepsilon \approx 2.3$ for data Set 1 and $k_\varepsilon \approx 2.2$ for data Set 2. Even if the simulation curve is lower for the strain rates (thus an higher k_ε would be expected) $k_{\varepsilon,1} > k_{\varepsilon,2}$ since the strain intensification factor was computed at constant global strain. In this way the specimen at higher strain rate is more solicted in terms of stress and the most solited point is ahead on the plastic curve with respect to the one of the irregular specimen;
- Since the strain concentration factor is a geometrical property, its variation with respect to the strain rate was historically studied in a different way [23]. In particular, in Figure 4.23 is shown the effect of frequency for tests at different k_t , which are considered as constant values. This was done when the computational efforts were not sustainable. Since in these years the trend of k_ε can be computed easily, the proper k_ε was adopted for each strain rate condition.

Finally, after having computed the *fatigue intensity factor* and the *strain intensity factor*, the *notch sensitivity* could be computed.

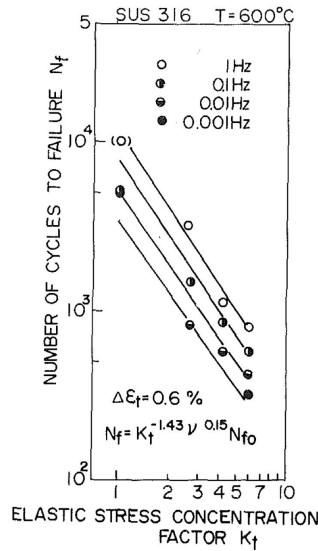


Figure 4.23: Example of frequency dependency on failure at constant k_t , for four different geometries [23]

4.5 Notch Sensitivity

From the definition of *notch sensitivity* (see Equation 2.8):

$$q = \frac{k_f - 1}{k_t - 1},$$

where generally q is depending on the global strain (owing to the strain intensity factor) and on the number of cycles to failure (owing to the fatigue intensity factor). Despite of that, in this case k_f is constant, thus q has only a variation with respect to the global strain. Furthermore, the proper k_ε was considered at each strain rate condition, so that $q = \frac{k_f - 1}{k_\varepsilon - 1}$. In Figure 4.24 its trend is plotted for both nominal strain rates. At the lowest global strain, thus in the elastic field, q is constant and its variation is linked to uncertainty in k_t computation. At higher global strain its value decreases until it stabilises near values $q = 0.3$ for Set 1 data and $q = 0.25$ for Set 2 data.

The last observations concerns to the difference between curves obtained at different strain rates. At lower strain rates, where the creep phenomenon let the plastic component arising, the notch severity is always lower and this consideration fits the expectations: materials with higher plastic behaviour are always less damaged by notch presence. Finally, in order to obtain a single value which could be used faster for design purpose, the average values were computed near testing global strain conditions. In particular, time frames from 3 before the lower experimental ε_g to 3 after the higher one were considered for the average computation. In this way constant values of *notch sensitivity* were computed for both data Set 1 and Set 2 and collected in Table 4.14.

All the obtained results are valid just in the following three conditions. First of all, the crack must start nucleating where the simulation shows the most solicited point (which means that the points taken into account and represented

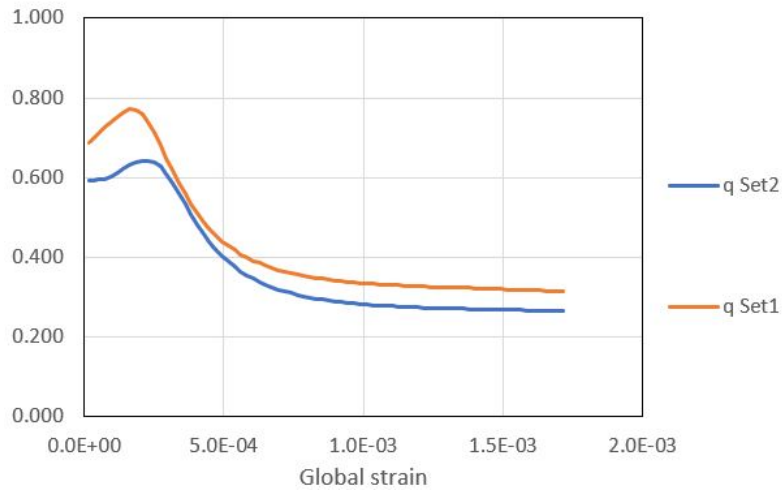


Figure 4.24: Notch sensitivity variation with respect to the global strain.

Table 4.14: Average notch sensitivity for Set 1 and Set 2 data

	Set 1	Set 2
q	0.36	0.32

by k_t are effectively responsible for fatigue failure). Otherwise, it means that the influence of the irregularity on the lead sheath is even lower than the computed one. Furthermore the results can be considered as accurate just were supported by experimental data. Indeed, they are few and too scattered to extend their interpolation to completely different strain conditions. Finally, even if in the smooth specimens the stress is not uniform in all the notched section (see Figure 3.14), this condition was considered as *nominal distribution* in the notch sensitivity computation.

In the end k_f , q and k_t were resumed in the same plot for both strain conditions in Figures 4.25 and 4.26.

4.6 Data and Results Resume

In this section a brief resume of the procedure and results for the irregularity effect on the lead specimen is discussed.

- The geometrical measured properties of the irregular specimens are collected in Table 4.1, while the dimensions assigned to the model are plotted in Figure 4.3. Experimental fatigue data are then collected in Tables 4.2 and 4.3, each for the corresponding nominal strain rate;
- The material and model properties are the same used for the model calibration and they are resumed in Section 3.5;
- The fatigue intensity factor was computed for both the data set (see Table 4.13). This was found following few steps:

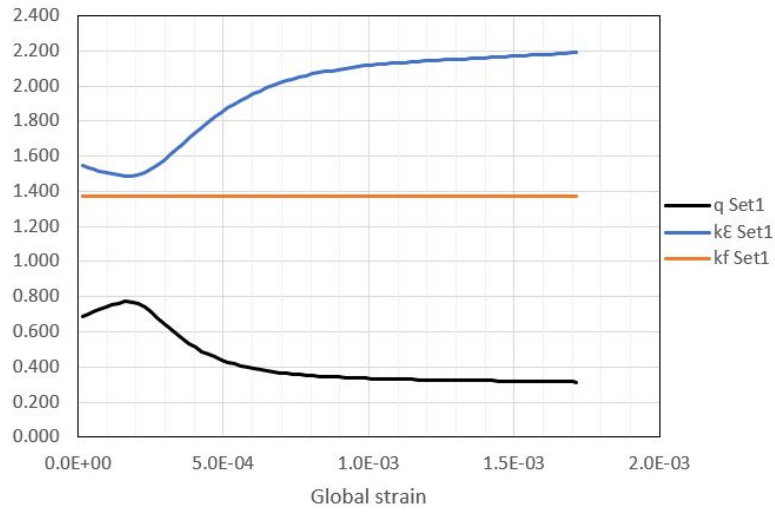


Figure 4.25: k_f , q and k_t plot for Set 1 data

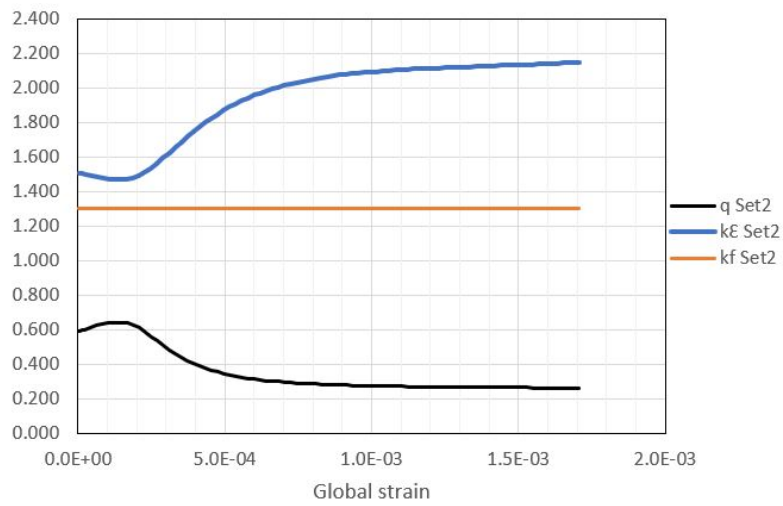


Figure 4.26: k_f , q and k_t plot for Set 2 data

- Identification of the time frames of the simulations, which are corresponding to the experimental conditions for the models of smooth (see Tables 4.5 and 4.6) and irregular specimens (see Tables 4.7 and 4.8);
 - Computation of the global strain amplitudes (collected in Tables 4.9 and 4.10) from the identified time frames, useful for plotting the $\varepsilon_g - N$ fatigue curves in Figures 4.7 and 4.8;
 - Interpolation of the fatigue curves by means of Coffin-Manson-Basquin equation, which coefficients are collected in Tables 4.11 for the smooth specimen and 4.12 for the irregular one. Thus, the interpolation curves are plotted in Figures 4.15 and 4.16.
- The strain intensity factor was then computed (see Figure 4.22). For this purpose, the most solicited point in the model was found for both the models and plotted in Figure 4.18. From this, the equivalent strain was computed in every time frame and plotted against the global strain amplitude in Figures 4.20 and 4.21, which were used in order to compute the intensity factor;
 - Finally, the notch sensitivity was computed and plotted in Figure 4.24. The average values in the field of interest (thus the one where experimental results of the irregular specimen are coming from) were computed and collected in Table 4.14. Lastly, k_ε , k_f and q were plotted together in Figures 4.25 and 4.26.

In order to compute q the fatigue tests on the smooth and irregular specimens were necessary. Once it was known, its value could be considered as a geometrical property and it could be used for considerations regarding to the real configuration of the power cable. For this reason, a section of the power cable (with a smooth and irregular Pb layer) was created and studied in the following chapter.

Chapter 5

Irregularity Influence on the Real Configuration

Once the axial fatigue tests were performed both for the smooth and irregular specimens, the influence of the irregularity in the test conditions was defined and computed in terms of *strain intensity factor* and *notch sensitivity* (see Chapter 4). In particular, the notch sensitivity can be considered as a geometrical property and its values can be generally extended also outside from the testing conditions in which it was computed. From the other side, even if the irregularity effect in fatigue conditions was characterised, these results (in terms of k_ε and k_f) could be not enough accurate in the real cable configuration. Indeed, the experimental fatigue analysis were performed with specimens surrounded by air, even if in the assembled power cable the contact between lead sheath and the surrounding layers could have some effect in the lead behaviour. Furthermore, in working conditions each layer is subjected to a multiaxial stress field with an high hydrostatic component (rather than the uniaxial stress applied as in the experimental tests) which could affect the irregularity influence on fatigue life.

In order to highlight a possible difference in terms of notch effect between the experimental tests and the real working conditions, an axisymmetric 2D model (representing the cable's section) was created with and without the irregularity on the lead layer. In this situation, the qualitative effect of the irregularity was studied by the computation of the *intensity factor* in the real configuration. Indeed, it's well known that the stress and strain intensity factors depend on the nature of the load, further than the notch geometry. In particular, the load condition was simulated by means of a *thermal cycle*, which is caused by the cable warming owing to the *Joule effect*.

This chapter is organised in the following few sections:

- Models creation:
 - Power cable section geometry and description of each layer;
 - Material properties assignment to each section. Definition of the characteristics and of the layers orientation;
 - Mesh creation;
 - Internal contact and boundary conditions assignment;

Table 5.1: Cable section geometries for a lead thickness of $t = 3.3 \text{ mm}$ [16]

Part	Components	Description	$t \text{ (mm)}$	$R_{int} \text{ (mm)}$	$R_{ext} \text{ (mm)}$
A	1	Conductor			23.15
	2	Conductor screen	0.4	23.15	23.55
B	3	Insulation	20.15	23.55	43.7
	4	Insulation screen			
	5	Serving			
C	6	Lead Sheath	3.3	44.6	47.9
D	7	PE Sheath	3.3	47.9	51.2
	8	Bedding			
E	9	Reinforcement	0.8	51.2	52
	10	Bedding			
F	11	Armor wires	3	52	55
	12	Bedding			
G	13	Armor wires	3	55	58
	14	Bedding			
H	15	Outer Sheath	6	58	64

– Loading step definition.

- Calibration of the thermal step duration;
- Outputs selection and jobs creation;
- Notch intensity factor computation and estimation of the fatigue life loss.

5.1 Cable Section Geometry

The considered submarine power cable (see Figure 1.2 for an example section) is made by several layers, which dimensions (thickness, internal and external radius) were collected in Table 5.1 [16]. The description and function of each layer was faced in Chapter 1.

Since the purpose of this chapter was to figure out the irregularity effect in terms of *intensity factor* (thus from a stress and strain point of view), even if each layer has its own mechanical properties, only few of them were modelled. These are the most relevant from the *structural* point of view. Indeed, the thinnest layers (such as the *semi conductive nylon tapes* 8, 10 and 12, further than the *carbon black paper tapes*) are useful for other purposes rather than the structural one, thus their influence on the stress and strain field is negligible. For this reason, only the layers collected in Table 5.2 were modelled, where the equivalent dimensions were computed taking into account also the small contributions coming from the neglected layers. Furthermore, the dimensions collected in Table 5.1 are concerning to a power cable in which the lead sheath has a thickness of $t = 3.3 \text{ mm}$, rather than $t = 1.8 \text{ mm}$ (which is the nominal dimension studied in this entire work). Thus, the internal and external radius of each layer in Table 5.2 were adjusted considering that the lead sheath dimensions (plotted in Figure 3.1) were fixed. In particular, the radius of the internal layers with respect to the lead one were reduced proportionally to the dimensions

Table 5.2: 2D model section geometries

Part	Components	t (mm)	R_{int} (mm)	R_{ext} (mm)
A	1			20.35
B	3	18.85	20.35	39.2
C	6	1.8	39.2	41
D	7	3.3	41	44.3
E	9	0.8	44.3	45.1
F	11	3	45.1	48.1
G	13	3	48.1	51.1
H	15	6	51.1	57.1

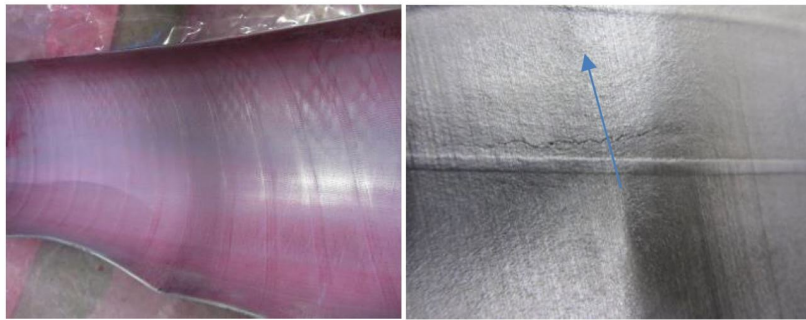


Figure 5.1: Irregularities example on the lead sheath [12]

in Table 5.1, while the external layers were maintained of the same thickness. Indeed, owing to the available data, only a *qualitative analysis* was possible, thus it was useless to know the exact thickness of each layer.

Thus, the geometrical data collected in Table 5.2 were used in order to create two *2D axisymmetric* models: one with a smooth lead sheath, the second with the same irregularity studied in the previous chapter. The 2D axisymmetric model was chosen in order to reduce the computational time. Indeed since this is a complex problem, a first simplified model was created even if this choice has some limitations in the applicable loads. This allowed to produce a refined mesh, which is able to describe a more accurate stress and strain field in all the cable section and in particular near to the irregularity.

The distance between each irregularity was not known and from Figure 5.1 an approximate longitudinal distance of 10 cm was considered. Even if in some cases the distance could be lower, it was demonstrated that the irregularities have a null or negligible influence on each other and the maximum distance at which a noise on the stress field was visible was of ≈ 3 cm. For this reason it was sufficient to model only one irregularity. Thus, a model with a longitudinal length of 5 cm and periodical boundary conditions was created. An example regarding to the geometry of the model with irregularity was plotted in Figure 5.2, where it was chosen that the irregularity of the lead sheath was entirely absorbed by the surrounding layers (rather than being transmitted and perceived through more of them). Finally, after the geometry creation, the material properties were assigned to each layer.

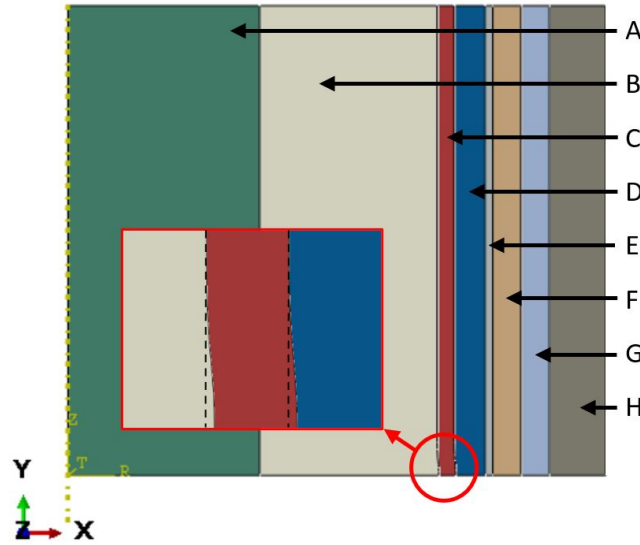


Figure 5.2: Axisymmetric model of the cable with irregularity on the lead sheath. x radial direction, y axial direction

5.2 Material properties

In this section, the material properties definition and assignment were faced. Starting from the most internal layer all the sections were defined, considering that the following material properties were given by Reference [16]. In addition to the elastic properties, also the plastic and creep ones were assigned where necessary. Then, considering that in this model the irregularity effect was studied with a thermal cycle loading condition, also the thermal volumetric expansion coefficient α_v was assigned to few layers.

During the working conditions, the cable can expand owing to the warming up for Joule effect. Presuming that at a maximum of ≈ 500 m depth the seawater temperature is around 4°C and that at stationary working conditions the temperature at the interface between lead and insulation layers can reach 50°C , a $\Delta T = 50^\circ\text{C}$ was considered as reference gap for the two layers A and B [16]. Even if in a more complex and correct model the temperature gradient should be considered and the expansion of each layer should be studied, in a first approximation the only expansion of the two most internal layers was considered. This approximation holds for the following reasons:

- Owing to the conduction between the adjacent layers and convection with the surrounding water, the other layers are subjected to a significant lower temperature gap [11];
- The thermal expansion coefficient of the other layers is negligible with respect to α_v of the MI insulation layer;
- A more accurate model would request extra informations, useless for a qualitative estimation.

Thus, a brief description of the characteristics of each layer is faced.

Layer A

High purity copper conductor, isotropic material which is supposed to work only in its linear elastic field. The Young's modulus, Poisson's ratio and the thermal expansion coefficient were assigned.

Table 5.3: Layer A material properties

E (MPa)	ν	α_v (1/K)
120000	0.34	5.1E-05

Layer B

Insulation system, which is made by Kraft paper impregnated by high viscosity oil. Since the temperature field explored by the cable during the service is low, for simplification, the insulation is assumed to be isotropic and elastic [11]. About this layer, being the insulation a complex system composed by paper and oil (see Figure 1.4), few clarifications are necessary:

- The definition of the mechanical and thermal properties is difficult and several assumptions were made. In particular, the *equivalent* mechanical and thermal properties were used [11]. Regarding to the mechanical properties, the equivalent values $E_{eq} = 10$ GPa and $\nu_{eq} = 0.45$ were given, while the equivalent expansion thermal coefficient is $\alpha_{eq} = 2.52E - 04$ 1/K. This was computed considering that only the oil gives a contribution to the thermal expansion, thus its expansion coefficient $\alpha_v = 6.3E - 04$ 1/K was multiplied by the typical volume fraction $f_v = 0.4$ occupied by the oil in the mass impregnated layer [16].
- Even if only eight layers were modelled, in the sections created are merging the material properties of the neglected components. Thus, since the copper tape (component 3) has in general not negligible structural properties, an equivalent Young's modulus and Poisson's ratio were computed for the layer B taking into account the copper tape and the Kraft paper [16]:

$$E_B = \frac{\sum(E_i \cdot I_{f,i})}{I_B} \quad , \quad \nu_B = \frac{\sum(\nu_i \cdot V_i)}{V_B}.$$

Where E_B and ν_B are the equivalent Young's modulus and Poisson's ratio, computed considering that the components merged in the layer B are in parallel each other. In particular, they were computed considering an average of the *flexural stiffness* and an average computed on the volume occupied by each component in the modelled layer. Thus, E_i and $I_{f,i}$ are the elastic modulus (for an isotropic material) and the flexural inertia of the *i*-component, while ν_i and V_i are the Poisson's ratio and volume of each component per unit length. This choice consists in another approximation, since the copper woven taper (being it a woven) should introduce negligible isotropic properties. Anyway, the same procedure adopted from the reference was repeated.

Even if these equivalent values were computed for studying the flexural behaviour of the cable (which is excluded by an axisymmetric model), they were still used since they would have been anyway affected by error. Indeed, already the value E_{eq} for the insulation is a rough estimation and, owing to the thermal cycle, this layer is subjected to a triaxial stress which is not easily definable for a more appropriate computation of E_B . Thus, the equivalent values for the layer B are collected in Table 5.4 and they were corrected considering the modified dimensions of each section, which are collected in Table 5.2.

Table 5.4: Layer B material properties

E (MPa)	ν	α_v (1/K)
20524	0.44	2.52E-04

From a comparison between the thermal expansion coefficients, it's obvious why the expansion of the other layers was neglected. The MI paper has an α_v which is one order of magnitude higher.

- The mass impregnated paper is not a continuum body, since it's characterised by the presence of cavities in which the oil is contained. In particular, a fraction of these cavities is free of oil at the lowest temperatures. Then, owing to the warming up, they become filled by oil when the insulation layer reaches a threshold temperature called *cavity free temperature*. Above this temperature, which is usually of $30^\circ C$, the insulation layer starts expanding [11]. For this reason, being the $\Delta T = 50^\circ C$ between the starting and stationary conditions, a reasonable temperature gap which causes thermal expansion can be considered of $\Delta T = 20^\circ C$ (which is the applied one in the model). In order to simplify the step definition, the same final temperature was applied to the copper conductor, which gives anyway a negligible contribution.

Layer C

The lead sheathing was modelled considering an isotropic elastic, plastic and creep behaviour (by means of the strain hardening power law). In particular, the properties collected in Section 3.5 were used, thus considering that after the cable immersion in the seawater the lead layer is facing already the stabilised conditions. This approximation was done considering the complexity of the problem and the target, which is just a *qualitative* understanding of the irregularity effect on the fatigue life.

Layer D

This layer is made by polyethylene (PE) and its behaviour is considered to be strain-rate and temperature independent (for lack of data). The isotropic elastic-plastic properties were given by Nexans Norway [16]. Since the temperature gap is lower outside from the insulation, no thermal expansion was considered. Thus, in the Tables 5.5 and 5.6 are collected the properties assigned to this layer.

Table 5.5: Layer D elastic material properties

E (MPa)	ν
600	0.46

Table 5.6: Layer D plastic material properties

σ (MPa)	ε_{pl}
2.0	0.00
3.0	1.50E-02
4.0	2.33E-02
6.0	4.00E-02
7.5	9.00E-02
9.0	1.90E-01
9.5	2.90E-01
10.0	3.90E-01
10.5	4.90E-01
11.0	5.90E-01
11.5	6.90E-01
12.5	7.90E-01
13.0	8.90E-01
13.5	1.00

Layer E

Above the polyethylene is winded up a galvanized steel tape, which purpose is to produce a tangential reinforcement in opposition to the radial deformations of the power cable (usually caused by the thermal expansion of the inner layers). Being it a tape, the provided strength acts only along the winding direction, otherwise it would slip on the adjacent layers. For this reason, this layer was modelled by means of *orthotropic* linear elastic properties (rather than isotropic).

Even if this tape is wind up with a direction of $\approx 20^\circ$ with respect to the tangential one (see Figure 5.3), that material orientation couldn't be used in an axisymmetric model. For this reason, the steel Young's modulus and Poisson's ratio were assigned along the pure tangential direction. In particular, if the local coordinate system is equal to the global one, plotted in Figure 5.2, these are $E_3 = E_t = 200000$ MPa and $\nu_{12} = \nu_{tp} = 0.3$ as reported in the Abaqus guide [1]. Then, the elastic modulus along the other directions $E_p = E_1 = E_2$ were arbitrary chosen equal to $1\%E_3$ in order to have an enough low value representative to the fact that no strength can be provided by the tape in those directions [11]. Since the *elastic matrix* $[E]$ must respect the symmetry condition, $\nu_{13} = \nu_{pt} = \frac{E_p \cdot \nu_{tp}}{E_t} = 0.003$ was computed, then $\nu_{23} = \nu_p = \nu_{13}$ was arbitrary chosen, being the directions orthogonal to the tangential one negligible from the structural point of view. Finally $G_{23} = G_p = \frac{E_p}{2(1+\nu_p)} = 997$ MPa was computed and the $G_{12} = G_{13} = G_{23}$ were arbitrary chosen. These values are respecting the *stability conditions* of the Abaqus guide and they are resumed in Table 5.7, where E_i and G_{ij} are reported in MPa [1].

A peculiarity of this layer is that it is usually winded up with a preload. In

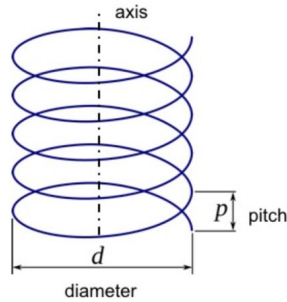


Figure 5.3: Tape winding, example

Table 5.7: Layer E orthotropic elastic material properties

E_1	E_2	E_3	ν_{12}	ν_{13}	ν_{23}	G_{12}	G_{13}	G_{23}	α_v (1/K)
2000	2000	200000	0.3	0.003	0.003	997	997	997	3.5E-5

order to model this condition an initial thermal step, which is discussed in the next section, was applied until the stress along the tangential direction (which is more or less equal to the Von Mises equivalent stress) reached the value of $\approx 200 \text{ MPa}$ [16]. Thus, also the thermal expansion coefficient was assigned (see Table 5.7). Finally, it was also verified that this layer was in its elastic field along all the simulation and a discussion about this topic is faced in the next section.

Layers F and G

Above the steel tape, two galvanized steel armours made by wires are winded. Since also in this case a detailed model would be too complex (modelling each wire as separated from the other would request a 3D model, further than more data which are not available), these armours were considered as continuum bodies with orthotropic linear elastic behaviour [16]. This approximation, as for the steel tape, allows anyway to perform a qualitative investigation of the irregularity effect on the power cable fatigue life.

In particular, the steel wires (which are used in order to provide strength along the axial direction, useful in order to sustain the cable weight during the installation) have an orientation with respect to the longitudinal one which is 12.7° for the most internal armour and -10.5° for the external one [16]. Since in an axisymmetric model the local material orientation must be concordant to the global reference frame, being the angle orientation small with respect to the longitudinal direction, the two layers were modelled considering them as laying along the axial direction. Thus, the same considerations of the layer E are valid, except for the fact that the elastic orthotropic properties were assigned in order to have the maximum strength along the axial direction (which is the direction 2). Finally, these properties (valid for both the layers F and G) were collected in Table 5.8.

Table 5.8: Layers F and G orthotropic elastic material properties

E_1	E_2	E_3	ν_{12}	ν_{13}	ν_{23}	G_{12}	G_{13}	G_{23}
2000	200000	2000	0.003	0.3	0.003	997	997	997

Layer H

The most external layer consists of an High Density Polyethylene (HDPE), which is characterised by an isotropic elastic-plastic behaviour. For lack of data it's considered to be strain-rate independent. In Tables 5.9 and 5.10 are collected its mechanical properties [16].

Table 5.9: Layer H elastic material properties

E (MPa)	ν
780	0.46

Table 5.10: Layer H plastic material properties

σ (MPa)	ε_{pl}
10	0
10.5	1.7
11.75	2
14	3
17	4
20	5

The plastic curve in Table 5.10 was partially considered, since intermediate points between the first two had the same stress value and this would have brought to errors during the simulations. Then, after having assigned the material properties to each section, all the layers were assembled together and the mesh on each of them was defined.

5.3 Mesh Creation

Since the target of the following simulations is to figure out the irregularity effect on the stress and strain field, the mesh should be enough detailed and refined in order to allow a local evaluation. For this reason, further than a small size of each element, *quadratic elements* were chosen. Then, in order to focus on the region of interest and to reduce the computational time, a mesh with a *variable seed* along the radial direction was created on each layer (rougher far away from the lead sheath and more refined closer to the irregularity).

The same size of the mesh on each section was used for both the models (the first with a smooth lead sheath, the second with the presence of the irregularity) and an example of the mesh dimensions is plotted in Figure 5.4, where a detail on the irregularity of the lead sheath is highlighted. The maximum size of the

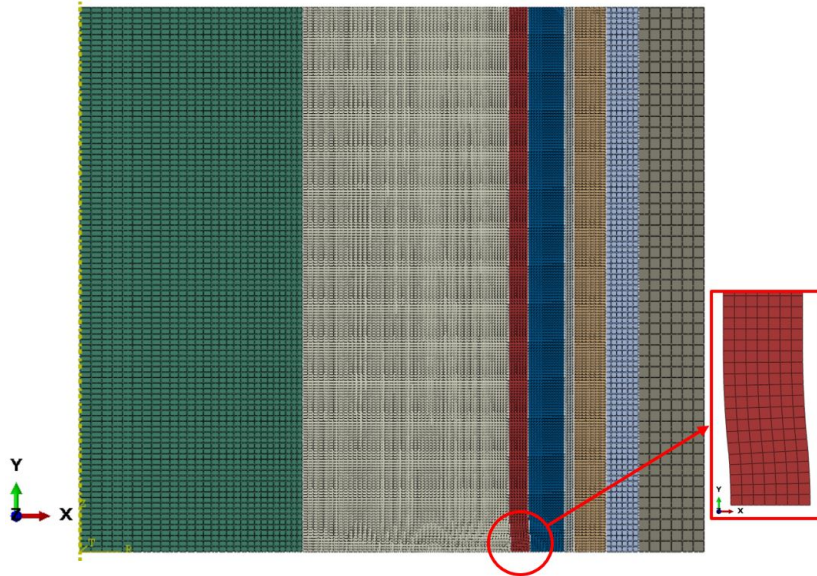


Figure 5.4: Mesh on the cable section.

elements on the lead section and closer to it is equal to 0.25 mm , while on the most internal and external layers the mesh is less detailed. These dimension were chosen after few simulations, in order to describe in a more appropriate way the stress distribution nearby to the irregularity and to demonstrate that the noise which introduces isn't affecting the other irregularities. Once the mesh was defined, the boundary conditions definition was faced.

5.4 Boundary Conditions

The boundary conditions must be able to describe a cable with infinite length, with the presence of one irregularity every 10 cm (which is the approximated axial distance between each of them). Thus, the following boundary conditions were applied independently to each external surface of the model:

- The first boundary condition was applied in order to describe a complete irregularity (since in the model just an half of it was sketched, as plotted in Figure 5.4). Therefore, an *Y-symmetry* boundary condition was adopted on the lowest side;
- Then, the choice of creating a 2D axisymmetric model represents itself a boundary condition on the cable's axis (which is represented in Figure 5.4 by the dotted line on the left side). Since the model is bidimensional each node allows a displacement only on the plane xy and, being the analysis axisymmetric, no torsional and flexural behaviour are admitted. Thus, the stress and strain components $r - c$ and $r - z$ are equal to zero (where r is the radial direction, c the circumferential and z the axial one in Figure 5.5).
- The model must be able to move along x and y directions without loosing

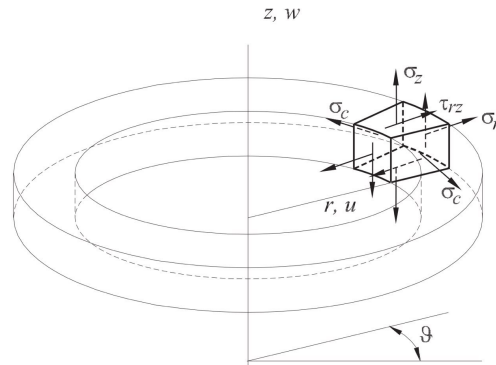


Figure 5.5: Axisymmetric stress components [9]



Figure 5.6: Comparison between boundary conditions on the upper surface. The lowest one represents the correct periodic boundary condition application.

the contact between the adjacent layers and these conditions are separately managed:

- During the thermal expansion, the cable hasn't constraints along the axial direction (except from the other side of the cable which is not modelled). For this reason, a *periodic* boundary condition was applied in order to guarantee that each layer could move along the y direction (for which the symmetry condition couldn't be applied), each with the same displacement. Indeed, owing to the fact that the model consists in a single section of the cable it would make no sense to allow different displacements for each layer along the axial direction. Since the insulation layer is the one with the highest thermal expansion coefficient, it's also the one which would like to expand the most. Instead of expanding more than the other layers along the y direction, it acts like a stretching load. A comparison between the wrong situation (thus without the periodic boundary condition) and the realistic one is plotted in Figure 5.6. The periodic boundary condition was defined by a constraint called *equation* imposing that each node of the mesh for the upper surface had a fixed displacement along the desired direction with respect to a *reference point*.
- The compatible displacement along the x direction was allowed by the imposition of a contact condition between each layer. Even if it would have been enough to use a *tie constraint* between each inner adjacent surfaces (being the displacements along y direction fixed on the upper surface, thus in all the possible intermediate sections)

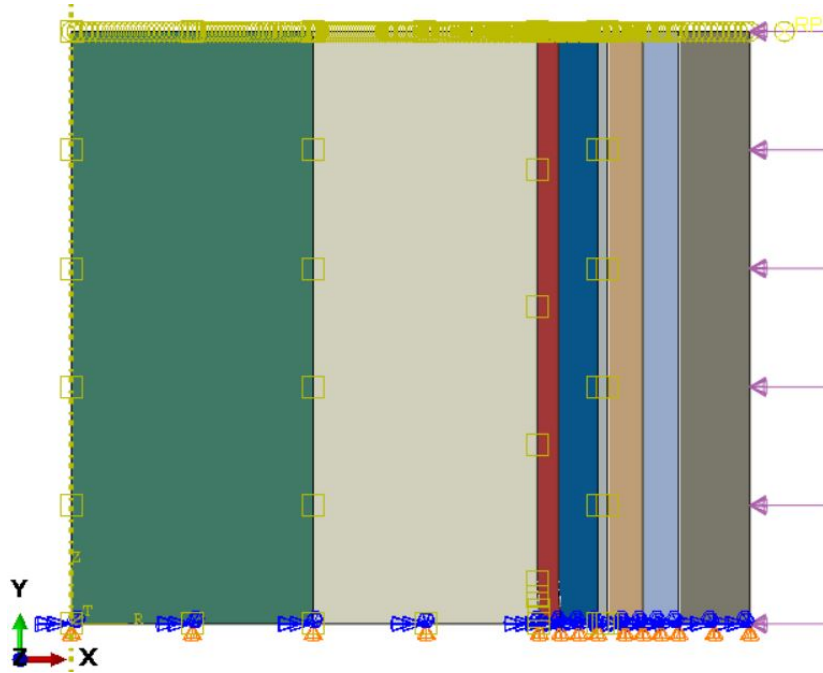


Figure 5.7: Boundary conditions resume

a contact was defined using an *Hard contact normal behaviour* and a *Penalty tangential behaviour*. In particular, the normal one was defined avoiding the separation of the surfaces after the contact, while the tangential behaviour was described by an arbitrary medium isotropic frictional factor equal to $\mu = 0.3$. This is lower than an usual contact between plastic materials or steel, since nylon and other tapes are used between each layer. The contact effect is visible in the σ_{12} component, which isn't null (even if negligible) in the model with irregularity, as discussed in the next Sections.

- The last boundary condition consists in the water pressure on the external surface (thus the right one in Figure 5.4). Even if its effect is negligible it was arbitrary chosen a maximum depth of 500 m, where the pressure is equal to $p = 5 \text{ MPa}$.

If the geometrical boundary conditions are applied during all the simulation, the water pressure was defined in a different step, which is introduced in the next section. Finally, all the boundary conditions were resumed in Figure 5.7.

5.5 Load Steps Definition

The submarine power cables are subjected to several loads in the different stages of their life (from the production, to transportation, installation and in working conditions). In general they have different origins and this work is focused on the effect of the load caused by the thermal expansion of the inner

layers (such as the conductor and the insulation system). Thus, in order to represent the real working conditions, few loading steps were created:

Initial step During the *initial* step (which is the default one) all the pre-existing conditions were implemented. In this case, the initial temperature (arbitrary, since the target is to obtain the wanted gap ΔT) for the layers A, B and E was set equal to $T_0 = 0^\circ C$. If for the first two layers the thermal expansion is useful in order to study the stress field evolution in all the power cable section, for the steel tape E the thermal load is used just in order to model a preload which is provided during the cable production.

Preload The first step, which was called *Preload*, was created in order to obtain a preload of about 200 MPa on the steel tape, thus on the layer E (which is represented in Figure 5.2) [16]. Since the lead sheath was modelled also with its creep behaviour, a *visco* step was chosen and, during this step, a final temperature of $T_f = 30^\circ C$ with a *ramp* shape was settled. This allows to introduce a temperature gap of $\Delta T = 30^\circ C$, which was verified to be enough in order to obtain the wanted σ_{VM} . Since the tape has a tangential orientation and negligible mechanical properties on the other directions, the equivalent Von Mises stress is almost equal to σ_{33} , thus the circumferential component. In particular, the step duration was set arbitrary to 1 s and the number of time frames was chosen near 10, since this step is not of primary importance for the stress and strain field study.

Water Pressure After the Preload step, the water pressure was applied considering a maximum depth of 500 m . Thus, selecting a *visco* step, a pressure of 5 MPa was distributed on the external surface of the model (which is the adjacent one to the layer H). Imposing a duration of 1 s and about 10 time frames (being this step not important from the stress-strain field evaluation), the water pressure was simulated. The main effect of this step is to introduce an higher hydrostatic stress component, which brings to reduce the slope of the equivalent stress condition in all the layers.

Thermal expansion The last step, which is the one of main interest, was called *Thermal expansion*. During this step, two different temperatures should have been defined on the layers A and B. Indeed, the layer A (copper conductor) is subjected to the thermal expansion during the whole gap $\Delta T = 50^\circ C$, while the insulation layer uses the first $30^\circ C$ in order to warm the oil until it fills the cavities and the last $20^\circ C$ for the effective thermal expansion [16]. Since the copper thermal expansion coefficient is negligible with respect to the insulation's one, in order to simplify the steps creation, the final Temperature of $T_f = 20^\circ C$ was set on both the layers.

Finally, the duration of this step was chosen in order to obtain a longitudinal strain rate $\dot{\epsilon}_{22}$ on the lead sheath equal to the strain rate measured during the experimental fatigue tests. Even if the loading condition is different from the experimental one (axial load) and a multiaxial stress-strain field is present, $\dot{\epsilon}_{22}$ was arbitrary still considered as reference entity in order to perform a comparison between the results obtained from the fatigue intensity factor computation for the specimens and the results obtained from these more realistic models. Since the experimental tests on the irregular specimens were performed at two different strain rate conditions,

two simulations for each model were performed. An iteration procedure on the thermal step duration allowed to obtain the desired strain rate. A discussion upon this topic was faced in the next subsection and the optimized step durations t are collected in Table 5.11.

Table 5.11: Thermal expansion step duration and comparison between strain rates

<i>Set</i>	$\dot{\epsilon}_m$ (1/s)	$\dot{\epsilon}_{22}$ (1/s)	t (s)
Set 1	5.23E-03	5.00E-03	0.2
Set 2	6.14E-04	5.54E-04	1.8

Set 1 and Set 2 have the same meaning of the previous chapters, thus Set 1 regards the model on which the highest strain rate was set, while Set 2 corresponds to the smooth and irregular models on which the lowest strain rate was applied. The average strain rate values $\dot{\epsilon}_m$ were taken from Table 3.7, while $\dot{\epsilon}_{22}$ corresponds to the computed strain rate for the step duration t . Then, knowing the values of t , the *increment size* during this loading step was set in order to have at least 40 time increments.

5.5.1 Thermal Step Duration

The strain intensity factor was computed in two strain rate conditions. In order to obtain the desired longitudinal strain rate, the correct thermal step duration was chosen by means of an iterative procedure. In particular, the strain rate was computed during each time frame:

$$\dot{\epsilon}_{22_i} = \frac{\epsilon_{g,22_i} - \epsilon_{g,22_{i-1}}}{t_i - t_{i-1}},$$

where $\epsilon_{g,22}$ is the *global* strain along the axial direction and t is the time instant of each time frame. The global strain was computed far away from the irregularity on the lead layer, in order to obtain a strain value which was not influenced by the noise introduced by the irregularity. Thus, the point from which the output was extracted consists in the node 1 of the element highlighted in Figure 5.8, which is adjacent to the upper surface. Since the periodic boundary condition was applied to the upper surface, the strain component ϵ_{22} is equal for each axial coordinate and the choice of the element along the x direction was indifferent.

Then, the average was performed between the strain rate $\dot{\epsilon}_{22_i}$ computed during each time frame of the *thermal expansion* step. Finally, adjusting the duration of the same step, the values in Table 5.11 were computed, which are close enough to the $\dot{\epsilon}_m$ (taken from the Table 3.7). The strain rate was computed and verified in this way for both the models (smooth lead layer and the second with the irregularity on the lead layer) in the two strain rate conditions.

Even if the duration computed is small and not realistic (since in real working conditions the cable warming duration is at least of some minutes), the following results were considered valid, being this a qualitative analysis.

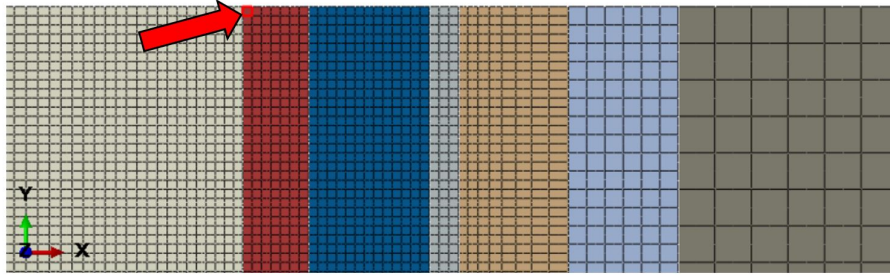


Figure 5.8: Assembly detail, element of the lead layer from which the global strain output was extracted.

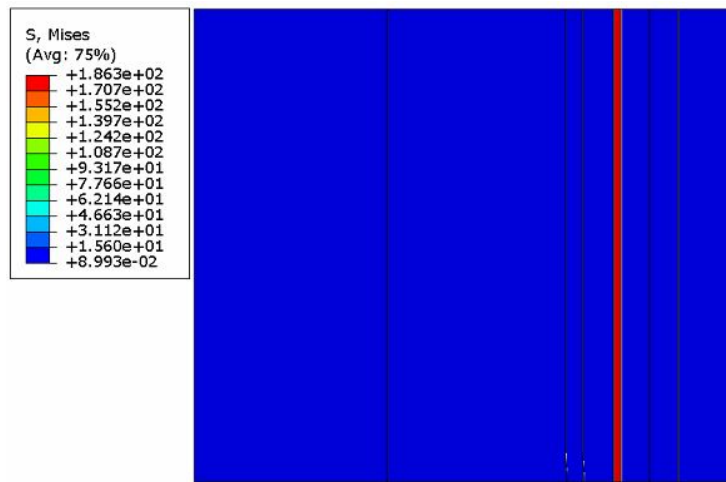


Figure 5.9: Preload stress on the steel tape. Irregular specimen, highest strain rate.

5.6 Output Selection

The necessary outputs for the correct interpretation of these models and for the results computation are regarding to few different integration points:

- The first output is useful in order to verify that the correct preload stress was reached on the steel tape ($\Delta T = 30^\circ C$ on the layer E, identified in Figure 5.2) during the *preload* loading step. Thus, the most solicited point of this layer was identified for both the models (the first with a smooth lead layer, the second with the irregular Pb layer) and this was contained in the lowest element in Figure 5.9, on the internal curvature. From this, the results in terms of σ_{VM} , which is almost equal to σ_{33} , were arbitrary selected from the integration point 1;
- The second output, which was useful for the computation of the strain intensity factor (further than the strain rate), was extracted from the element identified in Figure 5.8. From this, the strain component ε_{22} (which is called in the following as *global strain* $\varepsilon_{g,22}$) was extracted from the integration node 1;

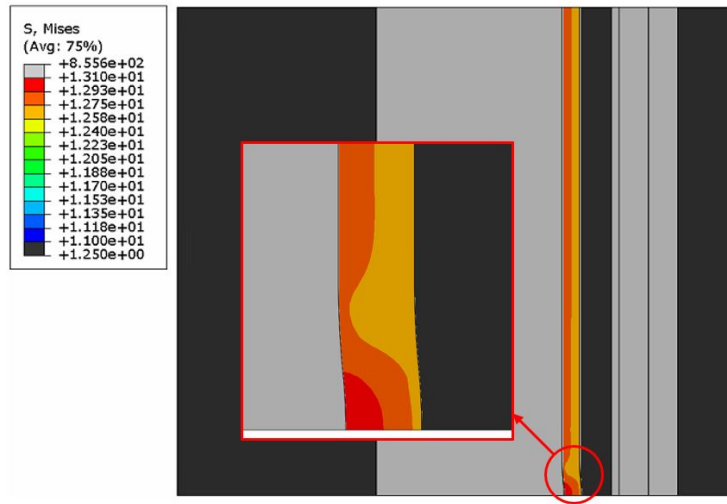


Figure 5.10: Detail of stress field on the Pb layer and identification of the most solicited point.

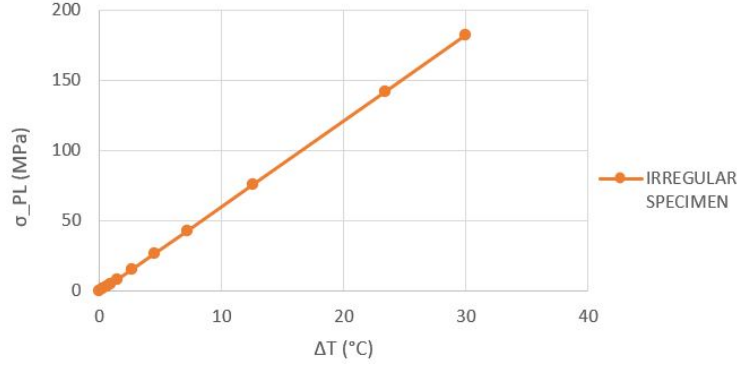
- Finally, all the strain components of the most solicited point on the lead layer, further than the stress components and the Von Mises stress, were selected. This point is contained into the element identified in Figure 5.10 for the model with irregularity, but the same one was considered also for the model with the smooth lead layer. Indeed, in the second model the stress-strain field is uniform along the axis, thus any point on the internal curvature represents the most solicited point.

Once all the desired outputs were known, the necessary elaborations could be done and the strain intensity factor could be computed.

5.7 Results and Intensity Factor

The main target of this section is the *strain intensity factor* computation in a real power cable configuration. Despite of that, before facing that discussion, the preload stress on the steel tape was verified to be equal or near to the wanted value $\sigma_{VM} = 200 \text{ MPa}$. Thus, since the *ramp* shape was used in the thermal gap application, from each time frame of the *preload* loading step the current temperature was easily computed by a proportion to the time. Plotting the collected Von Mises stress against the temperature gap, the chart in Figure 5.11 was obtained. A temperature gap $\Delta T = 30^\circ\text{C}$ allowed to obtain a $\sigma_{VM} \approx 183 \text{ MPa}$, which is close enough to the target value. Then, it was verified that the steel tape was in its elastic field even at the end of the thermal expansion. Indeed, only the elastic property was assigned to this layer. The maximum stress was verified to be $\sigma_{VM} \approx 800 \text{ MPa}$, which (depending on the steel) could effectively still be in the elastic behaviour field. After that, the strain intensity factor computation was faced.

In a multiaxial stress and strain condition, the intensity factor definition is not univocal. Indeed, the usual formula for the strain intensity factor computation

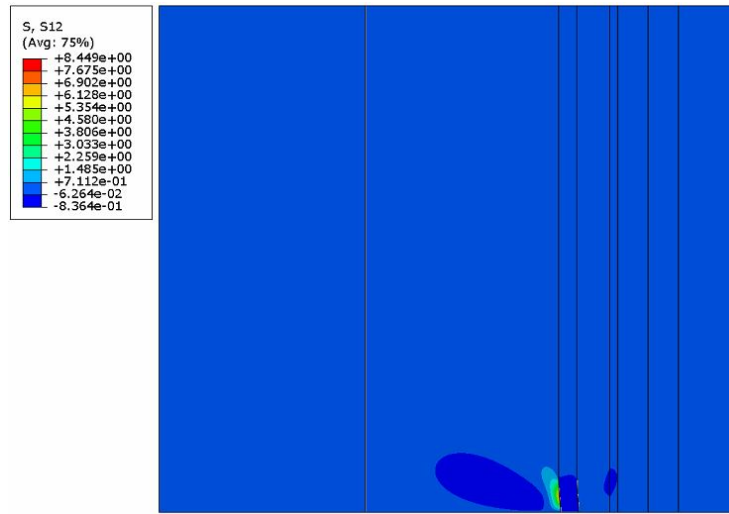

 Figure 5.11: Steel tape preload $\sigma_{PL} - \Delta T$

(see Section 2.1.3) takes into account the maximum strain values for the same global strain, which depends on the nature of the applied load. For this reason, in the previous case where the notch effect was computed on the specimens, the global axial strain $\varepsilon_{g,22}$ was considered, being the load applied an axial one. When a multiaxial problem is faced, where also the load acts along the three main directions, the strain intensity factor $k_\varepsilon = \frac{\varepsilon_{max,eq,irr}}{\varepsilon_{max,eq,smo}} | \varepsilon_g$ can be defined in different ways:

1. Being the thermal expansion predominant along the radial direction, the load could be considered as radial. Thus, the strain intensity factor could be computed for the same global ε_{rr} , which is the radial deformation far away from the irregularity;
2. Since the thermal load generates a multiaxial stress and strain condition, also the same $\varepsilon_{g,eq}$ could be used. This is the equivalent Von Mises strain computed far away from the irregularity (which takes into account all the global strain components rather than only one of them);
3. In the last case, which was the used one, the strain intensity factor can be computed for the same global $\varepsilon_{g,22}$. Even if this component is a consequence the radial deformation (owing to the Poisson's ratio), it was used as reference condition being the same strain component used for the notch sensitivity evaluation in the case of the lead specimens.

Thus, the computation of the intensity factor requires the global axial deformation (which is the same component used for the strain rate evaluation, taken from Figure 5.8) further than the *maximum equivalent Von Mises strain*. For this reason, the most solicited point on the lead layer was identified and the same point was then considered for the model with the smooth lead layer, even if (being the geometry equal along all the axis) any point on the internal curvature would have had the same stress and strain history. Then, the outputs ε_{11} , ε_{12} , ε_{22} and ε_{33} were used in order to compute the equivalent strain in the most solicited point (see Equation 4.2):

$$\varepsilon_{eq} = \frac{2}{3} \cdot \sqrt{\frac{3(\varepsilon_{11}^2 + \varepsilon_{22}^2 + \varepsilon_{33}^2)}{2} + \frac{3(\varepsilon_{12}^2)}{4}}.$$

Figure 5.12: σ_{12} component distribution on the model

Since the strain component ε_{12} is not null in the case of the model with irregularity, even if negligible (see Figure 5.12), the choice of defining a contact between the each layers rather than using a *tie constraint* was justified.

In this way, the charts in Figures 5.13 and 5.14 were obtained, where the first one refers to the highest strain rate, while the second to the lowest one. In order to consider only the effect of the thermal load, the time frames regarding to the previous loading steps were neglected in this analysis and a polynomial cubic interpolation was performed. In the end, at constant global strain, the *strain intensity factor* k_ε was computed:

$$k_\varepsilon = \frac{\varepsilon_{max,eq,irr}}{\varepsilon_{max,eq,smo} |_{\varepsilon_{g,22}}} .$$

It's value was plotted in Figure 5.15 together with the temperature gap during the thermal expansion step.

In the end, the estimation of the irregularity effect on the fatigue life was performed considering the same *notch sensitivity* computed for the specimens (see Table 4.14). Thus, the average values for k_ε , called $k_{\varepsilon,m}$, were computed along the thermal step and they were used in order to compute a constant k_f for both the strain rates (according to the Equation 2.8). All these values were collected in Table 5.12, where is evident that the *fatigue intensity factors* are lower than the ones collected in Table 4.13. This means that the irregularity has a lower damaging effect on the power cable than the expected one from the experimental fatigue tests. Since the strain amplitude introduced by the thermal cycle is higher than the experimental values faced in the previous chapter (see Tables 4.9 and 4.10), this realistic loading condition is considered to act in the low cycle fatigue domain.

An accurate fatigue life estimation can't be performed with the available data and for *qualitative* analysis it's intended a percentage estimation on the reduction of number of cycles to failure, knowing that (in a fatigue analysis) the ratio between the maximum equivalent strain values for the two models is

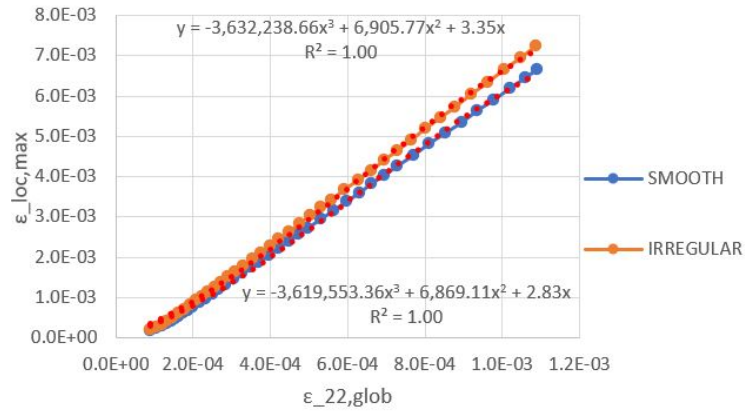


Figure 5.13: Equivalent strain in the most solicited point against the global strain component ε_{22} , Set 1

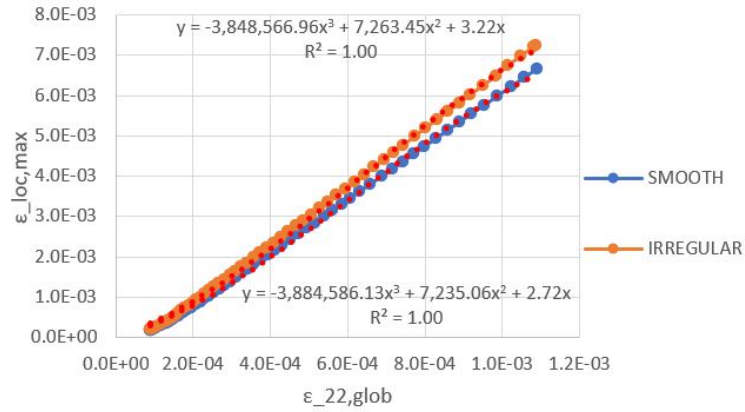


Figure 5.14: Equivalent strain in the most solicited point against the global strain component ε_{22} , Set 2

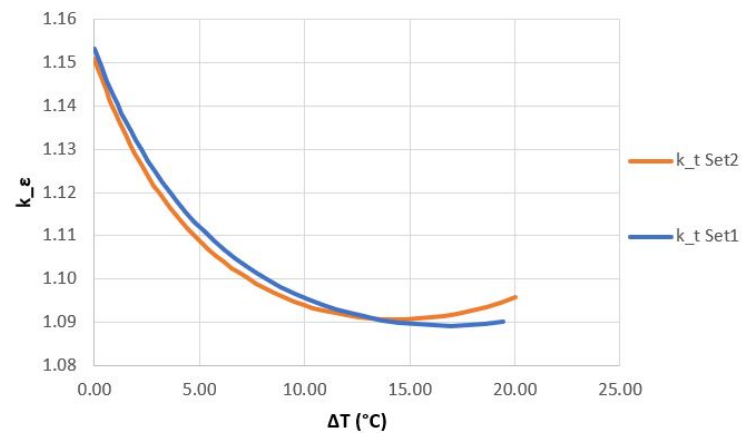


Figure 5.15: Strain intensity factor

Table 5.12: Fatigue intensity factor in the real cable configuration

Set	q	$k_{\varepsilon,m}$	k_f
Set1	0.36	1.11	1.041
Set2	0.32	1.11	1.036

represented by k_f . Even if the fatigue curves of a real cable are different from the ones of the experimental tests, they are anyway layered each other by the multiplication factor k_f . Furthermore, the real fatigue curves are assumed to have the same slope coefficients b_{el} and b_{pl} . Thus, taking into account the fatigue curves in Figures 4.15 and 4.16 and knowing that the thermal cycle is acting in the LCF domain, only their plastic contribution was considered, as plotted as an example in Figure 4.12. If s stands for smooth and i for irregular, the following relations can be written:

$$\varepsilon_{g,22} = A_{pl} \cdot (N_s)^{b_{pl}} \quad , \quad \varepsilon_{g,22} \cdot k_f = A_{pl} \cdot (N_i)^{b_{pl}}.$$

Thus, dividing these equations, the following relations were obtained:

$$k_f = \left(\frac{N_i}{N_s}\right)^{b_{pl}} \quad , \quad \frac{N_i}{N_s} = k_f^{1/b_{pl}},$$

where $1 - \frac{N_i}{N_s}$ consists in the percentage loss of fatigue life owing to the irregularity presence. Even if the real fatigue curves could have a different intercepts (also owing to the compression coming from the hydrostatic contribution) these are not relevant in a *percentage* computation, where only the slope parameters are important.

Then, the same procedure was performed also considering small deformations acting in the elastic field, in order to have an idea on the expected life loss. Thus, the Coffin-Manson-Basquin parameters collected in Table 4.12 were used in order to compute the values in Table 5.13. An higher loss factor is present in

Table 5.13: Percentage life loss estimation

Set	$1 - \frac{N_i}{N_s \text{ el}}$	$1 - \frac{N_i}{N_s \text{ pl}}$
Set1	23%	4%
Set2	18%	3%

the small deformations field (thus in the dominant elastic of the fatigue curves) since the elastic contribution has a lower slope. Thus, the same fatigue intensity factor brings to a major damaging effect. From the other side, having the plastic contribution an higher slope, a less damaging effect is perceived in the low cycle fatigue domain. In any case, since the fatigue curves are describing the safety condition with an high error, it can be concluded that the irregularity has a negligible effect on the fatigue life of the power cable.

The entire analysis was performed considering only one half of a thermal cycle and the maximum value of the local strain is equal to $\approx 7.0E - 3$. The simulation of a complete thermal cycle is not possible with the assigned material properties (being the plastic property assigned with an *isotropic strain hardening*,

rather than kinematic), but it would be also useless. Indeed, the lead properties are regarding to the stabilised conditions of a traction fatigue test, which consists in supposing that the lead layer is already facing those conditions when it's immersed in the seawater. Thus, the simulation should expect a precedent plastic deformation of the lead layer, which for this reason couldn't start its stress-strain history from a null deformation. Otherwise, if the thermal cycles are bringing themselves the lead sheath in stabilised working conditions, it's improbable that they would be exactly the same of an axial fatigue test. Since the problem of the correct simulation of an entire thermal cycle is more complex than what it can be simulated with the available data, one half of the thermal cycle was considered enough in order to compute the *strain intensity factor*. Thus, even if the stress-strain history covered by the simulation is not exactly the real one, what matters is the comparison between the results coming from the two models (the first with the irregularity, the second with a smooth lead layer).

The deformations introduced by the thermal cycle (considering that the strain amplitude is half of the simulated one) are higher than the ones experienced during the axial fatigue tests. Thus, the most solicited point and in general all the elements on the lead layer are laying on an advanced point of the plastic curve, where the plastic curve itself contains more uncertainty (being not supported by experimental data). This could be the reason why the slope of the intensity factor curve in Figure 5.15 faces a variation for the highest temperatures, avoiding a convergence. In any case, the strain intensity factor is lower than the one computed for the lead specimens and decreases for increasing plasticity.

5.8 Data and Results Resume

In this chapter, the irregularity effect on the fatigue life of a submarine power cable in its real configuration was studied. In particular, few steps were followed:

- Two models (one with a smooth lead layer, the second with the irregularity) were created and the material properties were assigned to each layer. See Figure 5.2 for the cable's section geometry, while all the material properties were collected in Section 5.2;
- A preload was applied to the steel tape by means of a thermal gap of $\Delta T = 30^\circ C$, in order to reproduce the preload obtained during the cable production;
- Then, a thermal gap was used in order to simulate the insulation layer expansion and the duration was calibrated in order to obtain the same strain rate measured in the previous chapter. In particular, in Table 5.11 these data are resumed;
- The most solicited point on the lead layer was identified in Figure 3.14 and the equivalent Von Mises strain was computed. Then, the global strain component $\varepsilon_{g,22}$ was extracted from the point highlighted in Figure 5.8 and these two data were used in order to compute the *strain intensity factor*, which trend was plotted in Figure 5.15;
- Using the same notch sensitivity values computed in Chapter 4, the *fatigue notch factor* was estimated in the real situation. Their constant values for both the strain rates were collected in Table 5.12;

- Finally, the k_f was used in order to estimate the percentage life loss, which was computed and collected in Table 5.13 in different situations:
 - Computation for the two strain rate conditions;
 - Computation of the life loss considering external excitations acting firstly in the only plastic field (by means of the plastic contribution of the fatigue curves in Figures 4.15 and 4.16), then in the elastic one.

Chapter 6

Conclusions

The aim of this work was to find out the life loss of a submarine power cable, owing to the effect of the irregularities on the lead sheath. In order to perform such analysis, the computation of the geometrical factor *notch sensitivity* q was mandatory. This was done in different steps, since an evaluation performed directly on the real cable's section was not possible:

1. First of all, several experimental fatigue tests were performed at different strain rates on Pb smooth hourglass-shaped specimens. Then, in Chapter 3, the material calibration was performed in order to model the correct behaviour of Pb in fatigue conditions. In particular, the creep parameters for the *strain hardening* equation were computed by means of an iterative procedure implemented on Isight. Once the lead properties for specimens of thickness $t = 1.8 \text{ mm}$ were known, these could be used for the study of a model with the geometrical irregularity.
2. The second step consisted in the evaluation of the irregularity by means of the same material properties calibrated in the Chapter 3. Fatigue tests were then performed at two different strain rates on irregular specimens. Thus, the comparison between these results and the ones coming from the smooth specimens allowed to compute the notch parameters for the given test conditions: *strain intensity factor*, *fatigue intensity factor* and *notch sensitivity*. The observed results showed a low effect of the irregularity on the fatigue life. Indeed, even if the strain intensity factor is high, the *notch sensitivity* is far away from the value 1. In the last step, these results were used in order to study a section on a real power cable, rather than study lead specimens.

Few approximation were done in the Chapter 4. In particular, the experimental tests were performed on specimens with irregularities with a slightly different geometry if compared to the real irregularities found in another study [12]. Indeed, in some cases the irregularity from the external side of the cable is more severe and sharp-cornered. Finally, these results can be used for the evaluation for the effects of axial and bending loads. Indeed, also when the cable is subjected to bending, the lead sheath faces locally the same stress-strain conditions.

3. The last part of this work consisted in the irregularity effect evaluation

for a real power cable configuration, by means of the previously computed notch sensitivity. This was done in order to understand which could be the effect of the adjacent layers on the fatigue life of the lead sheath. Another approximation of this work consists in the capability of modelling just an half of the thermal cycle. Indeed, the *isotropic hardening* was assigned as a plastic property, thus the Baushingher effect couldn't be observed.

Despite of that, the hydrostatic stress contribution (which comes from the thermal expansion of the inner layers and from the water pressure) has a beneficial effect on the irregularity, which doesn't affect in a substantial way the fatigue life of the power cable. Even if the irregularity shape modelled in this work is not the worst which could be observed, the trend of the reduction of its effect in the fatigue life is evident. Finally, the results are valid also for the portions of the real power cable for which a longitudinal expansion is not possible and this situation was verified by the imposition of symmetrical boundary conditions also on the upper surface of the cable section.

Appendix A

Research Material

A.1 Example of Wrong Calibration

In the Figures A.1, A.2 and A.3 an example of wrong calibration is plotted. The optimization allowed to avoid these errors.

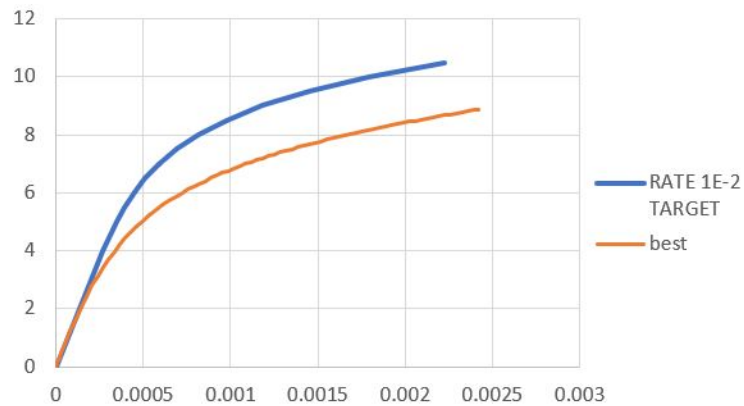


Figure A.1: Wrong calibration for Set 1 data

A.2 Irregularity Geometry

In the following, Matlab file useful in the computation of the four radius defining the irregularity geometry is reported. The output is obtained by choosing the most representative values of *irr* and *start* dimensions, which meaning is explained in the following.

Figure A.4 represents a quarter of the specimen with the convex side on top, where the coordinate $x = 0 \text{ mm}$ defines the end of the grabbing part (excluded in the drawing), while the coordinate $x = 13.5 \text{ mm}$ represents the mean section of the specimen. Thus, the dimensions *irr* and *start* are used in order to define how severe is the irregularity.

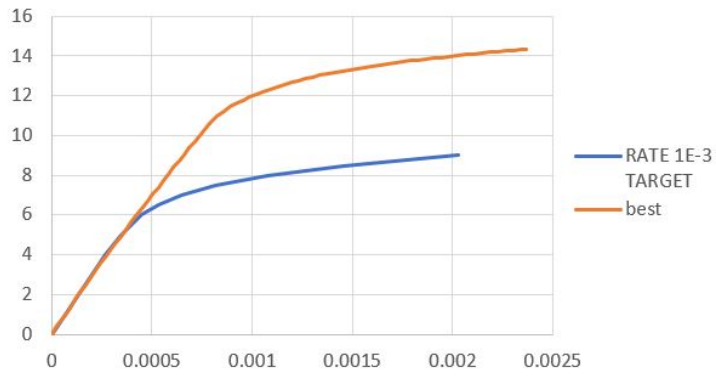


Figure A.2: Wrong calibration for Set 2 data

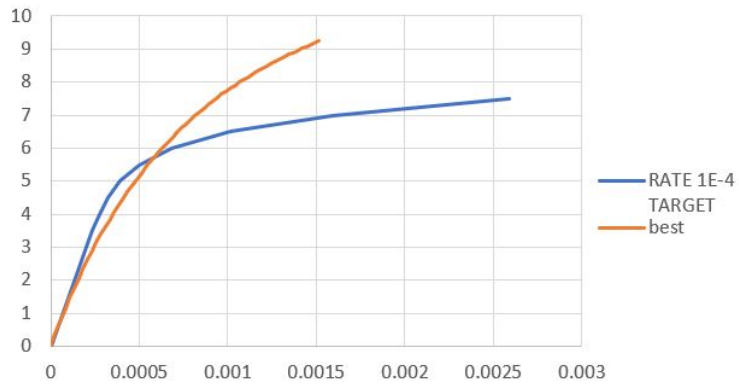


Figure A.3: Wrong calibration for Set 3 data

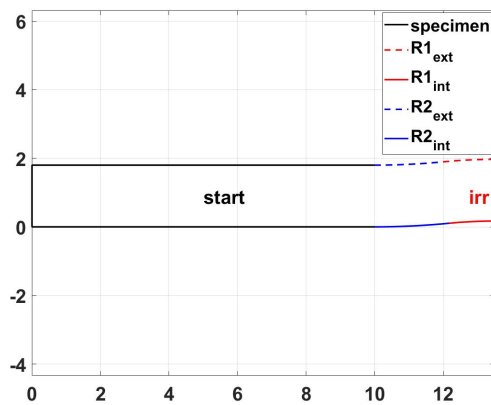


Figure A.4: Matlab plot representing the longitudinal section of the specimen, with irregularity on the centre

- $start = 10 \text{ mm}$ corresponds to the distance between the coordinate 0 and the point where the curvature owe to the irregularity starts, thus the length of the black lines;
- $irr = 3 \text{ mm}$ is the length of the convex part of the irregularity. Since only an half of the specimen is represented, the longitudinal length of the red lines corresponds to $irr/2$.

Finally, in the legend the four circle sections are explained. 1 refers to the circles which centres are under the specimen, while 2 refers to the circles outer from the convex side of the specimen. The dimensions highlighted were used in model creation.

```

close all
clear all

%% half specimen, grab excuded
%%irregularity dimensions
irr = 3; %convex length in mm (y direction) MINIMUM=1, MAXIMUM=20
start = 10; %curved part. 0 if starts at the end of grabbing section...
...START+IRR/2=MAX 13.5mm

%%geometrical data
a = 13.5; %half specimen, circle 1, x center coordinate
b = start; %circle 2, x center coordinate
m = 0.17;
t = 1.8;
t_i = 1.8;

%% computations
gamma = t-m-t_i;
zita = (acos(1+2*(t_i+m-t)*gamma/((b-a)^2+gamma^2)));
zita_int = (acos(1-2*m^2/((b-a)^2+m^2)));
p_x = [b, 0, 0, b];
p_y = [0, 0, t, t];

%%lower circle
down_ext = linspace(pi/2,pi/2+zita,10); %dot sequence in radians
down_int = linspace(pi/2,pi/2+zita_int,10);
R1_ext = (irr/2)/sin(zita); %circle 1 external radius
R1_int = (irr/2-t_i*sin(zita_int))/sin(zita_int);
x1_ext = R1_ext*cos(down_ext); %circle 1
y1_ext = R1_ext*sin(down_ext);
x1_int = R1_int*cos(down_int);
y1_int = R1_int*sin(down_int);

%%upper circle
up_ext = linspace(3/2*pi,3/2*pi+zita,10);
up_int = linspace(3/2*pi,3/2*pi+zita_int,10);
R2_ext = (t_i+m-t)/(1-cos(zita))-R1_ext;
R2_int = ((b-a)^2+m^2)/(2*m)-R1_int;
x2_ext = R2_ext*cos(up_ext);
y2_ext = R2_ext*sin(up_ext);
x2_int = R2_int*cos(up_int);
y2_int = R2_int*sin(up_int);

%%plot irregularity
alpha=-R1_ext+m+t_i;
beta = R2_ext+t;
plot(p_x,p_y,'k'); %specimen

```

```

hold on;
plot(x1_ext+a,y1_ext+alpha,'r--'); %lower circle (1)
plot(x1_int+a,y1_int+(-R1_int+m),'r'); %lower circle (1)
plot(x2_ext+b,y2_ext+beta,'--b'); %upper circle (2)
plot(x2_int+b,y2_int+R2_int,'b'); %upper circle (2)
axis equal;
grid on;
legend('specimen','R1_{ext}','R1_{int}','R2_{ext}','R2_{int}');
set(gcf,'color','w');
text(start/2,t/2,'start','Color','k');
text(13.5-irr/4,t/2,'irr','Color','r');

D1_ext=R1_ext*2;
D1_int=R1_int*2;
D2_ext=R2_ext*2;
D2_int=R2_int*2;

```

A.3 In-depth Analysis about k_f

In this section few clarifications about k_f are discussed:

- Discussion about the measurement of ε_g in a notched specimen;
- Why usually a constant value of k_f is used.

Being lead a material with a wide plastic field, its fatigue life was studied by means of the *fatigue notch factor* applied to the global strain amplitudes, rather than net section stress amplitude. For this reason, a correct computation of the *global strain* must be performed in both smooth and irregular specimen.

Talking about the smooth specimen (even if its section area is not constant) no intensification factors were present. Thus, the *global strain* could be computed for each segment length which bridges the mean section. This consideration consists in supposing that during the fatigue test each point along the specimen is solicited in the same way (same stress and strain values), so that each element is identified by the same point on the hysteresis loop or on the traction curve. If the notched specimen is considered, this is not any more true. Indeed, owing to the stress and strain intensification, the elements near to the notch are covering a wider hysteresis loop than the elements closer to the grabbing part. For this reason, as already discussed in Figure 2.10 (which is reproduced by the experimental results in Figure A.5), computing the global strain on different segments length L_0 could lead to different values.

Global Strain Measurement

In order that all the computations and results could be useful for the design purpose, the measured global strain must be directly comparable to the strain which is applied during real service conditions. Usually, the applied strain is a consequence of the cable bending, thus of the rotation to which the cable is subjected with respect to the straight condition (see Figure A.6). If the lead sheath would be smooth, the global strain computed from geometrical considerations would be equal to the local strain. However, being irregularities present on each cable sheathing at a distance of ≈ 10 mm each other, the same global strain must be used in order to evaluate the local effect of the irregularity.

This means that the global strain that can be computed from geometrical considerations must be the same computed on the irregular specimen, thus the length L_0 on which measurements are performed must be enough longer than the irregularity, in order to obtain a strain measure which is independent from the distance to the irregularity.

In Section 2.1.3 it has been explained that if the measurement is performed far away from the notched section, the described $\sigma - \varepsilon_g$ curve (*apparent* one) is stable and independent from L_0 . On the opposite side, if the length L_0 would be considered gradually closer to the irregularity, the measured strain wouldn't be any more the *true* global strain and the traction curve would be closer to the smooth specimen one. Indeed, in this case the measured strain would be closer to the local one, which is laying on the material plastic curve. Thus, if the output strain of the simulations $\varepsilon_{g,s}$ (considered to be the *global strain*) is not independent from L_0 , the curve which is describing together with the experimental stress is not the *apparent* one, but a curve in the middle between the notched and smooth curve in Figure 2.10. In this way, the *real* global strain $\varepsilon_{g,r}$ (which is computed by the strain definition, as in Figure A.6) is not comparable to the simulation one (being the simulation one affected by the irregularity influence). Thus, using the k_f computed from $\varepsilon_{g,s}$ on the real one $\varepsilon_{g,r}$ would lead to design errors, since these entities are not comparable. Indeed, being $\varepsilon_{g,s} > \varepsilon_{g,r}$ the computed fatigue curve of the irregular specimen would be closer to the real fatigue curve than expected and k_f would lead to an underestimation of the notch effect.

Finally, the simulation strain $\varepsilon_{g,s}$ (collected as output in the point highlighted in Figure 4.5) was verified to be independent from the length L_0 in the following subsection.

ε_g Verification

In order to verify that the simulation global strain could be effectively considered to be *global*, the strain was measured at the identified time frames also on another point more far away from the irregularity. This consists in the limit point of the specimen and it is identified in Figure A.7. In Table A.1 the global strain computed from this point $\varepsilon_{g,2}$ and the one in Figure 4.5 ε_g (which

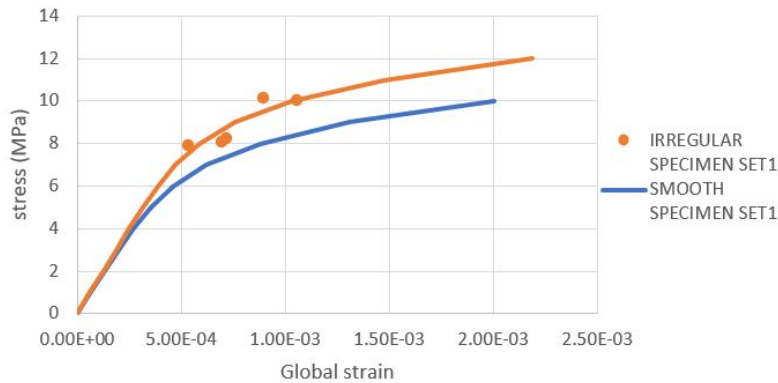


Figure A.5: $\sigma - \varepsilon_g$ for smooth and irregular specimens

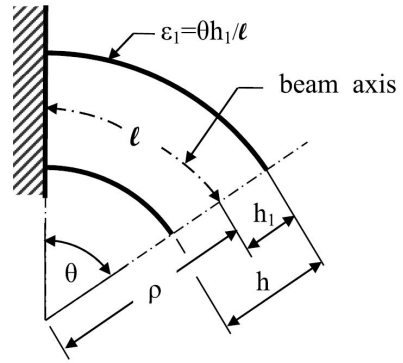


Figure A.6: Deformation resulting from pure bending

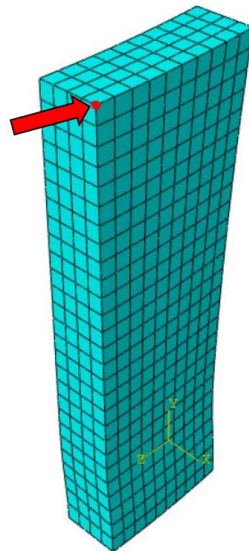


Figure A.7: Global strain verification

Table A.1: Comparison between ε_g , Set 1

time frame	ε_g	$\varepsilon_{g,2}$
32	6.94E-04	7.04E-04
33	7.16E-04	7.26E-04
25	5.38E-04	5.47E-04
48	1.06E-03	1.06E-03
41	8.97E-04	9.05E-04

data are taken from Table 4.9) are collected, for data Set 1. Since the measured values have a relative error of less than 2%, the conclusion is that both the points can be used for the *global strain* computation (being then independent from the length L_0) and the results obtained for k_f can be effectively applied for design purpose.

Constant k_f

In this work, being the experimental data concerning to the irregular specimen few and scattered, the interpolation curve on the $\varepsilon_g - N$ plot was chosen supposing a proportionality with respect to the CMB fatigue curve of the smooth specimen. This choice avoided to perform the interpolation of the experimental data and it led to compute a constant k_f . Despite of that, as explained in Section 4.3.4, if more experimental data were available a more correct interpolation could have been performed by means of the *apparent* traction curve as reported in Figure A.5. Plotting the global strain (which comes from the simulation) together with the nominal stress amplitude (which is an experimental data) and performing the RO interpolation should have led to a case analogous to the one in Figure 2.10. Then, the RO curve could have been used in order to obtain the elastic and plastic components of the global strain ε_g , which are useful in order to perform the *exact* CMB interpolation on the $\varepsilon_g - N$ plot. In this way, two *real* fatigue curves could have been obtained and, by the definition of the fatigue notch factor, a variable k_f with respect to the number of cycles could have been generally computed.

Even if this procedure could be followed, a variable k_f couldn't be easily used and for this reason an average value is generally provided. Indeed, using a variable k_f requests to perform an iterative computation if the fatigue curve of the irregular specimen is not directly accessible:

- First attempt k_f applied to the global strain amplitude;
- N computation from the intersection of the perceived strain amplitude and the fatigue curve of the smooth specimen (*true* fatigue curve) on the $\varepsilon_g - N$ plot;
- Verification that N corresponds to the number of cycles for which the adopted k_f is valid.

For this reason, a constant notch factor is preferred, since it allows to simplify the computations.

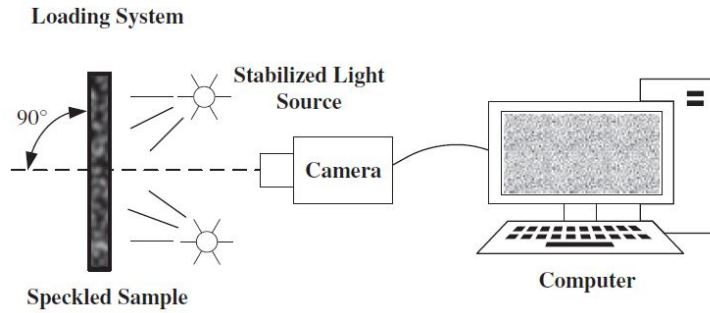


Figure A.8: DIC system example [13]

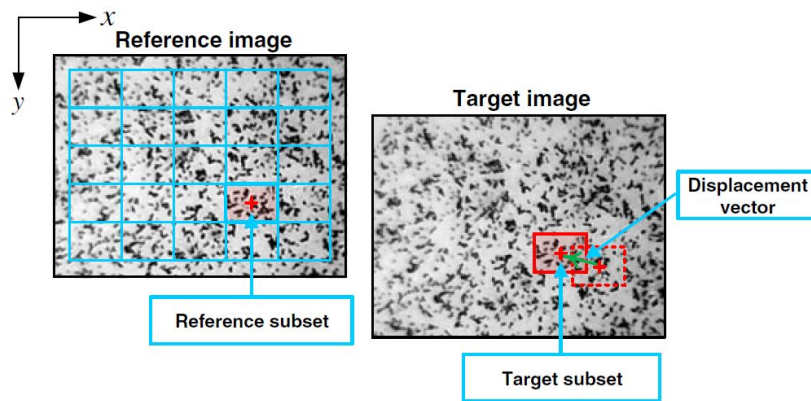


Figure A.9: DIC pattern in two different time frames [13]

A.4 Digital Image Correlation

The *Digital Image Correlation* (DIC) is a non-destructive surface deformation measurements method, which scheme is plotted in Figure A.8. This measurement technique is used when a specimen or component is subjected to a non uniform deformation and it allows to perform a local strain measurement in all the specimen's surface. In order to achieve this result, a speckle pattern must be artificially created on the region of interest, as it was done for the specimens in Figure 4.4. After that, a post processing analysis allows to follow the path of each speckle in order to compute the local deformation for every time instant, as reported in Figure A.9. This technique was used in this work in order to compute more accurate strain values.

Bibliography

- [1] Abaqus (2017), *Abaqus User's guide*, Dassault Systemes.
- [2] ASM international (1996), *ASM Handbook, Volume 19: Fatigue and Fracture*, ASM.
- [3] Barsom J. , Rolfe S. (1999), *Fracture and Fatigue Control in Structures: Applications of Fracture Mechanics*, ASTM.
- [4] Bentachfine S. et al. (1999), *Notch effect in low cycle fatigue*, Elsevier, International Journal of Fatigue 21.
- [5] Bonacuse Peter J. et al. (1995), *Elevated Temperature Axial and Torsional Fatigue Behavior of Haynes 188*, ASME, Journal of Engineering Materials and Technology.
- [6] Callister N. (2018), *Materials Science and Engineering: An Introduction*, Wiley.
- [7] Diana FEA, <https://dianafea.com/manuals/d944/Analys/node405.html>.
- [8] Farouk A.M. (2014), *High Voltage Engineering*, CRC Press.
- [9] Gugliotta A. (2002), *Elementi finiti*, Politecnico di Torino.
- [10] Guruswamy S. (2000), *Engineering Properties And Applications of Lead Alloys*, Marcel Dekker.
- [11] Huang Z. Y. et al. (2014), *Numerical Thermo-Mechanical Stress Analysis for HVDC Cables*. Electrical Insulation Conference.
- [12] Johanson A. et al. (2019), *Small-and full-scale fatigue testing of lead cable sheathing*. ISOPE - International Offshore and Polar Engineering Conference. Proceedings.
- [13] Jianlong Z. et al. (2019), *The state of the art of two-dimensional digital image correlation computational method*, Wiley.
- [14] Kassner M.E. (2015), *Fundamentals of Creep in Metals and Alloys*, Elsevier.
- [15] Lazzarin P. et al. (1997), *Fatigue crack initiation and propagation phases near notches in metals with low notch sensitivity*, Elsevier.
- [16] Luigi M.V. et al. (2019), *Tape winding angle influence on subsea cable sheathing fatigue performance*.

- [17] Lukáš P. (2005), *Fatigue notch sensitivity of ultrafine-grained copper*, Elsevier.
- [18] Majzoubi G. , Daemi N. (2010), *The effects of notch geometry on fatigue life using notch sensitivity factor*, THIM.
- [19] Manson S.S. , Halford G.R. (2009), *Fatigue and Durability of Metals at High Temperatures*, ASM International.
- [20] Milella P. (2013), *Fatigue and Corrosion in Metals*, Springer.
- [21] Penny R.K. (1995), *Design for Creep*, Chapman & Hall.
- [22] Roesler J. et al. (2007), *Mechanical Behaviour of Engineering Materials. Metals, Ceramics, Polymers and Composites*, Springer.
- [23] Sakane M. , Ohnami M. (1983), *A Study on the Notch Effect on the Low Cycle Fatigue of Metals in Creep-Fatigue Interacting Conditions at Elevated Temperature*, ASME Journal of Engineering Materials and Technology, Vol. 105.
- [24] Worzyk T. (2009), *Submarine Power Cables. Design, Installation, Repair, Environmental Aspects*, Springer.